UC Berkeley

UC Berkeley Electronic Theses and Dissertations

Title

Kinetics of Li Transport in Disordered Rocksalt Li-excess Compounds

Permalink

https://escholarship.org/uc/item/1cq824b1

Author

Jadidi, Zinab

Publication Date

2023

Peer reviewed|Thesis/dissertation

Kinetics of Li Transport in Disordered Rocksalt Li-excess Compounds

By

Zinab Jadidi

A dissertation submitted in partial satisfaction of the

requirements for the degree of

Doctor of Philosophy

in

Engineering – Materials Science and Engineering

in the

Graduate Division

of the

University of California, Berkeley

Committee in charge:

Professor Gerbrand Ceder, Chair
Professor Mark Asta
Professor Bryan D. McCloskey

Summer 2023

Abstract

Kinetics of Li Transport in Disordered Rocksalt Li-excess Compounds

by

Zinab Jadidi

Doctor of Philosophy in Engineering – Materials Science and Engineering

University of California, Berkeley

Professor Gerbrand Ceder, Chair

Disordered rocksalt Li-excess (DRX) compounds form a potentially new class of cathode materials for Li-ion batteries, as they contain only abundant metals and do not require Co or Ni. While DRX compounds are promising as battery materials, their properties and performance are not as optimized as those of conventional layered cathode materials. To compete with conventional cathodes, developing a more detailed understanding of the structure-property relation in DRX compounds as it relates to their electrochemical applications is necessary. Specifically, the Li transport properties in DRX materials are not well understood, despite their significant impact on the rate performance of the battery.

This dissertation employed first-principles calculations, the cluster expansion technique, and the kinetic Monte Carlo method to investigate the Li transport properties of DRX materials. Chapter 1 provides an introduction to DRX, including a detailed discussion of the possible Li^+ diffusion mechanisms and percolation in these materials.

Chapter 2 investigates the impact of fluorine and Li-excess on Li migration barriers in rocksalt structures. Fluorine substitution in the oxygen sublattice reduces oxygen redox and enhances energy density and capacity retention. However, its impact on Li transport remains unclear. Using first-principles calculations, this chapter explores the effects of both F substitution and accompanying Li-excess on Li migration barriers. The results show that F has a small negative effect on Li migration barriers while Li-excess decreases Li^+ migration barriers. Because fluorination enables more Li-excess, these results do not predict any detrimental impact on Li transport.

Chapter 3 delves into the essential aspects of the delithiation process and cation short-range ordering (SRO) in DRX compounds. This study uses first-principles calculations and the cluster expansion approach to model the disorder in DRX $Li_{2-x}VO_3$ with $0 \leq x \leq 1$. The chapter discusses the SRO of Li in tetrahedral and octahedral sites, and the order in which Li delithiates and V oxidizes with respect to local environments. The results indicate that the number of nearest neighbors V determines the order of octahedral Li delithiation, and that V are oxidized in a manner that minimizes the electrostatic interactions among V. This research provides valuable insights into how to tailor the performance of V-based DRX cathode materials by controlling SRO features that may reduce energy density. Additionally, findings of this chapter shed light on the relationship between SRO and Li transport properties.

Chapter 4 investigates the kinetics of Li^+ transport in disordered rocksalt structures, focusing on DRX $Li_{2-x}VO_3$. Using a combination of first-principles calculations, cluster expansion approach, and kinetic Monte Carlo simulations, the chapter provides insights into the factors affecting Li^+ transport properties in DRX materials. The results show that the relative stability of tetrahedral Li and octahedral Li occupancy plays a crucial role in determining the number of active sites in the percolation network and the resulting Li^+ transport properties. Furthermore, the chapter demonstrates that the wide site-energy distribution can cause correlated motion in $Li_{2-x}VO_3$, which can hinder Li^+ transport. Although this study focuses on $Li_{2-x}VO_3$ as a model system, the insights gained apply to all DRX materials, given their inherently broad site-energy distributions.

In the concluding chapter, Chapter 5, the key findings of this dissertation are summarized.

تقدیم به پدر و مادر عزیزم

Table of Contents

List of Figures

Acknowledgments

Chapter 1
Introduction

1.1 Disordered rocksalt with Li-excess compounds as cathode materials

Rechargeable batteries, among various forms of renewable energy sources, possess the characteristics of modularity and scalability. [1] This makes them a particularly promising solution to meet the urgent need for clean energy. [2,3] As of now, rechargeable Li-ion batteries continue to surpass different kinds of secondary batteries in performance, primarily because of their unique combination of high energy and power density. [4] The majority of commercial Li-ion cathodes are layered structures such as $LiCoO_2$ (LCO), $Li(Ni, Co, Mn)O_2$ (NMC), and $Li(Ni, Co, Al)O_2$ (NCA), where O anions form a face-centered cubic (FCC) framework with alternating layers of LiO_6 and MO_6 on the (111) planes of the FCC oxygen lattice, as shown in Figure 1-1a. [2] The choice of Co, Ni, and Mn in these layered materials is due to the fact that these transition metals (TMs) do not migrate during battery cycling and prefer octahedral coordination, thanks to their highly occupied t_{2g} orbitals. [5,6] This characteristic is crucial for stabilizing the layered structures and preventing cation mixing or disordering. However, the known layered cathodes suffer from limitations such as low thermal stability, significant c-axis shrinkage (structural collapse) during delithiation, and a limited capacity (140 – 200 mAh/g) as a result of incomplete Li extraction. [7,8] Another major challenge facing layered Li-based cathode materials today is the scarcity of Co resources, which can barely meet the growing demand for portable electronics and electric vehicles. [9] In order to achieve the objectives set by the Vehicle Technologies Office (VTO) of the US Department of Energy for battery and cell technologies, including a cost below $100/kWh, a range of 300 miles, and a charge time within 15 minutes,[10] it is essential to overcome the constraints imposed by the layered structure in cathode materials. One approach to address this challenge is to develop cathode materials that can tolerate cation disordering, thus expanding the range of chemistries that can be used to produce Co-free cathodes.

Complete disorder of cation sites in a layered material leads to a rocksalt-like structure. Rocksalt represents a type of ionic crystal structure in which cations are arranged in an FCC pattern, while anions occupy all the octahedral sites. Alternatively, this can be described as an FCC array of anions with cations filling the octahedral sites [11] as shown in Figure 1-1b.

During the 1990s, certain instances of disordered rocksalt cathodes were identified. [12,13] These materials were initially considered electrochemically inactive due to the slow kinetics of Li^+ transport, resulting in subpar electrochemical performance. [11] However, the development of the so-called 0-TM percolation theory facilitated the design of disordered rocksalt materials with

improved Li$^+$ transport properties.[14,15] According to the 0-TM percolation theory, Li$^+$ in a disordered structure can percolate if there is sufficient Li (an excess beyond the 1:1:2 Li:TM:O ratio of the layered phase) to form low-barrier percolating 0-TM diffusion networks.[14,15] The insights gained from the 0-TM percolation theory have provided valuable guidelines for the battery community to develop cobalt-free and nickel-free disordered rocksalt structures with Li-excess (DRX)[14,16–24] which are capable of delivering specific energies up to 1000 Wh/kg.[11,16]
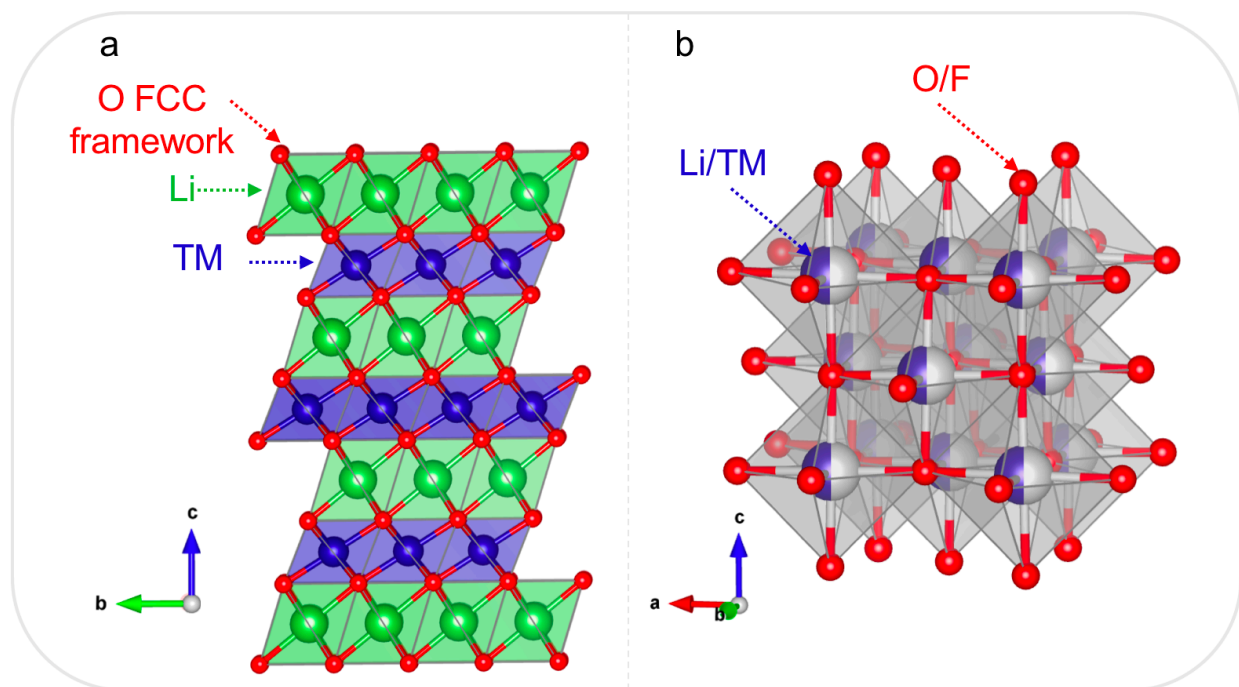
Figure 1-1 (a) An O3-type layered LiCoO$_2$ structure, where oxygen anions form an FCC framework, with alternating layers of LiO$_6$ and MO$_6$ located on the (111) planes of the FCC oxygen lattice. Li, TM, and O are depicted in green, blue, and red colors, respectively. **(b)** Disordered rocksalt structure with close-packed oxygen framework, where Li, TM are randomly distributed on the octahedral cation sites.

1.2 Li$^+$ Diffusion mechanisms and percolation in disordered rocksalt structures

In layered intercalation compounds, the migration of Li$^+$ can occur through two distinct mechanisms. The first is the oxygen dumbbell hop (ODH) mechanism, where Li$^+$ migrates between two octahedral sites by traversing the anion dumbbell.[25] The second mechanism is the tetrahedron site hop (TSH) mechanism, where Li$^+$ moves through an intermediate tetrahedral site that shares anion-coordinated faces with the initial and final octahedra.[25] Typically, the ODH mechanism is observed during single vacancy migration, primarily because of the repulsion exerted by the cations surrounding the migration path.[25] However, when there is at least one additional Li vacancy present, the energetically favored mechanism in layered materials is the TSH.[25] It's worth mentioning that Li$^+$ can also migrate via the intermediate tetrahedral site during a single vacancy mechanism. This is possible when the lower and upper intermediate tetrahedral sites—bridging the initial and final states of the hop—do not have face-sharing interactions with

the same species. In instances of asymmetry between the upper and lower intermediate tetrahedral sites, Li$^+$ passes through the intermediate site that presents the least migration barrier. [26]

In the TSH mechanism, we categorize the hop types based on the count of TM occupying octahedra that face-share with the intermediate tetrahedral site. For instance, if the intermediate tetrahedron has no nearest-neighbor TMs, it is labeled as a 0-TM channel, adhering to the notation frequently found in the relevant literature. [14] As the intermediate tetrahedron has four nearest-neighbor octahedral sites—two of which are the initial and final sites for the Li$^+$ hop—we can divide potential channels into 0-TM, 1-TM, or 2-TM types. In layered materials, the tetrahedron is commonly surrounded by either 1-TM or 3-TMs, with the 1-TM divacancy channel acting as the primary path for Li$^+$ migration. However, in the case of DRX materials, tetrahedra can be encircled by anywhere from 0 to 4 TMs. This allows for the presence of 0-TM, 1-TM, and 2-TM channels for Li$^+$ to migrate through. Figure 1-2 visually demonstrates the ODH and TSH mechanisms, including various counts of face-sharing Li, TM, and vacancies.
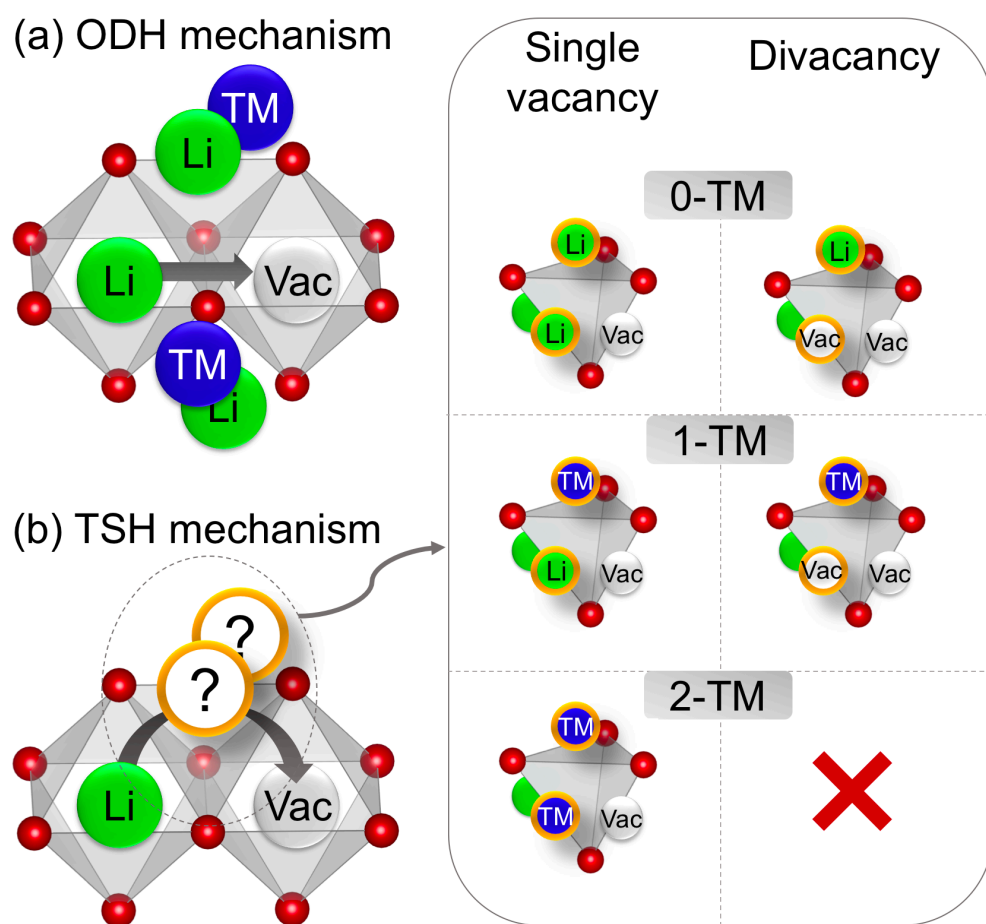
Figure 1-2 (a) The Oxygen Dumbbell Hop (ODH) mechanism where Li$^+$ migrates between two octahedral sites by crossing the anion dumbbell. **(b)** The Tetrahedral Site Hop (TSH) mechanism in which Li$^+$ moves via an intermediate tetrahedral site that shares anion-coordinated faces with the initial and final states of the hop. Adjacent schematics depict these intermediate tetrahedral sites. Each intermediate tetrahedral site face-shares with four octahedral sites, two of which involve migrating Li$^+$ and the final state vacancy. Depending on the species occupying the

remaining two octahedral sites, we can classify the tetrahedron channel into 0-TM (no surrounding TM), 1-TM (one surrounding TM), and 2-TM (two surrounding TMs).

Cation disordering in a structure tends to shorten the height of the tetrahedron, which consequently increases the electrostatic repulsion experienced by Li^+ when it is close to a TM. For instance, the tetrahedral magnitude in layered $Li(Ni_{0.5}Mn_{0.5})O_2$ has been determined to be approximately 2.64 Å. [27] However, calculation results show that in Mo and Co-based DRX materials, the tetrahedron height ranges from 2.35 Å to 2.41 Å. [14] This decrease in tetrahedron height results in migration barrier for the 1-TM channels that exceeds 300 meV, causing the 1-TM to mainly become inactive in DRX cathode materials. [14] As an example, the migration barriers for the 1-TM channels in Mo and Co-based DRX material has been calculated to vary between 400 to 700 meV. [14] Adding more TMs near the migration path further increases this migration barrier, leading to the 2-TM channels being inactive in DRX materials. [14,15] Despite the majority of 1-TM channels being inactive in DRX materials due to their high migration barrier, cation disordering leads to the formation of 0-TM channels, which are not found in layered materials. [14] Computational studies have shown that in DRX materials, Li^+ primarily prefers to traverse through 0-TM channels as their migration barriers usually fall below 300 meV. [14]

Disordering facilitates the formation of locally low-barrier 0-TM channels. However, it is equally crucial to establish a connection between these low migration environments, implying that Li^+ should be capable of percolating throughout the structure. The concept of having Li-excess arises from the requirement for substantial Li in the structure to stimulate the formation of Li_4 clusters. This is a pivotal step in maintaining connectivity between 0-TM channels. Less than ten years ago, Urban et al. [14,15] proposed a percolation theory for DRX materials. They suggested that Li^+ percolation in a DRX materials (represented as $Li_xTM_{2-x}O_2$, where $0 < x < 2$) could be determined based on two key factors. The first is the distribution of various tetrahedral clusters within the structure, such as Li_4 (0-TM), Li_3TM (1-TM), Li_2TM_2 (2-TM), $LiTM_3$ (3-TM), and TM_4 (4-TM). This distribution depends on the level of cation disorder and the Li to TM ratio, indicating the amount of Li-excess. [14,15] The second factor is the 3D network of 0-TM diffusion channels featuring low migration barriers. [14,15] Urban et al. [14,15] demonstrated that a critical Li concentration (x_C) is necessary to form a percolating network of low-barrier 0-TM channels. Specifically, they found that for a completely disordered cation arrangement (100% cation mixing), maintaining a 3D percolating network of 0-TM channels for Li^+ diffusion requires 10% Li-excess. [14,15] To extract 1 Li per formula unit (f.u.), 26% Li-excess is necessary. [14,15]

The current version of the percolation theory [14,15] was developed based on the concept of octahedral Li occupancy and the TSH diffusion mechanism. [25] However, recent findings have shown that Li can also occupy tetrahedral sites [28–30], especially in highly delithiated states when no species are face-sharing with the tetrahedral Li. As a result, in DRX materials, Li^+ can engage in not only the ODH and TSH mechanisms but also mechanisms where the tetrahedral site is one of the end sites of the hop, such as tetrahedral-octahedral-tetrahedral, octahedral-tetrahedral, or tetrahedral-octahedral hops. [30] Figure 1-3 illustrates additional migration mechanisms in DRX structures where the tetrahedral site is involved as one of the end sites of the hop. The migration barrier for Li^+ transitioning from a tetrahedral site to an intermediate octahedral site and stabilizing in either an opposing tetrahedral site or a corner-sharing tetrahedral site has been computationally found to be around 300 meV in $Li_{3+x}V_2O_5$, where $0 < x < 2$. [30] In the same compound, the Li^+ migration barrier from a tetrahedral site to an edge-sharing tetrahedral site has been found to vary between 300 and 900 meV, depending on the local environment of the migrating ion. [30]
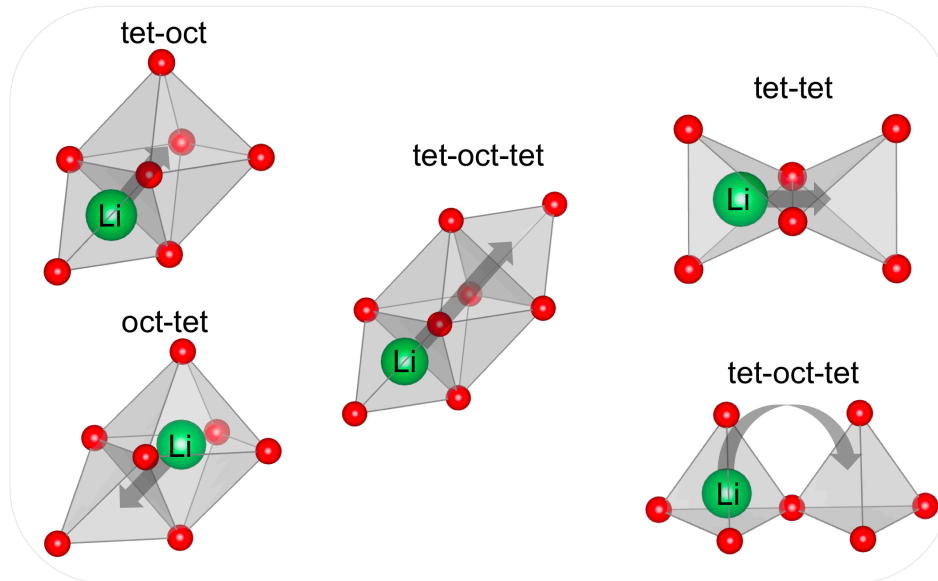
Figure 1-3 DRX cathode materials offer various possibilities for Li migration hops when either the initial or final state of the hop involves a tetrahedral site. By incorporating tetrahedral Li occupancy, it becomes feasible to have hops where Li^+ transitions from a tetrahedral site to a face-sharing octahedral site (or vice versa), moves from a tetrahedral site to an opposing tetrahedral site through an octahedral site, or migrates from a tetrahedral site to a corner-sharing or edge-sharing tetrahedral site.

1.3 Motivation and outline

While the use of DRX as a battery material holds promise in the battery community, it has yet to reach the level of optimization seen in traditional layered cathode materials in terms of properties and performance. [11] To compete with these conventional cathodes, it is essential to gain a deeper understanding of the relationship between the structure and properties of DRX in electrochemical applications. [11] One crucial aspect that remains poorly understood is the Li transport properties in DRX materials, despite its significant role in battery rate performance. This lack of knowledge is primarily due to the challenges in experimental measurements of Li diffusivity [21,31–33] and the complexity of building kinetic models for high-component DRX systems, similar to what has been accomplished for layered intercalation compounds. [25,31,32,34–36] While the 0-TM percolation theory offers valuable insights into the structural features that can influence Li^+ transport properties, it does not encompass all the factors that affect them. Consequently, its predictions do not always lead to high Li diffusivity [20,21,37] or the desired rate performance. [38] To enhance the percolation theory and better capture Li^+ transport properties in DRX cathodes, it is essential to gain a deeper understanding of the fundamental factors that affect both the local migration barrier and macroscopic Li^+ diffusivity in DRX materials. The following sections outline the specific focus of each chapter in this dissertation, providing insights into the Li^+ transport properties of DRX materials.

The inclusion of fluorine into the oxygen sublattice in the DRX materials has been shown to decrease oxygen redox, resulting in a reduction of the average anion valence and increasing the amount of redox-active TM.[11,24] This, in turn, enhances the energy density, average voltage, and capacity retention of these materials. [11,24] Nevertheless, the impact of fluorine substitution on Li^+

transport — an essential determinant for the rate performance of DRX-based cathodes — requires further investigation. In Chapter 2, first-principles calculations are used to analyze the influence of fluorine and Li-excess on the Li^+ migration barriers in various local environments of an Mn-based rocksalt structure.

In Chapter 3, I leverage first-principles calculations and the cluster expansion methodology to simulate the disorder in DRX $Li_{2-x}VO_3$ material, $0 \leq x \leq 1$. This compound has been experimentally studied as a potential candidate for cathode materials. The chapter delves into Li Short-Range Ordering (SRO) in both tetrahedral and octahedral sites and the chronological process of Li delithiation and vanadium oxidation in various local environments. Furthermore, this chapter elucidates the link between Li SRO at varying Li contents and the empirically observed Li^+ diffusivity within the $Li_{2-x}VO_3$ system. The cluster expansion constructed in this chapter is integral in capturing the thermodynamic properties of the $Li_{2-x}VO_3$ system. It also establishes the groundwork for the Kinetic Monte Carlo model developed in the Chapter 4.

In Chapter 4, I examine critical factors that impact Li^+ percolation in DRX materials. I present a kinetic model that takes into account both tetrahedral and octahedral Li occupancy, as well as the site energies of Li occupation, which have the potential to induce correlated motion. Similar to Chapter 3, the $Li_{2-x}VO_3$ model system is maintained for this chapter. To model the kinetics of Li^+ transport on this cluster expansion, the kinetic Monte Carlo method is employed using the rejection-free (n-fold) algorithm. This chapter highlights three significant aspects. First, it emphasizes the significance of considering both tetrahedral and octahedral Li occupancy when predicting transport properties in DRX materials. Second, it explores the fundamental factors contributing to changes in diffusion coefficients as the Li content varies in $Li_{2-x}VO_3$. Lastly, it investigates the influence of the energy landscape on the correlated motion of Li^+ ions.

Chapter 5 provides a comprehensive summary of the key findings presented in the dissertation.

Chapter 2

Effect of Fluorination and Li-excess on the Li Migration Barrier in Mn Based Cathode Materials[1]

2.1 Introduction

Li-Rich transition metal (TM) oxides are considered prospective high-energy-density cathode materials for the next generation of lithium ion batteries (LIBs). [39–43] An especially attractive class of Li-rich cathode materials are those based on Mn redox due to their large energy densities, widespread availability, cost efficiency, and relative stability of the Mn^{4+} valence state. In addition, these Mn-based cathodes [44,45] do not contain Co and Ni, which are limited resources. [9] In Li-rich compositions the TM redox capacity is typically lower than the Li-content capacity. Accessing high capacities therefore requires significant oxygen redox participation, [46,47] which commonly leads to more oxygen gas release and thus poor capacity retention. [48–51] Substitution of some O by F lowers the average valence of the cations thereby increasing the TM redox capacity and reducing oxygen loss during cycling. [24] While the impact of fluorination on the redox capacity is well understood, it is also crucial to understand how F substitution affects the Li transport. Previous work has shown that while small amounts of F reduce the percolation of Li migration paths, larger F contents (>15%) improve percolation. [52] In this work we investigate the effect F has on the local migration barrier in Mn based compounds.

We use orthorhombic-$LiMnO_2$ (o-$LiMnO_2$) as a prototypical material as it exhibits similar structural motifs to Mn-based Li-rich cathodes (namely Mn and Li in octahedral sites on the same anion FCC lattice), and it has a larger variety of anion environments compared to layered TM oxide cathodes. As such it is a good ordered model system to evaluate the effect of F on Li mobility.

Van der Ven *et al.* [53] proposed that Li migration in rocksalt structures can occur through a single or divacancy mechanism. In general, the activation energy of the divacancy mechanism is lower in layered cathodes making it the active mechanism as soon as any Li is removed from the structure. [25,54] To fully understand the interplay between the effect of F and Li-excess, we calculate

---

[1] This chapter is based on the previously published paper: Jadidi, Z., Chen, T., Xiao, P., Urban, A., & Ceder, G. (2020). Effect of fluorination and Li-excess on the Li migration barrier in Mn-based cathode materials. *Journal of Materials Chemistry A*, *8*(38), 19965-19974.

the migration barrier for both mechanisms for varying amounts of F substitution and Li-excess and for different anion occupancies around the migrating Li. Based on the results from our calculations, we conclude that F substitution has only a small effect on Li migration barriers while Li-excess has a strong favorable effect and decreases the Li migration barrier in agreement with previous publications. [14] Hence, we do not expect any detrimental impact on Li ion transport when fluorination is used as a design strategy to increase the amount of TM redox and reduce oxygen loss from cathode materials.

$LiMnO_2$ has an orthorhombic *Pmmn* (o-$LiMnO_2$) structure [55] with close-packed oxygen lattice in which octahedrally coordinated Li and Mn align themselves in corrugated layers. All MnO_6 octahedra share a common edge with each other, and those with Mn^{3+} experience Jahn–Teller distortion due to the preference for the high spin state ($t_{2g}^3 e_g^1$). [56] Half of the anion sites are coordinated by 2Li and 4Mn, and the other half are coordinated by 4Li and 2Mn. Because of the weaker binding between TM and F compared to that between TM and O, F tends to substitute for O sites with maximal Li coordination. [57] When Li-excess is introduced into the composition, some anion sites become coordinated by 5Li and 1Mn. These anion sites are preferred substitution sites to introduce F as they generate only 1 TM–F bond. [57]

Li can migrate either through the anion dumbbell between two octahedral sites, ODH mechanism, as shown in Figure 2-1a (bottom), or through an TSH mechanism, as shown in Figure 2-1b (bottom).
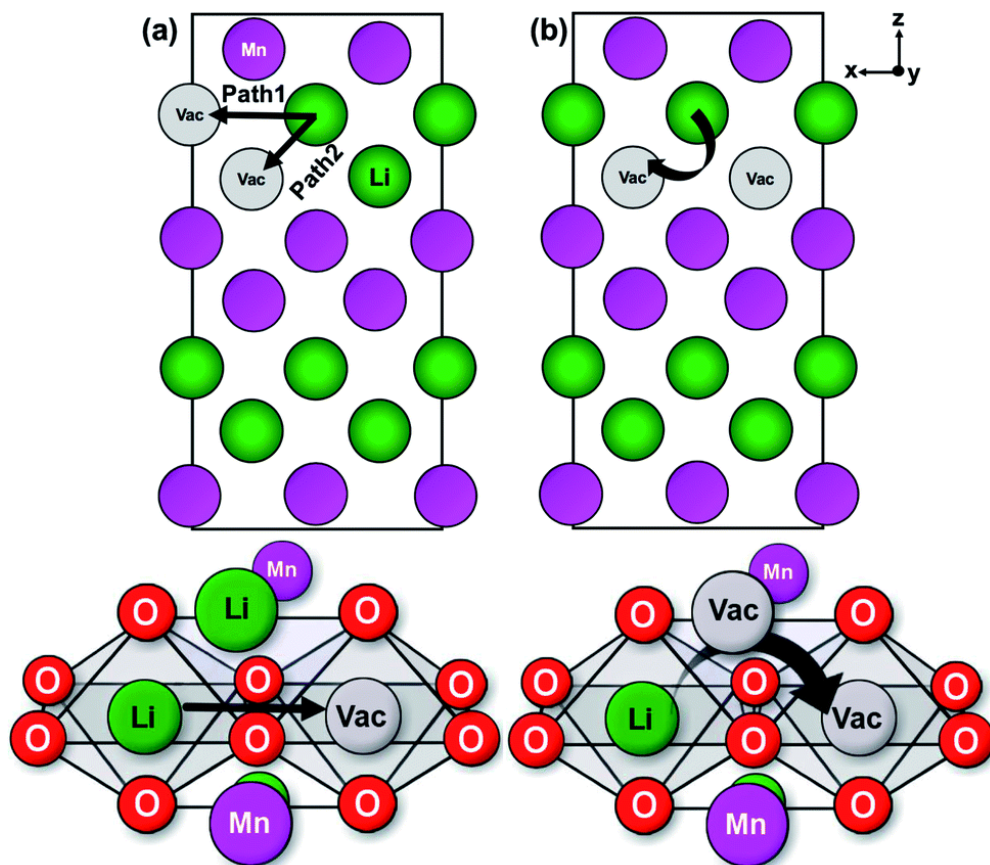
Figure 2-1 Possible Li migration paths in o-$LiMnO_2$ through the **(a)** single vacancy mechanism and **(b)** divacancy mechanism shown in the 010 plane (top) and in three-dimensional

representations of the nearest neighbor cations along the path (bottom). Li hops occur along the trajectory shown by the black arrows. The single vacancy mechanisms can proceed via an in-plane hop (path 1) or an out-of-plane hop (path 2), whereas the divacancy mechanism is shown proceeding through an intermediate 1-TM channel. Note that the divacancy mechanism can only proceed through out-of-plane hops. Li, Mn, and O are shown as green, purple, and red spheres. O atoms are not shown in the top figures for clarity.

2.2 Methods

2.2.1 First-principles density functional theory calculations

We obtained structural energies from density functional theory (DFT) [58,59] using the generalized-gradient approximation (GGA) with the PBE exchange–correlation functional [60] and projector-augmented wave (PAW) method,[61,62] as implemented in the Vienna *ab initio* Package (VASP) package. [63,64] We used a plane-wave cutoff of 520 eV in all of our calculations. In the voltage calculation, a Hubbard-U [65] correction was employed for Mn using the suggested U-value in the Materials Project ($U = 3.9$ eV). [66] For all the calculations, we used reciprocal space discretization of 25 K-points per $Å^{-1}$ and set the electronic convergence to 10^{-5} eV and the force convergence to -0.01 eV $Å^{-1}$. The nudged elastic band (NEB) method is used to compute diffusion activation barriers [67] based on five images along the diffusion paths for both single vacancy and divacancy migration mechanisms in both pristine o-LiMnO$_2$ and, 4%, 6% and 50% fluorinated o-LiMnO$_2$. All NEB calculations were performed using GGA without Hubbard-U correction in order to avoid potential convergence issues associated with electron localization at various atomic centers along the migration path. [68,69] Due to the directional dependence of the migration barriers, we also show the kinetically resolved activation barrier (KRA). [25]

2.2.2 Structural model

The pristine prototype structure o-LiMnO$_2$ (with space group *pmmn*) was obtained from the Materials Project and has materials ID mp-18767. [66] For the non-fluorinated structure and the highly fluorinated (50% F) structure, calculations were performed in a supercell of 64 atoms. Calculations of slightly fluorinated (4% F) structures were performed in a supercell with 96 atoms to isolate the effect of a single F on the diffusion barrier. The F is substituted on one of the anion sites that is coordinated to the maximal number of Li (coordination environment of 4Li and 2Mn). The extra Li that represents Li-excess generally strongly prefers to bond to F rather than to O. To account for this preference, the Li added to the structures substitutes for one of the two Mn bonded to the added F. After substituting the first O for F and an adjacent Mn for Li, we additionally substitute one more O, with the maximal Li local environment, for F to maintain charge neutrality (for the case of 4% F concentration). Note that the second F is substituted so that it is 4 atomic layers (~6 Å) away from the first F in order to isolate the effect of a single fluorine on the energy barrier. In the model structure with 50% fluorination, the same strategy is used as for the 4% fluorinated structure, except that the number of F and Li-excess substitution is higher. For the calculation of Figure 2-4 where there is no Li-excess in the structure, a background charge is introduced to maintain charge neutrality in order to isolate the effect of the location of F substitution. No charge background was introduced in other calculations.

2.3 Results

2.3.1 Diffusion mechanism in pristine o-LiMnO$_2$

All calculations are performed with the Nudged Elastic Band method (NEB) and Density Functional Theory in the GGA approximation. More details are provided in the Methods section. Because of the orthorhombic symmetry in o-LiMnO$_2$, the in-plane hop (path 1 in Figure 2-1a) and out-of-plane hop (path 2 in Figure 2-1a) are not the same. We find that the out-of-plane hop has a lower migration barrier (500 meV) than the in-plane hop (560 meV) due to the closer proximity of the migrating Li ion to Mn ions along the path. In the following discussion, we therefore generally consider the out-of-plane hop because of its lower barrier, and we use this out-of-plane barrier of 500 meV as a reference for other single vacancy hops. The minimum energy path (MEP) of the single vacancy hop is shown in Figure 2-S1 of the Supplementary Information. Our result is consistent with the Li diffusion barrier previously calculated for the ODH path in monoclinic LiMnO$_2$ (500 meV) [70] in which the immediate local environment for Li diffusion *via* the single vacancy mechanism is similar.

Figure 2-1b shows a divacancy diffusion mechanism proceeding through a 1-TM channel TSH. Migration proceeds through the face-sharing tetrahedral site which face-shares with one TM cation. Note that a given pair of octahedral sites is connected through two different TSH, one on each side of the oxygen dumbbell edge that is shared between the initial and final octahedron. For clarity we adopt the convention that in our figures the TSH path discussed is always depicted above the oxygen dumbbell. The activation energy of the divacancy hop in this scenario, as calculated with NEB, is 240 meV, much smaller than the barrier for the out-of-plane single vacancy hop (500 meV). We also use this divacancy barrier in the non-fluorinated o-LiMnO$_2$ as a reference to compare with those in the presence of F and Li-excess.

2.3.2 Single vacancy diffusion mechanism in presence of F and Li-excess

In F-substituted Li-excess compounds, Li sites with different local environments exist, so that the initial and final states, and thus the forward and backward migration barriers, of a Li hop may differ in energy, unlike the barriers in a symmetric local environment. In such a context, the kinetically-resolved activation (KRA) barrier is usually defined as the average between the forward and backward barrier. [25] Figure 2-1b shows a summary of the diffusion barriers for single vacancy Li migration in different local environments. The horizontal bars show the magnitude of the forward (yellow striped bars), backward (solid blue bars), and KRA (dotted gray bars) barriers for each specific atomic configuration labeled on the y axis of the chart. The green vertically striped bar is the energy barrier in the pristine non-fluorinated LiMnO$_2$ structure. The local atomic configurations and trajectories of the migrating Li atoms are visualized adjacent to their respective bars and listed in the table. It should be noted that, while these figures capture the most local part of the environment around the migration path, the site occupancy outside of these pictures can also influence the energy. Three different trajectories are specified: (i) straight black arrow corresponding to ODH mechanism, (ii) bent black arrow corresponding to TSH mechanism, and (iii) slightly curved blue arrow in which the migrating Li does not fully go through the tetrahedral site. All the arrows show the direction of the forward barrier.
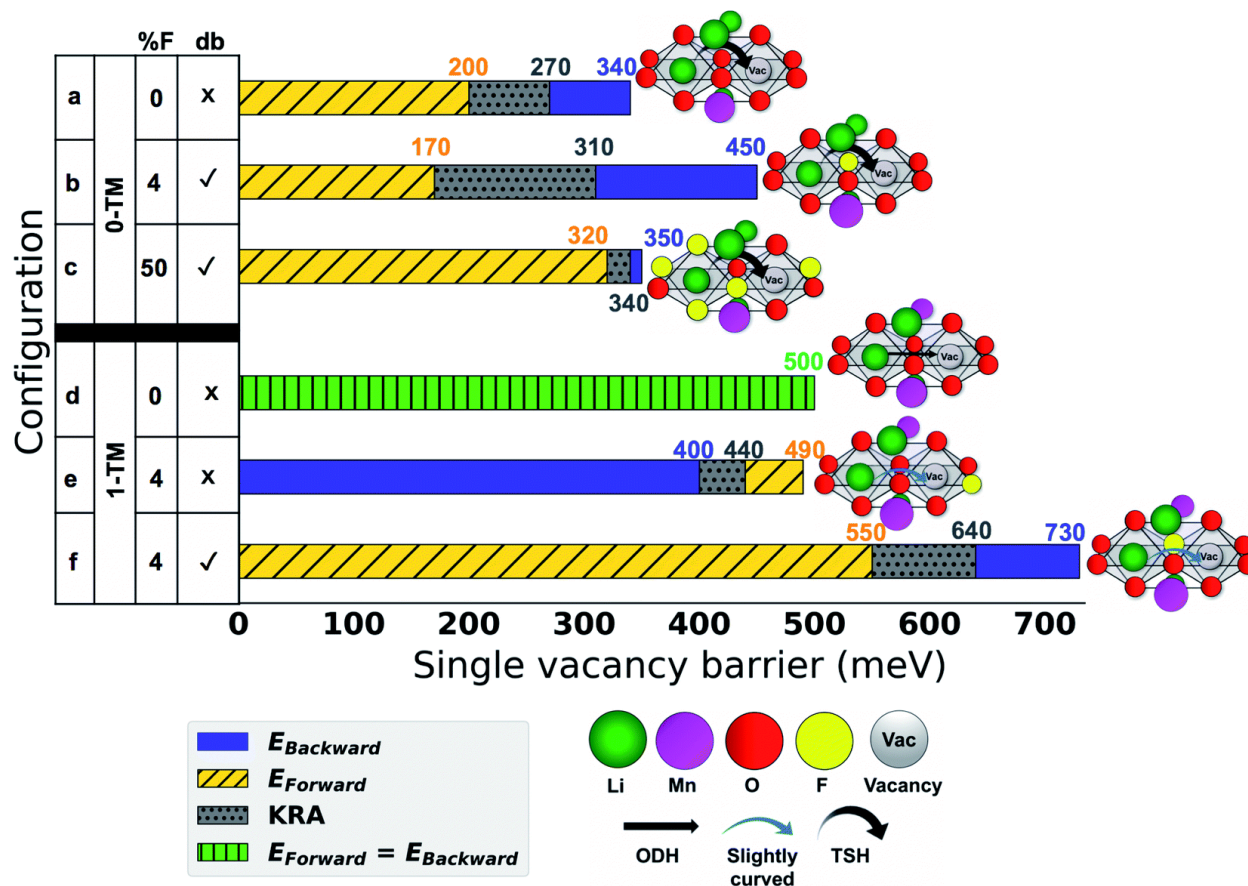
Figure 2-2 Horizonal bar chart showing the single vacancy diffusion barriers for various local configurations around a migrating Li. The black and blue arrows in each of the atomic configurations show schematically the Li migration trajectory. Li, Mn, O, F, and vacancy are shown as green, purple, red, yellow, and light gray spheres. The table attached to the y axis of the bar chart describes the local atomic configurations. The column labeled "%F" refers to F concentration, and the column labeled "db" refers to whether the F is in the anion dumbbell or not. The family of 0-TM bars correspond to the cases when Li-excess is present. Solid blue bars, striped yellow bars, and dotted gray bars, which are superimposed, show the backward energy, forward energy, and KRA barriers for each local environment. For symmetric local environments, a single vertically striped green bar is used because the forward, backward, and KRA barriers are equal. See Figure 2-S1, 2-S4, and 2-S6 for the corresponding MEPs.

The asymmetry around the dumbbell in hops a–c causes the migration path for Li to bend toward the 0-TM tetrahedral channel rather than go straight through the dumbbell (ODH path) (Figure 2-1a). Such 0-TM channels are more likely to be found when Li-excess is present, which is facilitated by the incorporation of fluorine. The kinetically-resolved barriers are similar (270 meV, 310 meV, and 340 meV) independent of the amount of F or its position in the local environment, though the KRA's are clearly somewhat higher when F is present in the dumbbell. Cases d–f are a family of 1-TM channel hops which are more likely to be found when there is no Li-excess nearby. Configuration d is the reference single vacancy ODH in o-LiMnO$_2$, which has a barrier of ~500 meV (Figure 2-1a). When 1O atom coordinating the final site of the migration is replaced with F (environment e), the forward barrier remains approximately the same as in the

11

pristine structure (490 meV), consistent with the fact that the initial state environment and the anion dumbbell occupation has not changed. The backward barrier in this environment is lower as the vacancy environment prefers F rather than O as one of its neighbors. However, when the F atom is substituted for one of the O atoms in the anion dumbbell (environment f), the KRA increases to ∼640 meV, demonstrating the barrier's dependence on the location of the F along the path. In both cases where 1 F has been added (environment e and f), the path bends slightly to avoid the anion dumbbell, which results in a path lying in between the ODH and the TSH pathways. This type of trajectory is shown with slightly curved blue arrows to distinguish them from the ODH and TSH mechanisms.

Several additional influences on the migration barrier can be extracted from the data in Figure 2-2. Comparing configurations d *vs.* a and f *vs.* b shows that the presence of Li-excess greatly decreases the barrier by more than 200 meV, which is in line with previous results showing that 1-TM channels are 200–300 meV higher in energy barrier than 0-TM channels. [14]

By comparing d *vs.* f and a *vs.* b, it is apparent that the effect of F itself on the energy barrier is negative (*i.e.* results in higher migration barriers) but that the decrease in barrier from nearby Li-excess outweighs the increase in barrier from F, resulting in an overall decrease in the barrier when both F and Li-excess are present (b *vs.* d).

By comparing configurations f *vs.* d, we can quantify that the increase of the KRA barrier when fluorine is added to the dumbbell in a 1-TM path is 140 meV. In contrast, when adding F to a 0-TM path, as in going from configuration a to b, the barrier increases by only 40 meV. Note that the purpose of this comparison is not to quantify the barriers exactly but to demonstrate that the increase of the migration barrier due to the presence of F is larger in the 1-TM channel than in the 0-TM channel. The origin of this variation of barrier increase with F can be elucidated by inspecting the actual migration paths in Figure 2-S4. For a 0-TM path the migrating Li can "escape" from the F in the dumbbell by bowing the path more into the 0-TM tetrahedron, thereby lessening the negative effect of F on the barrier. This is not the case for a 1-TM path where the repulsion with the TM keeps the migrating Li close to the F in the dumbbell. This analysis shows that increase of barrier by F is not constant and may depend on the species present in the local environment of the migrating ion, as the negative effect of F is smaller when Li-excess is present.

NEB calculations are subject to the errors of DFT calculations. [71] Though the accuracy of DFT barriers has never been firmly established across a large set of structures and chemistries, based on our experience, we estimate that the calculated migration barriers have an error bar of ∼0.1 eV. [72] In a recent study, it has been mentioned that the experimental error of activation barriers across different labs is about 128 meV for known conductors. [73] However, given that we compare barriers in similar structures and chemistries, we expect our relative differences to be more accurate than 0.1 eV.

2.3.3 Divacancy diffusion mechanism in presence of F and Li-excess

We also investigate the effect of F on a number of divacancy diffusion pathways. Figure 2-3 shows the barriers for divacancy Li migration in 4 different local environments following the same conventions as in Figure 2-2. Configuration a is the reference divacancy hop for the unfluorinated $LiMnO_2$ oxide with a KRA of 180 meV. Unlike the single vacancy hop in the pristine structure, the divacancy hop usually does not result in equivalent configurations before and after the hop, except in the most symmetric structures. Hence, the forward and backward diffusion barriers differ

(also shown in the MEP in Figure 2-S2), and the KRA is the most relevant quantity to extract. [25] Configurations b and c correspond to hops with F in different locations around the endpoint of the trajectory, while configuration d has F in the anion dumbbell and is shared among the polyhedra defining the initial, final, and intermediate sites. Most KRA barriers are in the range of 200 meV when no F is present in the dumbbell. With F in the dumbbell the KRA is significantly higher (configuration d), similar to what is observed for the single vacancy migration mechanism.
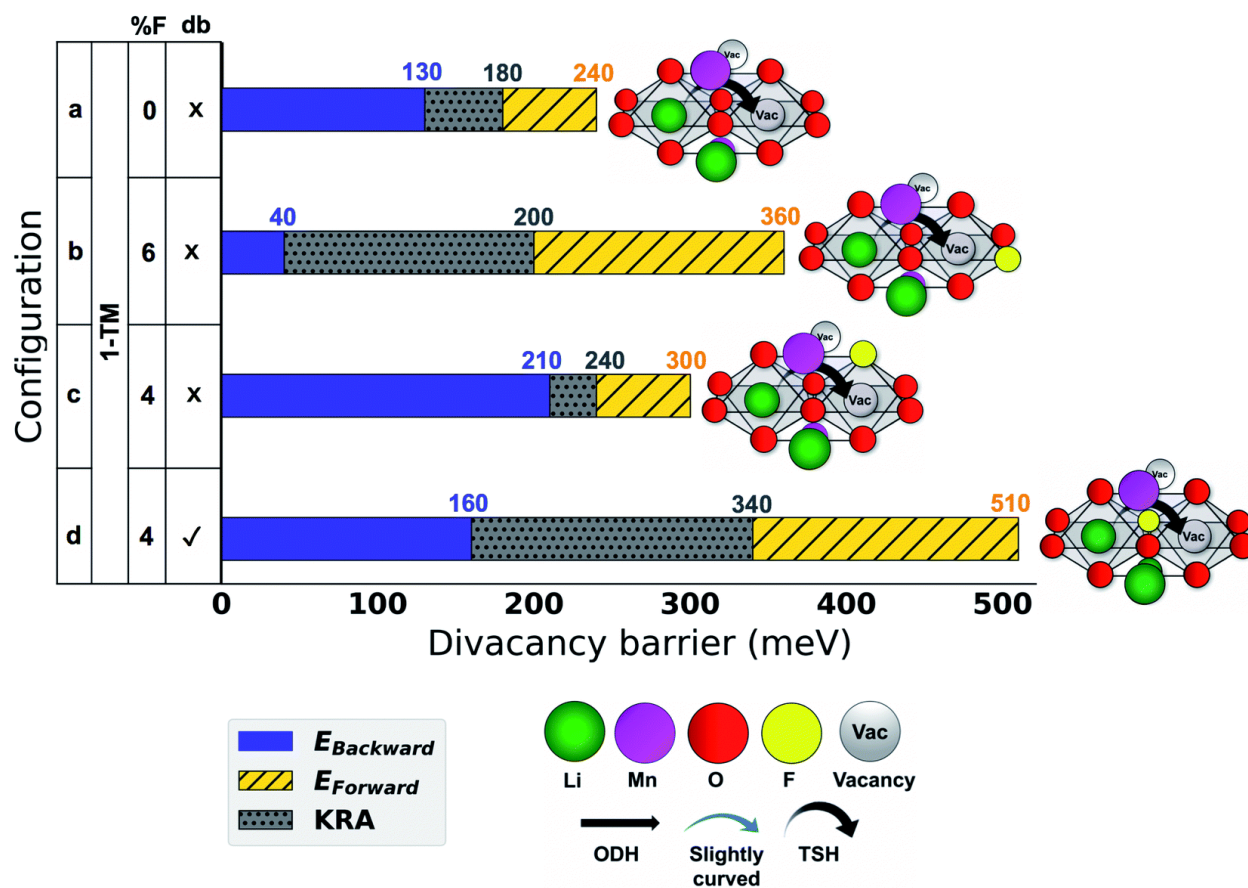
Figure 2-3 Horizonal bar chart showing the divacancy migration barriers for various local configurations around a migrating Li. The black arrows in each of the atomic configurations show schematically the Li trajectory obtained from NEB relaxation. Li, Mn, O, F, and vacancy are shown as green, purple, red, yellow, and light gray spheres. The table attached to the y axis of the bar chart describes the local atomic configurations. The column labeled "%F" refers to F concentration, and the column labeled "db" refers to whether the F is in anion dumbbell or not. Solid blue bars, striped yellow bars, and dotted gray bars show the backward, forward, and KRA barriers for each local environment. Figure 2-S3 compares the MEP of the pristine structure (configuration a) with the 4% F structure (configuration d).

2.3.4 F bonding preferences

Our previous results have focused on the barriers of Li migration in various local atomic configurations. When the initial and final sites are not equivalent, their Li site energy difference contributes to the barrier negatively or positively depending on the direction of the jump. It has been previously reported that in cation-filled rocksalts F prefers coordination to Li rather than to TM due to the high energy of TM–F bonds, [24,57] but it has not yet been investigated how F will interact in the presence of both Li and vacancies. To better understand the effect of F on Li site energies and Li transport, we additionally investigate the bonding preferences of F through both NEB results and the calculation of vacancy formation energies in varying configurations.

Figure 2-4 shows NEB calculations for Li diffusion *via* the single vacancy mechanism when a single F is substituted for an O on varying anion sites (labeled p1–p10) around the diffusing Li ion. Migration paths p1 and p6 have a F in the anion dumbbell and the highest KRA barriers. This is in line with our previous results showing that the substitution of an F in the anion dumbbell increases the barrier more than the substitution of F in other locations. Moving the Li atom from an initial state without F bonding to a F-bonded final state increases the energy as observed for migration in configurations p2–p5. In migration paths p7–p10, the Li escapes from the F-bonded higher energy initial site to the non-F bonded lower energy final site. These results indicate that fluorine prefers coordination by the vacancy rather than by Li in this system. Hence, jumps whereby Li moves towards a F will have a higher barrier than the reverse jumps. As shown in the horizontal bar chart in Figure 2-4 (right), the KRA of all positions of F are almost the same ($\sim$500 meV), except configurations with F in p1 and p6 which have about 100 meV higher KRA ($\sim$600 meV) than other positions.
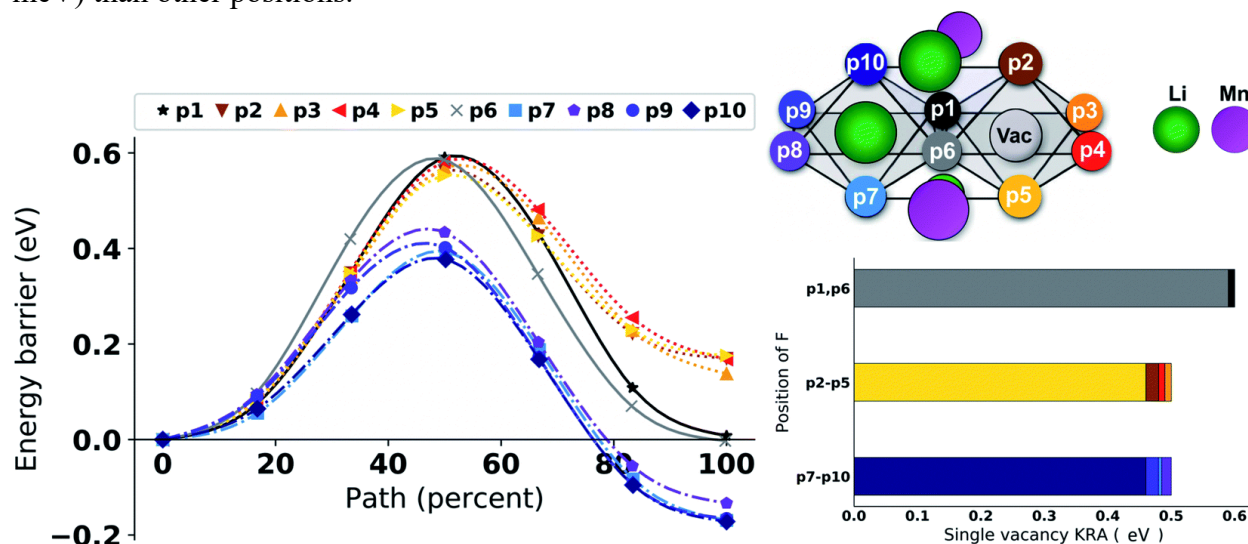
Figure 2-4 Li hopping in single vacancy mechanism (out-of-plane, ODH hop) with a single F in varying sites around the migrating Li. 1F is substituted for O in different anion sites (p1 to p10 in the atomic configuration inset). The family of blueish lines correspond to paths where F is bonded to only the initial state of the diffusing atom, the family of yellowish/brown lines corresponds to the paths where F is bonded to only the final state, and the black/dark gray lines correspond to the

paths where F is bonded to both the initial and final states. The green and purple circles in the inset correspond to Li and Mn, respectively. A horizontal bar chart corresponding to KRA of p1 to p10 are plotted to the right of the figure.

In order to confirm our findings on F bonding preferences, we also evaluate the voltage required to remove a Li (create a Li vacancy) at increasing distance from a F. Figure 2-5 demonstrates that it requires increasing voltage to remove a Li (create a vacancy) as the removed Li is at increasing distance from F, confirming that F stabilizes vacancies in its near neighbor shell.
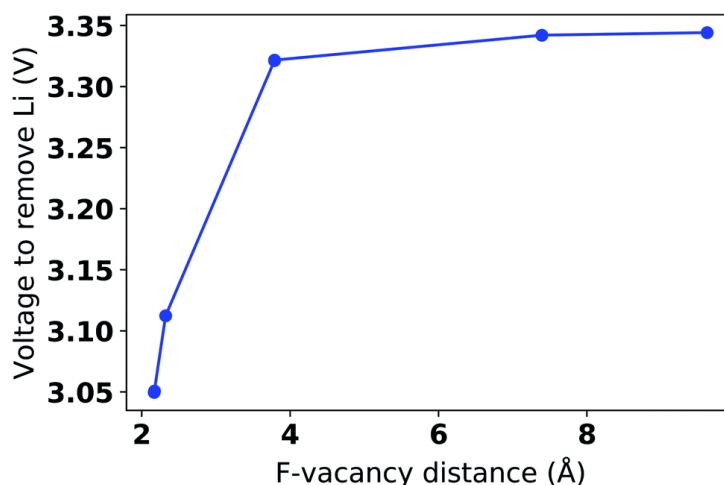
Figure 2-5 Voltage (V) required to create a Li-vacancy as a function of distance of the vacancy to the F anion in a ~2% fluorinated supercell of o-$LiMnO_2$ ($Li_{65}Mn_{63}O_{126}F_2$).

2.4 Discussion

We investigated the effect of fluorine substitution on Li migration and Li site energies in o-$LiMnO_2$ as a prototypical Mn-based cathode material that contains different local environments representative of those that can be found in disordered structures. Figure 2-6 compares the energy barriers in our model system with computed data available in literature for well known intercalation materials, including layered ($LiMO_2$ for M = Ti, V, Cr, Ni,[74] Co, [34] $Li(Ni_{0.5}Mn_{0.5})O_2$,[27] and $Li(Ni_xMn_yCo_z)O_2$ (NMC) [75]), spinel ($Li_{1+x}Mn_{2-x}O_4$ (x = 0, 0.125), [76] Li_xTiS_2, [54] and $LiNi_{0.5}Mn_{1.5}O_4$), [77] and olivine (LiM(=Mn, Fe, Co, Ni)PO_4 [78] and $Li_{1+x}Fe_{1-x}PO_4$, which contains Li-excess on the Fe sites of $LiFePO_4$) [79] systems. As Li migration barriers depend on various environmental factors, we indicate with polygons where variations in the barrier originate and with a double star adjacent to the structure name which materials are disordered, as the local environments vary greatly in these systems. We also depict the type of hop using differently colored bars.
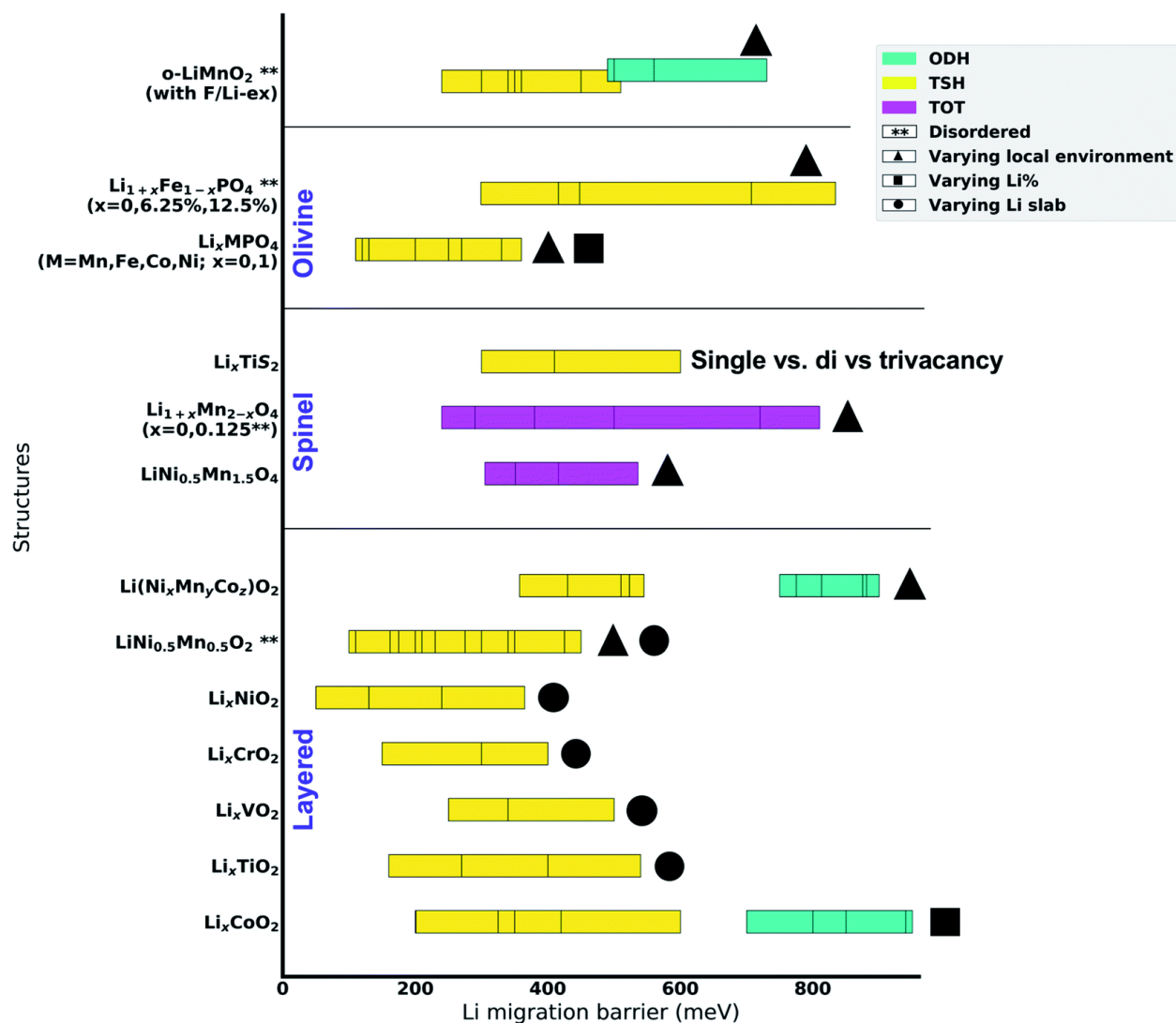
Figure 2-6 Comparison between activation barriers of the model system (o-LiMnO₂ with and without F/Li-excess) via both ODH and TSH mechanisms with available migration barriers for ODH and TSH mechanisms for various delithiated states of different layered, spinel, and olivine systems in literature. The barriers for ODH, TSH, and tetrahedral to octahedral to tetrahedral (TOT) paths are shown as turquoise, yellow, and magenta bars respectively. Double stars (**) next to the name of the structure indicate a disordered structure. In the case of $Li_{1+x}Mn_{2-x}O_4$, only the Li-excess phase (x = 0.125) is disordered. The polygons near the bars (triangle, square, and circle) specify where variations in the barriers come from (varying local environment, Li concentration, and Li slab space, respectively).

According to Figure 2-6, the range of migration barriers for TSH mechanism in our model system (~240 meV to ~500 meV) overlaps with TSH barriers for the LiCoO₂ (~200 meV to ~600 meV) and NCM (~357 meV to ~545 meV) cathode materials. In our model system, the ODH mechanism (~490 meV to ~730 meV) typically results in lower migration barriers than in

LiCoO$_2$ (~700 meV to ~950 meV) and NMC (~750 meV to ~900 meV) which can be explained by differences in structural geometry (orthorhombic *vs.* layered) and chemistry of these materials.

Furthermore, the overall range of barriers calculated in our model system (~240 meV to ~700 meV) is very similar to range of barriers in stochimetric and Li-excess spinel Mn oxides (~240 meV to ~810 meV). It is important to note that the migrating Li-ions always take the path with lowest activation barrier in order to percolate throughout the structure. However, since there is not much information available about how the disorder in these specific systems (such as Mn-based Li-excess spinel) affects the percolation path, we compare the overall range and distribution of barriers. The similar overall ranges between the model system and Li-excess spinel oxides thus further supports our finding that effect of F incorporation on Li diffusion is not expected to be significant and that the migration barriers calculated in this work remain in a reasonable range.

One of the main factors that result in having high power density is to have high Li-ion diffusivity. [27,75] The diffusivity of successful commercialized cathodes such as LiCoO$_2$ is around 10^{-12} to 10^{-11} cm^2 s^{-1}. [80] If we assume a hop distance of 3 Å for Li-ions and a vibrational prefactor of 10^{11} to 10^{12} s^{-1} in a simple random walk model for diffusivity, the diffusion coefficient needed to (de)lithiate a 1 micron particle in 1 h (estimating diffusion distance as the square root of the diffusivity x time) is associated with an upper range of acceptable activation barriers of ≈400–450 meV. Most of the migration barriers for the TSH hop in our model system are below 450 meV, including single vacancy barriers in the presence of Li-excess (Figure 2-2, environments a, b and c) and all divacancy mechanisms except one with F in the anion dumbbell (Figure 2-3, environments a, b, c). These low migration barriers indicate that Li will likely be able to find a percolation path through the lower-energy hops as long as TSH mechanism becomes available.

Our findings show that F substitution modifies the migration barrier, path, and site energy. Together with the Li-excess that can be co-introduced with F substitution these form an interrelated set of effects which we have tried to deconvolute in this work by evaluating the barrier when the local environment is systematically modified. We find that, when all else remains identical in the environment, the substitution of F for O tends to raise the Li migration barriers somewhat, with the strongest increase occurring when F is substituted in the anion edge (dumbell) that is shared between the anion octahedra coordinating the final and initial Li site. The most significant increase of KRA is found for single vacancy migration with 1-TM tetrahedral configurations present around the path (Figure 2-2, environment f), as the presence of TM on both the tetrahedral channels as well as the F in the dumbell create a highly constrained environment for Li to migrate through. But the high activation energy for this mechanism makes it all but irrelevant even in unfluorinated compounds. The effect of F in the dumbell on the single vacancy barrier is significantly mitigated when a 0-TM tetrahedron is present around the migration path as it allows the path to bow away from the F-containing edge (Figure 2-2, environment b). In the latter environment, F in the dumbell only increases the KRA by 40 meV, as compared to an increase of 140 meV when no 0-TM environment is present (Figure 2-2, environments f and d). Hence, Li-excess or appropriate short range order (SRO), [81] which create 0-TM environment is an important aspect of mitigating the effect of F on the migration barrier

We confirm that the barriers for the divacancy mechanism are considerably lower than for the single vacancy migration, consistent with the literature, [53] but also increase the most when F is present in the anion dumbell shared between the initial and final state octahedron. When F is present in sites that only coordinate the initial or final cation site, the path becomes asymmetric

with only a small increase in the KRA. While we only showed 1-TM divacancy hops in Figure 2-3, we also investigated the divacancy mechanism with a 0-TM channel with presence of F in the anion dumbbell (Figure 2-S8) and find that the octahedral sites are unstable and relax into the tetrahedral site. Euchner *et al.* has reported a similar observation in V and Ti disordered rocksalt materials in the presence of only Li-excess and two or more vacancies. [82] Previously, in a study that investigated the 0-TM diffusion barrier in special quasi-random structures (SQS) of fluorinated $LiTiO_2$, it was found that the combination of Li-excess and fluorination also resulted in a stronger stabilization of the tetrahedral site compared to Li-excess alone. [52] The stabilization of the tetrahedral site may be assisted by the two octahedral vacancies near F that it creates. Because the tetrahedral site is only stabilized by $\approx$150 meV over the octahedral sites, this site shift is not expected to impede Li migration.

The effect of F^- on the transition path and site energy can be rationalized from its different electron configuration compared to O^{2-}. Its lower negative charge results in less attraction to the Li^+ cation to compensate for the Pauli (steric) repulsion between the ions. This net repulsion is responsible for the single vacancy migration path bowing out but not bending completely into the tetrahedral site when F is in the anion dumbbell (Figure 2-2). It also explains the net attraction of F to a vacancy which creates asymmetry in the forward and backward path of jumps. In addition, the lower polarizability of F^- compared to O^{2-} limits its ability to screen Li^+'s repulsion from other cations resulting in a higher site energy and generally higher barriers.

While the presence of F has a small negative effect on Li migration, Li-excess is found to drastically decrease the migration barrier by transforming 1-TM channels into 0-TM channels, which reduces the diffusion barriers for both single vacancy and divacancy diffusion mechanisms. Comparing configurations d *vs.* a and f *vs.* b in Figure 2-2 shows that the presence of Li-excess decreases the barrier by more than 200 meV, which is in line with previous results showing that 1-TM channels are 200–300 meV higher in energy barrier than 0-TM channels. [14] While it is generally assumed that Li migration occurs through divacancies we find that in a Li-excess environment (0-TM channels) even the single vacancy mechanism may be active, as its KRA values are of the order of 300 meV, which is low enough for them to actively contribute to Li transport in the cathode material. This may be particularly important at the end of discharge where vacancies are scarce which may make the divacancy diffusion mechanism inaccessible.

To make an overall assessment of the effect of fluorination on Li transport one needs to combine both its effect on the percolation as investigated in other work [52] and its effect on local migration barriers. Previous work showed that for oxides with good 0-TM percolation, at fixed Li-excess, small amounts of F lower the percolation of 0-TM channels, whereas amounts above 15% improve percolation. However, for oxides with poor 0-TM percolation, fluorination should always be beneficial. [52] Because we find that Li migration through 0-TM environments is minimally affected by F substitution it is possible to conclude that no large changes in bulk Li diffusion rates should be expected when DRX materials are fluorinated.

Our results indicate an interesting possible trade-off between rate and stable capacity in fluorinated materials. If F substitution in the material is used to increase the Li-excess content, then the combined effect is likely to be highly favorable for Li transport as the increase in Li-excess will outweigh the small effect of F on the barriers. In contrast, when fluorination is used to increase the TM redox capacity, as originally intended, [57,83] its effects on rate will depend strongly on the amount of Li-excess already present.

Finally, our results also indicate some potential complications that can arise with F incorporation. The attraction of F to the single Li vacancy may trap vacancies at dilute concentrations, which indicates that a small amount of F might impede Li transport at early stages of charge. If the F content is high enough for F ions to share vacancies, then this effect is likely to be diminished. A quantitative evaluation of this effect would require more extensive kinetic studies similar to those performed for Li_xCoO_2, [25,34] but the complexity of this system with its disorder over multiple cation and anion components will make this challenging. SRO has been observed in disordered rock salts and has been argued to affect the amount of percolating Li. [52,84] However, to our knowledge there is no strong evidence of ordering or inhomogeneity on the nanoscale.

Somewhat surprisingly, we find in our work barriers of some 1-TM channels that are low enough to participate in Li diffusion. We believe that this is a result of our choice of model system. While o-LiMnO$_2$ has multiple distinct environments, making it a useful system to study the environment dependence of the barrier, the height of the tetrahedral site in o-LiMnO$_2$ is approximately 2.53 Å while the typical tetrahedron height in a disordered rocksalt structure is shorter and typically below 2.40 Å. [14] This height of the tetrahedron has been show to influence in particular the 1-TM barrier (but less so the 0-TM barrier). [14] Hence, 1-TM channels are probably somewhat disproportionally favored over 0-TM channels in our calculations.

Our calculations focused on the Mn systems, but recent work has found that there may be significant differences in the effect of F arising from the TM metal chemistry. [82] While the reason for this chemistry dependence is not clear, it is possible that chemistry modifies the geometry of the path. As our results indicate, the impact of F on the barrier is less significant when the migrating Li can evade F by bowing into the tetrahedral site, which would be much easier in larger tetrahedral sites. In that context, Euchner *et al.* [82] point at the potential reduction of the TM at the gate site as an important variable to affect the barrier, Such an electrochemical process would lead to F having chemistry dependent effects on the barrier.

In this work we have only looked at the Li diffusion in the early stages of charge where there is no oxygen oxidation. At the end of charge, due to oxygen oxidation, there might be some effect on Li mobility although that effect would likely be less important in F-substituted materials.

2.5 Conclusions

In this work, we used first principles calculations to investigate the impact of fluorine substitution on the Li migration energy in orthorhombic LiMnO$_2$ as a model for Mn-based DRX systems. While our results show a small increase in most kinetically resolved barriers in the proximity of F, they are mostly negated in the presence of Li-excess. Hence, one can expect that systems that are 0-TM percolating will have reasonable Li transport, with or without F in the composition.

2.6 Supporting information
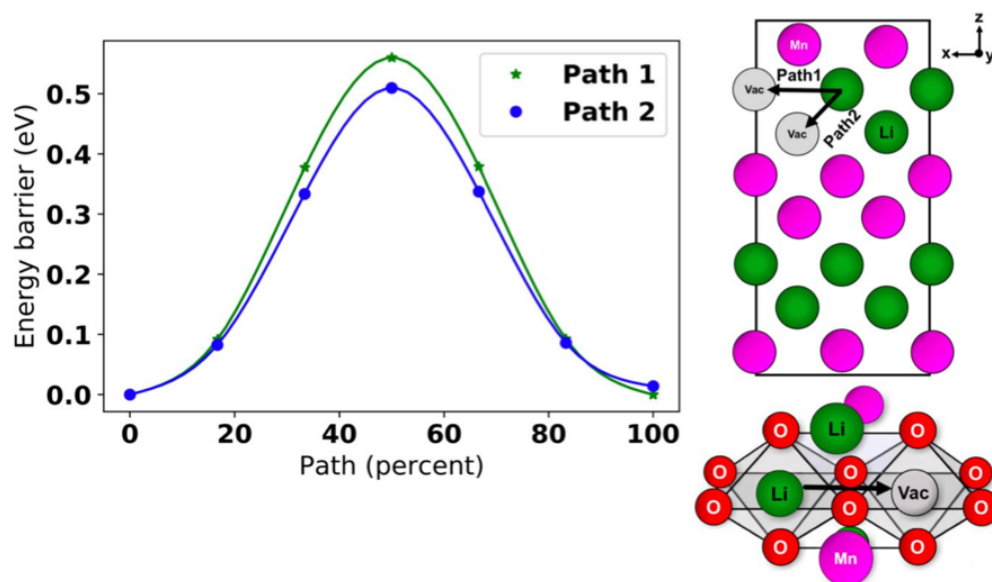
Figure 2-S1 (left) Energy (eV) along the two possible paths (%) for a single vacancy mechanism in o-LiMnO2. The in-plane hop (path 1) is shown in green with stars, and the out-of-plane hop (path 2) is shown in blue with filled circles. **(bottom right)** Magnified depiction showing the nearest neighbor cations along both paths. **(top right)** Atomic configuration demonstrating the Li hops, which occur along the trajectory shown by the black arrow along the (010) plane.
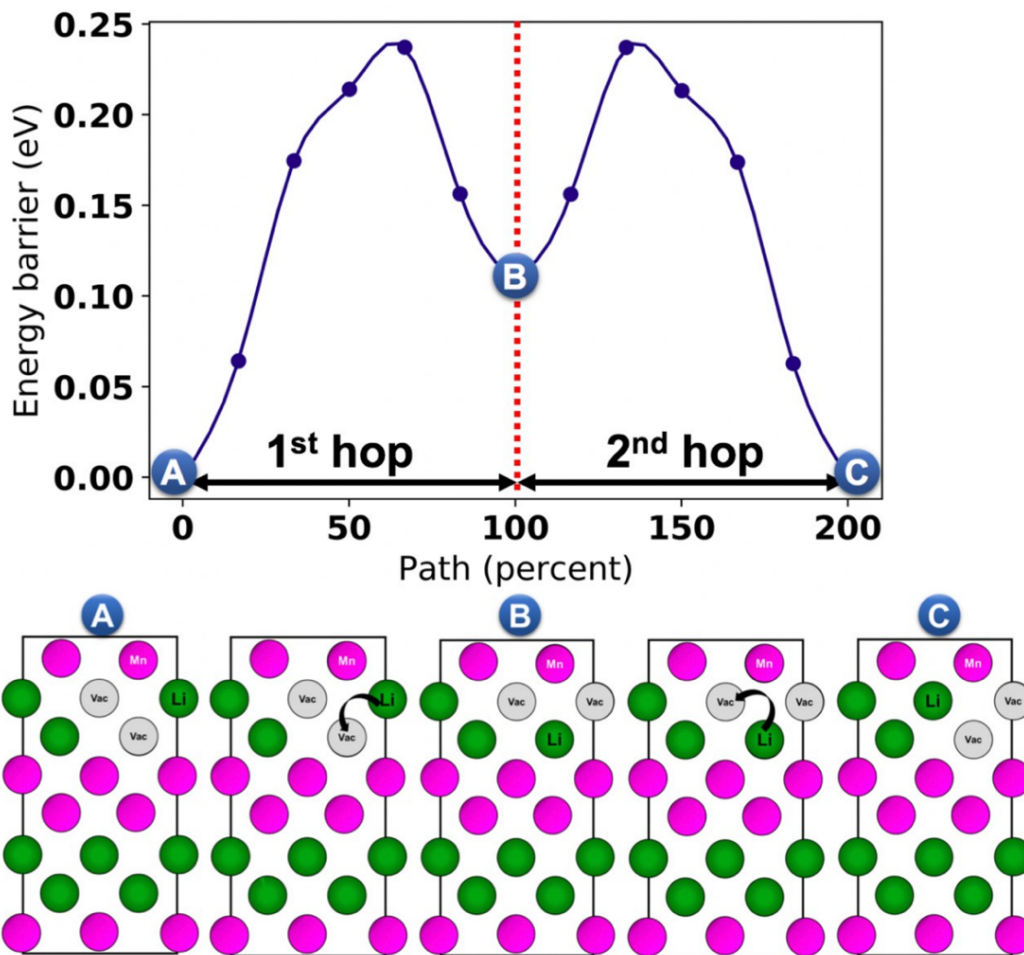
Figure 2-S2 (top) Energy (eV) along Li migration path (%) consisting of two separate hops that constitute a full percolating path using the divacancy migration mechanism in o-LiMnO2. **(bottom)** Atomic configurations of the hops before, during, and after the hops. Green, purple, and gray circles represent Li, Mn, and vacancies. O atoms are not shown for clarity. Position A in both top and bottom figures correspond to the case when two vacancies are not in the same plane but share an edge, while position B corresponds to the case when the vacancies are in the same plane. Position C is symmetrically equivalent to position A.
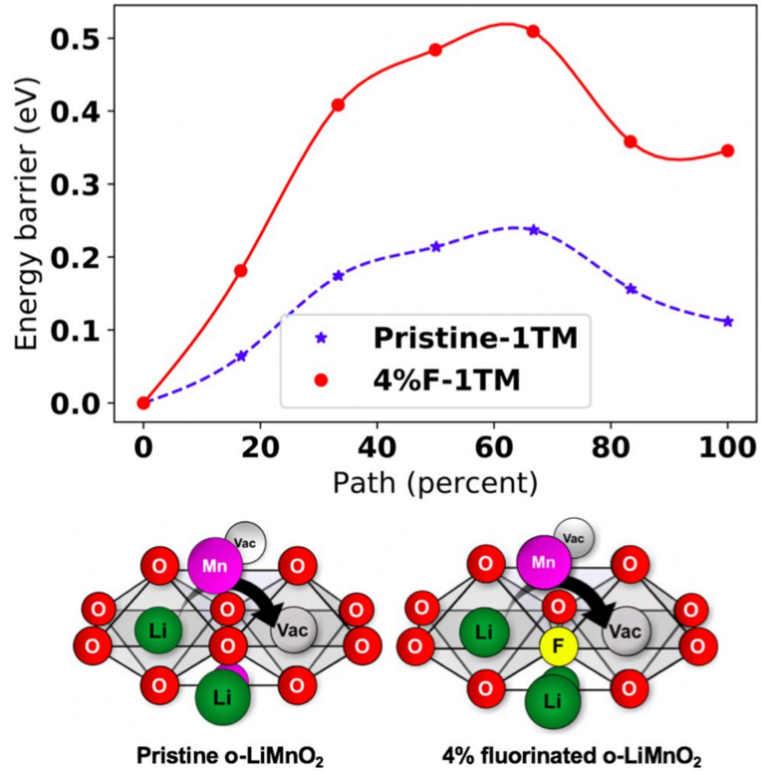
Figure 2-S3 Energy (eV) along Li migration path (%) for 1-TM divacancy Li migration mechanism in pristine (dotted blue line) and 4% fluorinated o-LiMnO2 (solid red line marked with filled circle). Atomic configurations are shown below the graph. Green, purple, red, yellow, and light gray show Li, Mn, O, F, and vacancy respectively.
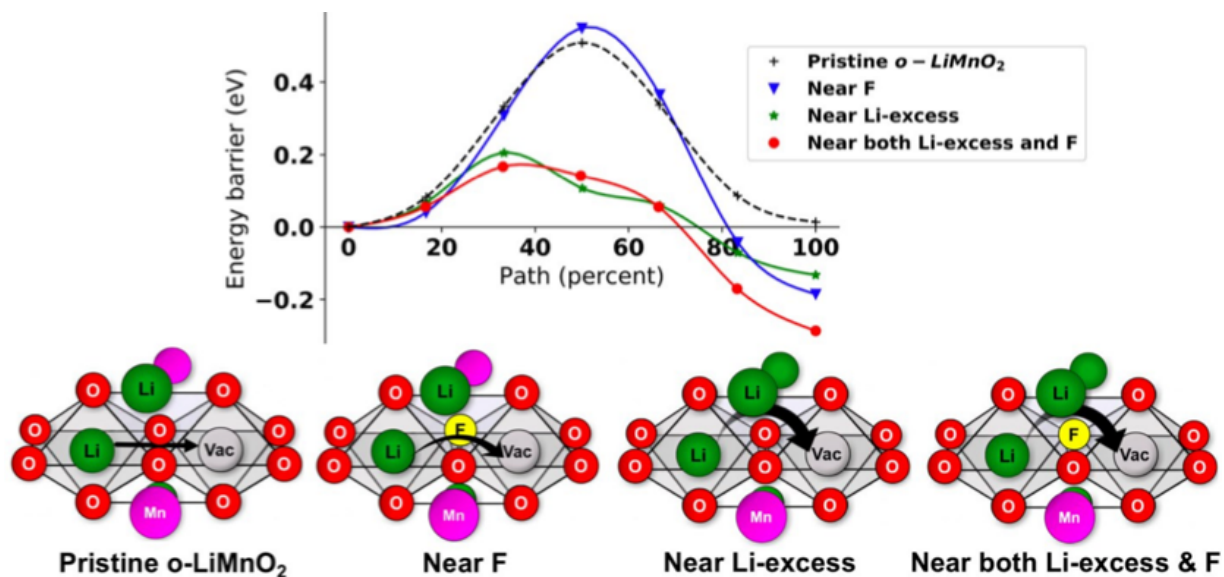
Figure 2-S4 Energy (eV) along Li migration path (%) for single vacancy migration mechanism for cases when the migrating ion is in pristine o-LiMnO2 (black dashed line, marked with plus sign), near F (solid blue curve, marked with triangle), near Li-excess (solid green curve, marked with star), and near both F and Li-excess (solid red color, marked with filled circle) from one octahedral site to another octahedral site. Atomic configurations are shown below the graph. Green, purple, red, yellow, and light gray show Li, Mn, O, F, and vacancy respectively. The black arrows on the atomic configurations correspond to the migration trajectory of the Li ion. Note that the o-LiMnO2 has corrugated Li and Mn layers. Therefore, the initial and final sites of the migrating Li ion have different nearest neighbor cation environments in all cases except the pristine structure.
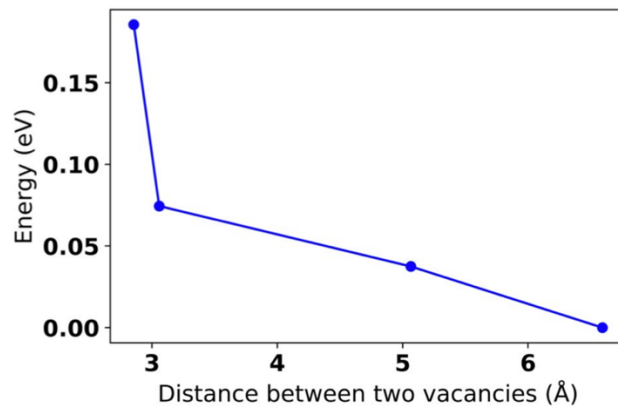
Figure 2-S5 Energy (eV) of two vacancies separated at different distances. All the energies on the y axis are adjusted relative to the energy of the lowest energy configuration which here corresponds to a separation between two vacancies of 6.6 Å.
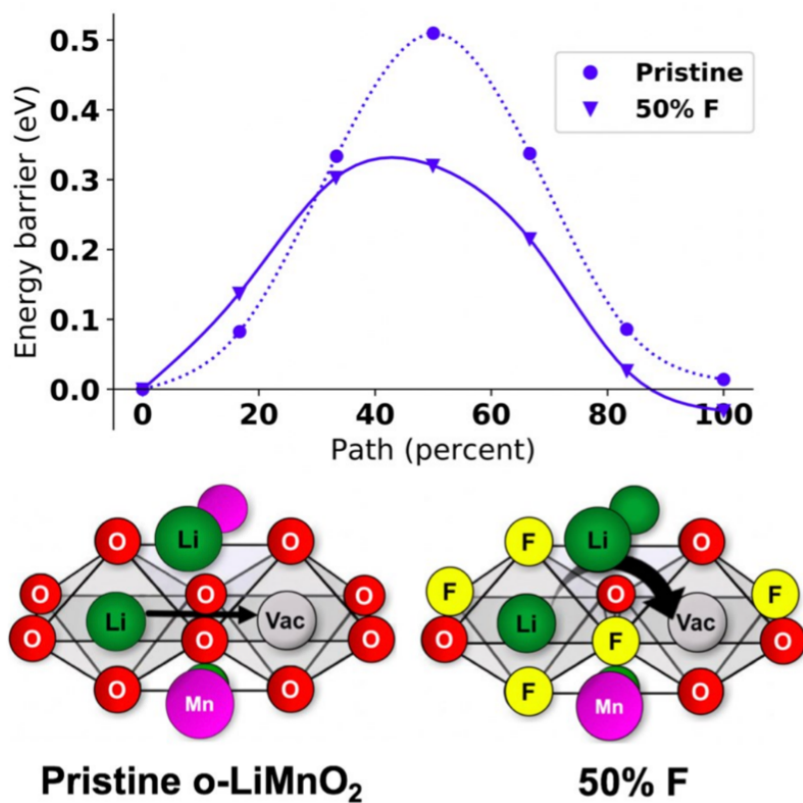
Figure 2-S6 Energy (eV) along Li migration path (%) for 1-TM, out-of-plane hop (solid blue line) single vacancy Li migration mechanism in 50% fluorinated o-LiMnO2. The MEP of the single vacancy migration mechanism for the pristine structure (dotted blue line) is replotted for the purpose of comparison. Atomic configurations are shown below the graph. Green, purple, red, yellow, and light gray show Li, Mn, O, F, and vacancy respectively.
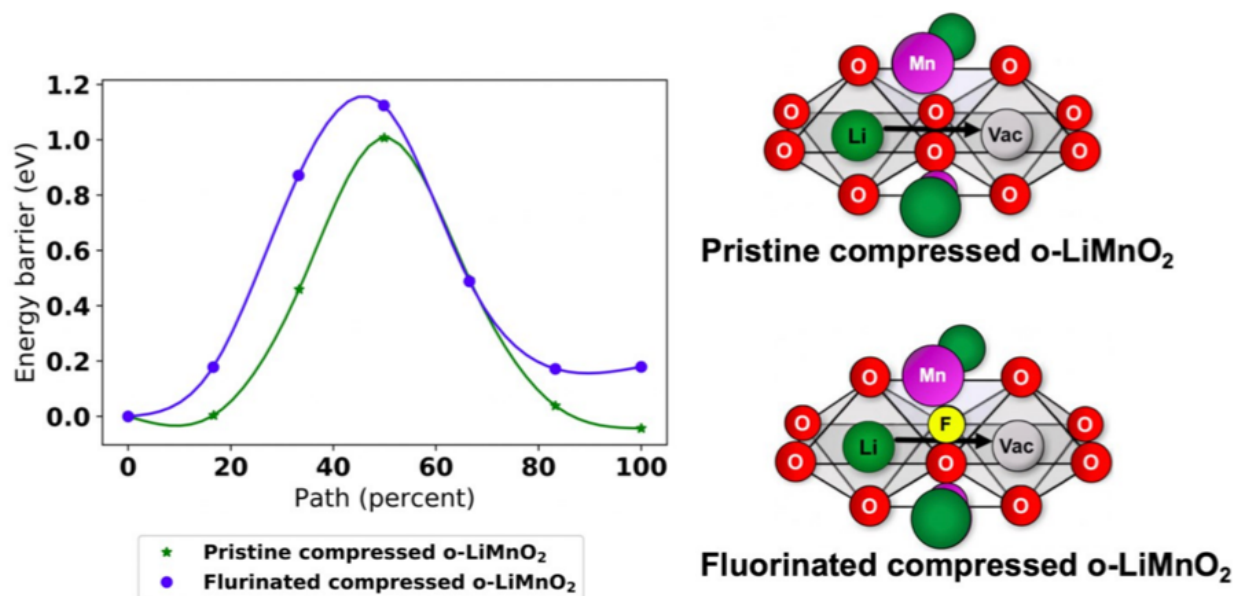
Figure 2-S7 Energy (eV) along Li migration path (%) for 1-TM single vacancy Li migration mechanism in pristine and 3% fluorinated o-LiMnO2 under compression. Atomic configurations are shown on the right. Green, purple, red, yellow, and light gray show Li, Mn, O, F, and vacancy respectively.
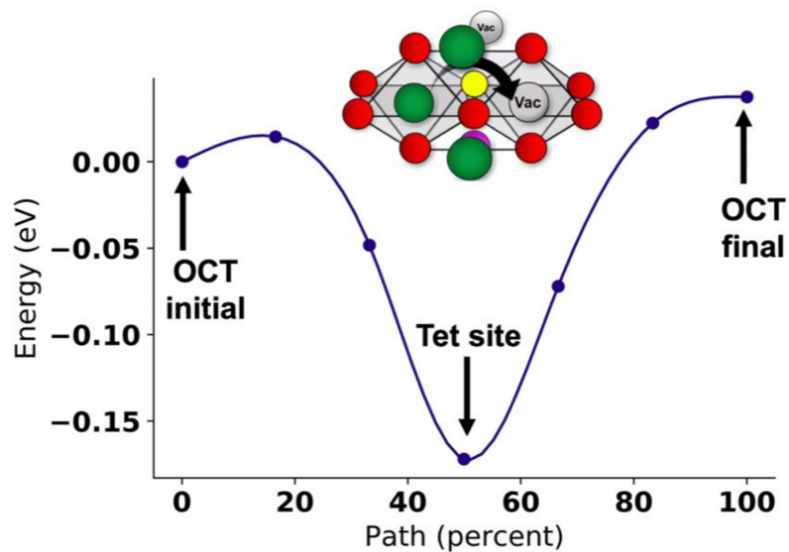
Figure 2-S8 Energy landscapes along the migration path for 0-TM divacancy diffusion in a slightly fluorinated (4% F) o-LiMnO2 structure. Also shown as an inset is the local atomic configurations with the Li trajectory shown by the black arrow in the atomic configurations, with black labels indicating the octahedral initial and final sites and tetrahedral intermediate sites. Li, Mn, O, F, and vacancy are depicted as green, purple, red, yellow, and light grey spheres.

Chapter 3

Ab-initio Study of Short-Range Ordering in Vanadium-Based Disordered Rocksalt Structures[2]

3.1 Introduction

Studies have shown that DRX materials contain cation SRO, an equilibrium phenomenon occurring above the order–disorder transition temperature. [4,84,85] Size and charge affect the degree of cation SRO, which in turn controls the extent of connectivity of the Li_4 tetrahedra in DRX materials: A smaller high-valent TM leads to greater Li segregation into Li_4 tetrahedra clusters compared to a larger high-valent TM. [84] Employing divalent redox-active TMs has also been shown to promote the formation of Li_4 tetrahedra to a larger extent than trivalent TMs. [84]

If these Li_4 clusters are fully connected, a percolating network for facile Li diffusion is formed. [14,15] Controlling cation SRO is therefore important to promote Li percolation [4,84–86] and, subsequently, the amount of accessible Li. [14,15,41,84] The presence of SRO is not specific to DRX materials as it has been studied [87–93] in the field of metallic alloys following the work of J. M. Cowley on Cu_3Au in 1950. [87]

In this paper, we examine $Li_{2-x}VO_3$, $0 < x < 1$, a compound that has been investigated as a potential cathode material [39], to serve as a model system for DRX materials. Our goal is to analyze the delithiation process in the presence of SRO and to determine the specific SRO features that influence the voltage profile in these materials. In Li_2VO_3, Li can occupy both tetrahedral and octahedral sites, whereas V occupies the octahedral sites. We model the configuration space using a lattice cluster expansion trained on first-principles calculations with quaternary disorder ($Li^+/V^{4+}/V^{5+}$ and vacancies) on octahedral sites and binary disorder (Li^+ and vacancies) on tetrahedral sites. To fit the cluster expansion, we use the approach previously applied in a high-component Mn-disordered spinel systems [94–96], which is explained in more detail in **Methods**.

In this study, we find that Li extraction preferentially begins from the octahedral environments with the largest number of nearest-neighbor (NN) V and that the number of NN V dictates the order of delithiation in the remaining octahedral sites, as sites with a higher number of NN V experience higher electrostatic repulsion. In addition, we find that at all stages of delithiation, the number of NN V^{5+}–V^{5+} is minimized.

3.2 Methods

3.2.1 First-principles density functional theory calculations

A cluster expansion (CE) is a formal representation of the dependence of the energy on the configuration of species on prescribed sites of a lattice. [97–99] The structure–energy dataset used to fit the present CE was obtained from density functional theory (DFT) [58,59] using the Vienna ab-initio simulation package (VASP) [63,64] and the projector-augmented wave (PAW) method. [61,62] For these calculations, we used the PBE exchange-correlation functional [60] with rotationally averaged Hubbard U correction, where the U value was selected based on a previously reported calibration to oxide formation energies (3.1 eV for V). [24,100] We used a plane-wave cutoff of 520 eV with reciprocal space discretization of 25 K-points per Å and electronic convergence of 10^{-5} eV with a convergence criterion of 0.01 eV $Å^{-1}$ for the interatomic forces for all our calculations.

3.2.2 Cluster expansion and Monte Carlo sampling

The CE method enables extensive configurational sampling that would not be computationally practical with DFT. The CE is written as:

$$E\left(\boldsymbol{\sigma}\right) = \sum_{\beta} V_{\beta} \left\langle \Phi_{\alpha}(\boldsymbol{\sigma}) \right\rangle_{\beta}, \qquad (3-1)$$

where the occupancy string $\boldsymbol{\sigma}$ represents a particular configuration, with each element σ_i of the string representing an occupation variable for site i. The summation in equation 3-1 is over all symmetrically distinct clusters β, which consist of products of point basis functions. In this work, we used the sinusoidal basis functions as described in Van de Walle et al. [101] The coefficients V_{β} are effective cluster interactions (ECIs) with the multiplicity of the corresponding clusters included, [97,102] and the functions Φ_{α} are cluster functions. [101]

The expansion represented in equation 3-1 can exactly capture any property of configuration when the sum is taken over all possible geometric clusters of sites. However, in practice, the expansion is truncated above some maximum-sized clusters. For our model, based on a cubic cell with a = 3.0 Å, we considered pair interactions up to 7.1 Å and triplet interactions up to 4 Å. We excluded quadruplet clusters from our final CE primarily as their energetics could not be fully sampled with DFT-calculated configurations. Strong electrostatic repulsion makes metal-rich quadruplets dynamically unstable in DFT prohibiting an evaluation of their energy. This insufficient sampling results in a high-rank deficiency of the cluster expansion when quadruplets are included, similar to what has been observed and reported in the cluster expansion of other high-component systems. [103]An Ewald summation term is included in the energy model as it has been shown to increase the accuracy in CE on ionic systems. [24,52,57,104,105]

The lattice model on which a CE is defined requires specification of which species can occupy which sites. As shown in Figure 3-1a, Li_2VO_3 has cubic $Fm\bar{3}m$ symmetry with Li^+ (green) and V^{4+}/V^{5+} (blue) cations occupying the 4a Wyckoff octahedral sites and O^{2-} (red) occupying the anion sites. [39] Li^+ in DRX can also occupy tetrahedral 8c Wyckoff sites. [28,30] Finally, to model delithiated configurations, vacancies (shown in gray) are treated explicitly as species that can also occupy the 4a and 8c sites. In summary, our lattice model for the $Li_{2-x}VO_3$, $0 < x < 1$, configuration space consists of $\{Li^+, V^{4+}, V^{5+}, vacancy\}$ on the octahedral sublattice and $\{Li^+, vacancy\}$ on the tetrahedral sublattice.

The initial set of configurations used to fit the CE consisted of Monte-Carlo-sampled configurations with low electrostatic energy using an Ewald-only Hamiltonian. [106] This initial dataset was used for the typical iterative approach of fitting, adding new low-energy Monte-Carlo-sampled structures from the fit and re-fitting with the newly generated structures until convergence. [107,108] Monte Carlo sampling is performed at varying Li compositions ($Li_{2-x}VO_3$, $0 < x < 1$), temperatures (300 K–5000 K), and supercell sizes ranging from 3×1×1 (with 3 anion sites) to supercells of 3×4×3, 2×6×3, 2×2×9 (with 36 anion sites) to include a wide energy range of atomic configurations in the space of $Li_{2-x}VO_3$, $0 < x < 1$. By utilizing simulated annealing and comparing our CE results with the DFT, we aimed to determine the ground state of this system. The ECIs of the converged fit are obtained by fitting to the DFT energies of 450 symmetrically distinct structures whose lattice configurations are a subset of possible charge-balanced arrangements of Li^+, V^{4+}, V^{5+}, and vacancies over the cation sublattice.

To build the CE, the smol python package is used. [109] We followed the sequential fitting approach for building multi-cation sublattice coupled cluster expansions previously introduced by Yang et al. [94] For training purposes, 80% of the DFT-computed structures are reserved, while the remaining 20% are utilized for testing. First, V_0, the coefficient of the constant basis function is set to the average energy of the training set, an assumption that holds for sampled centered basis functions. Next, the ECIs for the point-term correlation functions are determined using the lasso regularization approach [110] which is required because the charge-neutrality constraint in ionic systems reduces the dimension (or rank) of the point-term basis functions by one. [94,105] In practice, avoiding degenerate solutions in a rank-reduced space is achieved by setting an ECI for a point-term basis function to 0, which lasso regularization on the point-term correlation functions achieves. Finally, sparse group lasso is applied to solve for the ECI for the remaining correlation functions belonging to pairs and triplets. [94] The resulting fit has a 10-fold cross-validation error of 13.1 meV per site and an in-sample root-mean-squared error (RMSE) of 12.4 meV per site. Figure 3-S1 presents a comparison of the predicted and DFT convex hulls and the ECI values of the converged fit. Based on the cross-validation error, the RMSE, and comparison between the predicted and DFT convex hulls, the CE fit appears to represent the interactions between species relatively well. We discuss some of the specific challenges of fitting this high-component system in the SI, note 1.

To construct a representative topotactic Li voltage profile of the disordered $Li_{2-x}VO_3$, $0 < x < 1$, we use semi-grand canonical MC simulations (SGC MC) from the smol python package [109] at T = 300 K and scan the Li chemical potential, at intervals of 0.05 eV, as a function of the Li content. The Li/V^{4+} metal configuration in the fully lithiated state is obtained by equilibrating at 1800 K in a 9×8×9 cell (i.e., a 648-oxygen supercell with a total of 1296 atoms) using canonical MC to simulate the as-synthesized cation ordering. The topotactic SGC MC at 300 K is then initialized from this fully lithiated configuration and calculated by freezing all V and allowing for

only Li/vacancy disorder and oxidation/reduction of V^{4+}/V^{5+}. We equilibrate for 2 million MC proposals and sample every 2000 proposals, totaling 1 million samples per Li chemical potential.

The voltage profile is calculated from the chemical potential as [68]:

$$V(x) = -\frac{\mu_{Li} - \mu_{Li}^{reference}}{Z}, \qquad (3-2)$$

where μ_{Li} is the Li chemical potential of the cathode material; $\mu_{Li}^{reference}$ is the Li chemical potential of the anode, which we consider to be a pure BCC Li metal (-1.9 eV); and Z is the electron charge carried by one Li ion, $+1e$. The average voltage for the simulated profile is calculated using equation 3-3, with $X_1 = 2$ and $X_2 = 1$ [68]:

$$\bar{V}(X_1, X_2) \approx -\frac{E\left(Li_{X_1}VO_3\right) - E\left(Li_{X_2}VO_3\right) - (X_1 - X_2)E(Li)}{(X_1 - X_2)}, \; with \; X_1 > X_2. \qquad (3-3)$$

For the SRO analysis, we used the pymatgen package [111] to track the species occupying the 12 NN edge-sharing octahedra around each octahedral site (depicted in the top panel of Figure 3-1b) and the 4 NN face-sharing octahedra around each tetrahedral site (depicted in the bottom panel of Figure 3-1b). The species that can occupy these sites include the Li in green, V in blue, and vacancies in gray, as illustrated in Figure 3-1b.
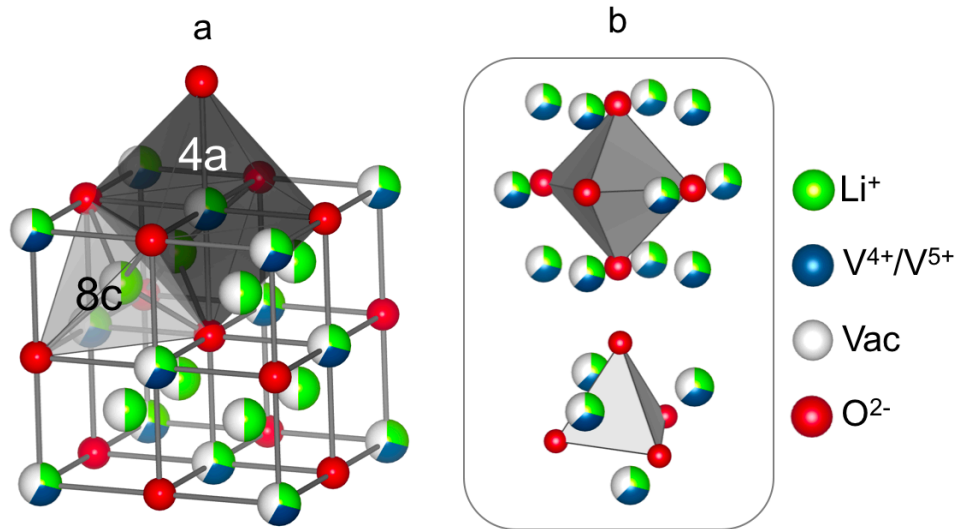
Figure 3-1 (a) Rocksalt structure of $Li_{2-x}VO_3$, $0 < x < 1$ with random cation occupation. The face-centered cubic (FCC) lattice of octahedral sites, which can be occupied by Li^+ (green), V^{4+}/V^{5+} (blue), or vacancies (gray), is represented by the tri-colored spheres. The tetrahedral sites, which can be occupied by Li^+ (green) or vacancies (gray), are represented by the bi-colored spheres. The red spheres form the anion lattice, which is fully occupied by oxygen. **(b)** (top) Schematic of octahedral site surrounded by 12 edge-sharing octahedral sites; (bottom) schematic of tetrahedral site surrounded by four face-sharing octahedral sites.

3.3 Results
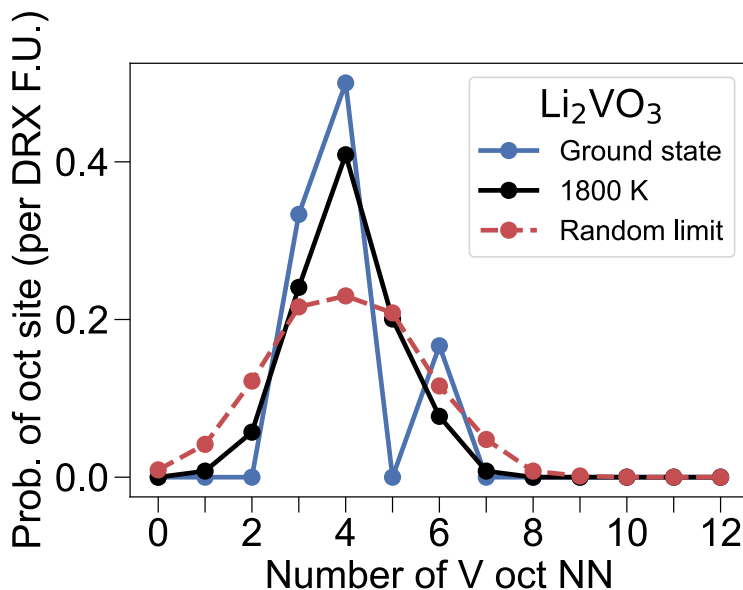
Figure 3-2 Probability that an octahedron has a certain number of V-occupied NN octahedra in the ground state (solid blue curve), at 1800 K (solid black curve), and in the limit of random cation occupancy (dotted red curve). The Y axis is normalized per DRX formula unit (F.U.). Therefore, the sum of the probabilities for each curve (each T) is 1.

The SRO in the as-synthesized $Li_{2-x}VO_3$, $0 < x < 1$ is analyzed in a 9×8×9 cell with the Li/V^{4+} metal configuration obtained by equilibrating at 1800 K. The choice of 1800 K was made because the voltage profile derived from this configuration was found to be the most similar to the experimental voltage profile of Li_2VO_3 when compared to the voltage profiles obtained at lower temperatures, as depicted in Figure 3-S2. Moreover, the simulated X-ray diffraction (XRD) pattern at this temperature (Figure 3-S3) displays only the primary peaks associated with the rocksalt structure (38°, 43°, 63°, 76°, and 80°), suggesting that the simulation temperature exceeds the ordered semi-layered to disordered rocksalt transition temperature. Configurations sampled at temperatures below 1800 K exhibit additional peaks at low angles which have higher intensity than the main rocksalt peak at 43°.

Figure 3-2 shows the probability that an octahedral site in the fully lithiated composition has a given number of NN V (ranging from 0 to 12). The ground state of Li_2VO_3 (blue curve) is a semi-layered structure of Li and Li/V^{4+} layers [112] (shown in Figure 3-S4), in which octahedral Li has 4 and 6 NN V and octahedral V has 3 NN V. For comparison, in a typical layered R-3m $LiMO_2$, such as $LiCoO_2$ or $LiNiO_2$, all the octahedral sites have 6 NN TM. [28] At 1800 K (black), the probabilities of any octahedral site having 3, 4, and 6 NN V decrease, whereas the probabilities of any octahedral site having 1, 2, 5, and 7 NN V sites increase. As the system tends toward the random limit (set to T = 10^5 K in our simulation), we observe the formation of octahedral sites with 0, 1, and 8 NN V, indicating that disordering increases the Li-rich and metal-rich environments compared with those in the semi-layered Li_2VO_3 structure. This result is in line with

SRO analysis using Raman spectroscopy [113] that reveal Li-rich and V-rich domains in disordered Li_2VO_2F, which is a fluorinated isostructural analogue of Li_2VO_3. [39] In the random-limit case (red curve), the probability of the octahedral site environment having a given number of NN V follows an approximately normal distribution with a mean of 4 NN V and a standard deviation of 1.
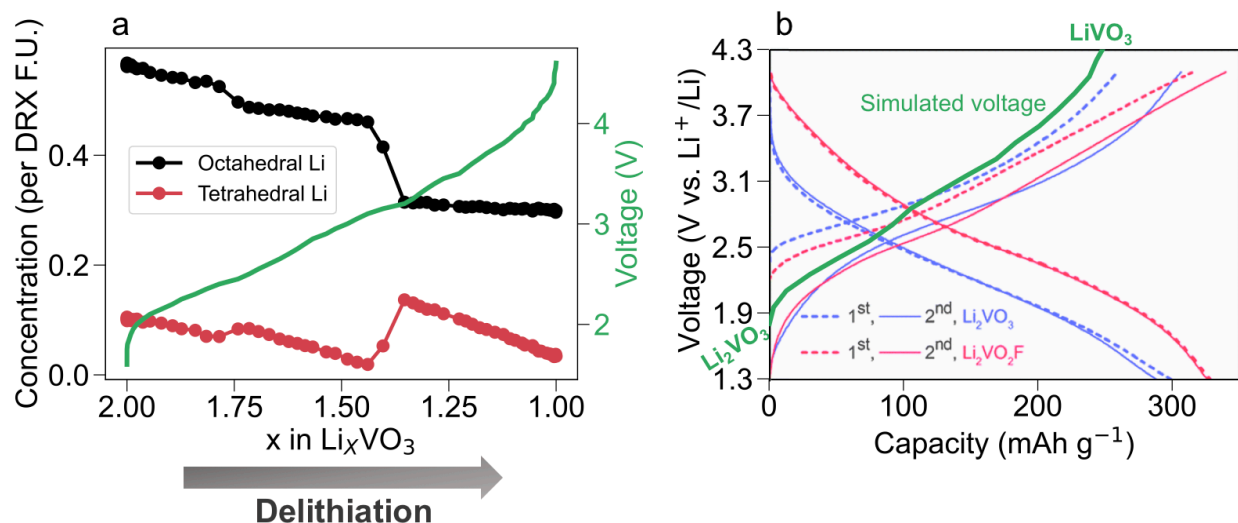
Figure 3-3 (a) Concentration of tetrahedral Li (red) and octahedral Li (black) and the voltage profile (green) as a function of Li content in Li_xVO_3, $1 < x < 2$. The direction of delithiation is indicated by the dark gray arrow under the plot. The Y axis is normalized per DRX F.U. **(b)** Comparison of experimental voltage profiles (blue curves) obtained by Chen et al. [39] and simulated voltage profile of Li_2VO_3 calculated with SGC MC (green curve).

To evaluate the environments from which Li is delithiated, we performed SGC MC simulations and track the concentration of tetrahedral Li and octahedral Li during the delithiation process. Figure 3-3a presents the voltage profile (green) and the concentrations of tetrahedral Li (red) and octahedral Li (black) for a Li_xVO_3 cell with 648 total oxygen atoms for $1 < x < 2$. For all compositions, the concentration of octahedral Li is higher than that of tetrahedral Li, consistent with the rocksalt nature of the material. At the fully lithiated composition of Li_2VO_3, approximately 10% of all Li are in a tetrahedral site. Although most DRX materials are expected to have only octahedral cations in the fully lithiated state, the presence of tetrahedral Li in Li_2VO_3 is not unexpected given that 4% tetrahedral Li has also been observed in the simulated $\sqrt{5} \times \sqrt{5} \times 2$ supercell of $Li_3V_2O_5$ structure. [30] Additionally, the potential for tetrahedral Li formation with varying amount of Li-excess has been demonstrated in the simulation of the fully disordered structure of $Li_{1+y}TM_{1-y}O_2$ $(0 < y < 0.3)$. [28]

Upon delithiation from $X_{Li} = 2$, there is a gradual decrease in the concentration of both octahedral and tetrahedral Li until approximately $X_{Li} = 1.4$. At $X_{Li} = 1.8$, the small increase in the concentration of tetrahedral Li signifies the migration of some octahedral Li into tetrahedral sites. This shift in site occupancies is observed to a much greater extent between $X_{Li} = 1.45$ and $X_{Li} = 1.35$ (voltage range of ~3.1–3.2 V). As delithiation proceeds from $X = 1.35$ to $X = 1$, the concentration of tetrahedral Li quickly decreases, whereas the concentration of octahedral Li remains almost constant, indicating the preferential extraction of tetrahedral Li at high voltage. At the end of the delithiation ($LiVO_3$), most of the remaining Li is in octahedral sites. Having almost

33

all Li in octahedral sites in Li_xVO_3 (x = 1) is consistent with the DFT calculations (Figure 3-S1b), where the configurations with tetrahedral Li are more than 0.1 eV/atom above the hull at $LiVO_3$. Figure 3-S5 offers a spatial representation of these tetrahedral Li ions. Typically, they appear as clusters exhibiting edge-sharing and point-sharing tetrahedral Li formations. This arrangement can be attributed to a driving force to minimize the repulsive interaction between Li ions in tetrahedral positions and Li/V ions in adjacent cation sites.

In Figure 3-3b, the experimental Li_2VO_3 voltage profile obtained by Chen et al. (in blue) [39] is compared with our SGC MC calculated profile (in green). The calculated voltage profile has a slightly steeper slope than the experimental profile of the 1st cycle (dotted blue line). [39] Additionally, the average discharge voltage in the experimental profile is reported to be ~ 2.2 V [39], whereas the simulated voltage profile has an average voltage of 2.9 V, calculated using equation 3-3. This discrepancy between the experimental and theoretical voltage profile is discussed later in this paper.
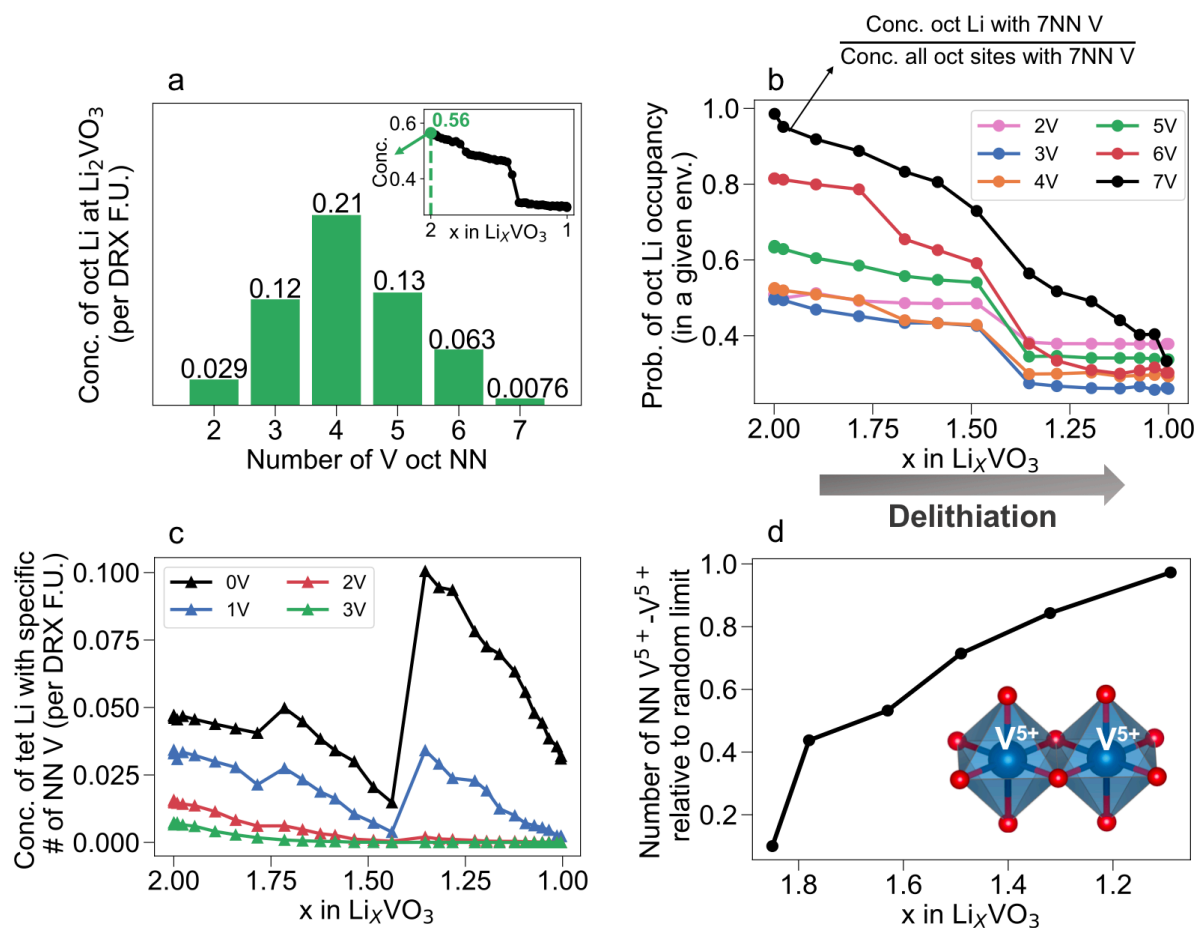
Figure 3-4 (a) Concentrations of octahedral Li at Li_2VO_3 vs. a certain number of V-occupied NN octahedra. The inset shows the concentration of octahedral Li (black) as a function of Li concentration in Li_xVO_3, 1 < x < 2, and the point $X_{Li} = 2$ is marked with a green filled circle. **(b)** Probability of octahedral Li occupancy in a given environment as a function of Li content in Li_xVO_3, 1 < x < 2. Octahedral Li sites with 2, 3, 4, 5, 6, and 7 NN V-occupied octahedra are

represented by the pink, blue, orange, green, red, and black curves, respectively. The probabilities of octahedral Li sites with 0–1 NN V or > 7 NN V are zero and not shown. The dark gray arrow at the bottom indicates the direction of delithiation. **(c)** Concentration of tetrahedral Li that face-share with 0–3 V as a function of Li concentration in Li_xVO_3, $1 < x < 2$. The black, blue, red, and green curves correspond to 0, 1, 2, and 3 NN V respectively. **(d)** Number of NN V^{5+}–V^{5+} relative to the random limit as a function of Li content.

To better understand how disordered Li_2VO_3 is delithiated and how V is oxidized, we analyze the Li and V environments during delithiation in Li_xVO_3, as shown in Figure 3-4. Figure 3-4a shows the concentrations of octahedral Li before any delithiation at Li_2VO_3 as a function of the number of the NN V the Li site has. Altogether, the bars sum to the total concentration of octahedral Li in Li_2VO_3, which is 0.56 per F.U. of DRX and is marked in the inset. Most of the Li (1.68 Li in Li_2VO_3) prior to delithiation are in octahedral sites, so we focus on octahedral Li in Figure 3-4a-b. At the fully lithiated composition, octahedral Li with 4 NN V are the most prevalent, whereas those with 7 NN V are the least prevalent.

To understand how Li is removed, we show in Figure 3-4b the probability (conditional probability) that a site with a certain number of NN V is occupied by Li, as a function of Li content. The total number of octahedral sites with x NN V remains constant as all the V are fixed during topotactic delithiation. The evolution of these curves gives a sense of the environments from which Li is removed at various states of delithiation.

Between $X_{Li} = 2$ and $X_{Li} = 1.45$, the relative contributions to capacity from octahedral sites with 6 and 7 NN V are more significant than those of other environments as their probabilities decrease by more than 0.2, whereas the probabilities of octahedral Li sites with 2–5 NN V decrease by less than 0.1. If there is no preference for how Li is removed (random delithiation), they would be removed at a higher rate from higher frequency environments. Combining Figures 3-4a and 3-4b, we see that although the population of octahedral Li with 2 NN V is higher than those with 7 NN V (from Figure 3-4a), octahedral Li with 2 NN V does not appear to participate in the early stage of delithiation. Thus, while all the octahedral Li environments are extracted to some extent at the beginning of delithiation, there is a clear preference for delithiation of octahedral Li sites with 6 and 7 NN V.

From $X_{Li} = 1.45$ to $X_{Li} = 1.35$, the probabilities of all the environments decrease by comparatively similar amounts, indicating that all the environments participate in the delithiation process. This decrease coincides with the rapid growth of tetrahedral Li and removal of octahedral Li, as shown in Figure 3-3a.

From $X_{Li} = 1.35$ to $X_{Li} = 1$, only octahedral Li surrounded by 6 and 7 NN V continue to be removed. This contrasts with the remaining octahedral sites surrounded by 2–5 NN V whose probability of Li occupation barely changes.

From the data in Figure 3-4b, it is evident that the extraction of octahedral Li is strongly influenced by the number of its NN V. The delithiation preference appears to be in the following order: 7 NN V, 6 NN V, 5 NN V, 4 NNV, 3 NN V, and lastly, 2 NN V environments.

To investigate the environment around tetrahedral Li throughout the delithiation process, in Figure 3-4c, we track the number of V that face-share with tetrahedral Li in the SGC MC simulations. The quantity plotted is the concentration of tetrahedral Li (per DRX F.U.) with a given number of face-sharing (octahedral) V. The black, blue, red, and green curves correspond to concentrations of tetrahedral Li with 0, 1, 2, and 3 V face-sharing.

Figure 3-4c shows that for all Li compositions, face-sharing between tetrahedral Li and octahedral V is uncommon. The concentration of tetrahedral Li decreases as the number of face-sharing V increases, consistent with the expected electrostatic penalty. The observation of dilute concentrations of Li-to-TM face-sharing features is not unique to this study and has been observed in the computational studies of overlithiated $Li_{3+x}V_2O_5$ [29] and Mn-based partially-disordered spinel systems. [95,96]

Upon delithiation, from $X_{Li} = 2$ to $X_{Li} = 1.45$, the concentration of tetrahedral Li decreases in all environments. Then, at $X_{Li} = 1.8$, a small increase in environments with 0 and 1 NN V indicates migration of some Li from octahedral sites to tetrahedral sites. This phenomenon is observed to a greater extent near $X_{Li} = 1.45$, where there is an abrupt increase in the concentration of 0 V and 1 V face-sharing environments. The increase in the tetrahedral Li concentration is consistent with the sudden decrease in the octahedral Li in Figure 3-3a and will be analyzed further in the discussion section.

To study the spatial arrangements that affect V oxidization, we investigate the total number of NN V^{5+}–V^{5+} bonds sampled relative to the random-limit case. To establish these random-limit cases, we sample the V^{5+} ordering during topotactic delithiation occurring at $T = 10^5$ K. Our analysis covers Li compositions ranging from $Li_{1.09}VO_3$ to $Li_{1.85}VO_3$, as shown in Figure 3-4d.

At $X_{Li} = 1.85$, the number of observed V^{5+}–V^{5+} NN pairs is only 20% of what would be present in the random limit. As the concentration of V^{5+} increases, it is no longer possible to avoid the creation of NN V^{5+} environments, and the random limit is reached at $X_{Li} = 1$ where all V is V^{5+}. We reason that the higher electrostatic penalty associated with V^{5+}–V^{5+} interactions is responsible for the low occurrence of NN V^{5+}-V^5 at the early stages of delithiation. This analysis shows that delithiation of Li involves minimizing the number of V^{5+}–V^{5+} bonds to minimize the electrostatic interaction between V.

3.4 Discussion

In this work we modelled the Li extraction from a Li_2VO_3 DRX compound with cation short-range order. We observed that the local environment of Li generally dictates the order in which it is extracted. Quantification of the Li extraction sequence depends on the frequency with which environments are present (as represented in Figure 3-4a) and their tendency to hold on to Li (as represented by Figure 3-4b). The frequency of environments is determined by combinatorial entropy statistics, modified by short-range order, whereas the probably for Li to remain in a specific environment is mostly determined by the interaction of the Li with its environment. Figure 3-4b reveals that during the delithiation, octahedral Li is preferentially removed from environments with 7 NN V, followed by those with 6 NN V, 5 NN V, 4 NN V, 3 NN V, and ultimately from 2 NN V environments. This delithiation order implies there is a repulsive interaction between Li and V, which is consistent with electrostatics dominating interactions even at this very short-range. Li in 2–5 NN V octahedral environments begin to contribute noticeably to the delithiation process at approximately $X_{Li} = 1.45$ (around 3.1 V).

Some tetrahedral Li are also extracted from the very beginning of the delithiation process. In particular, the face-sharing Li-V sites appear to deplete faster than the isolated tetrahedral Li. Critically, we find that the extraction of ~28% of Li ($X_{Li} = 1.45$) results in a noticeable decrease (increase) in the overall concentration of octahedral (tetrahedral) Li, indicating a migration of Li

from octahedral to tetrahedral sites. The same octahedral-to-tetrahedral Li migration has been computationally observed in $Li_{1.44}VO_2F$, a fluorinated isostructural analogue of Li_2VO_3. [114] Such collective migration phenomena are known in ordered spinel compounds [95] but they have so far not been well characterized for cation-disordered materials.

As illustrated in Figures 3-4b and 3-4c, at the end of delithiation Li is extracted from isolated tetrahedral sites and octahedral sites with 6 and 7 NN V, and the remaining octahedral Li sites with 2–5 NN V appear to be electrochemically inactive.

The order in which specific V ions are oxidized seems to be driven by V–V repulsion. Figure 3-4d shows that V^{4+}/V^{5+} are spatially arranged to minimize V^{5+}–V^{5+} bonds until V^{5+}–V^{5+} nearest neighbors become unavoidable at the top of charge. This interaction could be reduced, thereby minimizing the voltage slope near the top of charge, if SRO in the as-synthesized material could be controlled to minimize the number of nearest neighbor V pairs, or by substituting some V by another redox metal that is active at lower valence (reducing the repulsion with V^{5+}).

Our study finds a somewhat steeper voltage slope than observed experimentally. Previous modeling studies have demonstrated that the presence of tetrahedral Li can increase the slope of the voltage profile by displacing capacity from low to high voltage. [28] By definition, it has to do so by leaving the average voltage unchanged as this is only determined by the free energies [28] of the Li_2VO_3 and $LiVO_3$ endpoints. Our study finds a steeper voltage slope than that observed experimentally, suggesting that the concentration of tetrahedral Li in our model system may be higher than that in the synthesized structure. Our average voltage is also somewhat higher than the measured average voltage for Li_2VO_3. [39] Several authors [28,115–117] showed that an increase in disorder can increase the average voltage, suggesting that our theoretical model of the as-synthesized Li_2VO_3 endpoint may be slightly more disordered than the experimental reference. [39]

The cation SRO affects the distribution of Li^+ migration channels throughout the material and thus the macroscopic diffusivity of Li in $Li_{2-x}VO_3$. [39,41] The experimental Li diffusivity in Li_2VO_3 remains mostly constant (10^{-11} cm^{2}s^{-1}) between V = 1.0 V to V = 3.0 V, but rapidly increases to 10^{-10} cm^{2}s^{-1} when charging further to V = ~3.5 V. [39] At higher voltage up to V = ~4.2, the diffusivity decreases again to 10^{-12} cm^{2}s^{-1}. [39] Figure 3-3a shows that at $Li_{1.45}VO_3$ (~3.1 V), the concentration of octahedral Li rapidly decreases and is accompanied by an increase in the concentration of tetrahedral Li. This rapid emptying of the octahedral Li into tetrahedral sites could be the origin of the sudden increase in the experimental diffusivity of the Li_2VO_3 system from 10^{-11} to 10^{-10} cm^2/s observed at ~3.5 V. [39] This suggests that the tetrahedral and octahedral occupancy of Li are close in energy at this composition, which would create a dense network of available sites (with similar energy). Although the migration of Li from octahedral to tetrahedral sites can increase the diffusivity by further delithiation of $Li_{1.45}VO_3$,, overstabilization of Li in the tetrahedral sites can also block migration through tetrahedral sites and reduce the diffusivity at the end of the delithiation process. This analysis is in line with the experimental diffusivity profile of this material. [39] Our cluster expansion is limited to topotactic delithiation and prohibits any migration of V^{5+} ions to tetrahedral sites in order to keep the model complexity reasonable. Such migration has been observed at the top of charge in V-containing compounds [118–121] and can even lead to amorphization. Hence, some caution is required when comparing our topotactic delithiation model with experiments near the fully delithiated phase, $LiVO_3$.

Because the extraction voltage of Li depends strongly on its site energy, understanding which Li is extracted at which voltage provides insight into the local environments to avoid when

designing DRX cathode materials. DRX materials generally exhibit voltage profiles that have a large slope due to the various distributions of TMs around the Li sites. [28] This sloping voltage behavior results in reduced capacity within a fixed voltage window, compared to materials with long-range-ordered cations. [28]

It has been theoretically shown that low-voltage TMs, such as V, exhibit steeper voltage slopes when disordered, owing to a weaker screening of Li–TM interactions by oxygen. [28,122] This weaker screening amplifies the effect of cation disorder on the site energy distribution. [28]

For high-voltage TMs (such as Fe, Co, Ni), we expect the number of NN TMs to play a less significant role in the order of delithiation. Their stronger hybridization with oxygen results in more screening which can moderate the effect of different TM environments on the Li site energy. [28] It has indeed been experimentally shown that substituting some of the V with Fe or Ti [123] in Li_2VO_2F can reduce the slope of the voltage, and result in an overall improvement in the electrochemical cyclability.

In addition to the substitution of V with other TMs, optimization of the amount of Li-excess can help to reduce the voltage slope. As discussed earlier, tetrahedral Li is extracted at high voltages of ~4.1 V. If fewer tetrahedral sites are available or if their site energies are raised, the Li in these sites could be extracted at a lower voltage. One potential strategy may be to substitute some of the Li with more TM. Increasing the TM content will decrease the number of 0-TM channels that become high-voltage tetrahedral Li when the surrounding octahedral Li is removed, and the channel is occupied by Li. Although decreasing the number of 0-TM in this case can improve the voltage profile, it can be detrimental to the kinetics of Li transport because 0-TM channels can provide low-migration-barrier pathways.

3.5 Conclusions

In this work, we investigated the cation short-range order of Li and V in $Li_{2-x}VO_3$. We find that the number of nearest neighbor V in the environment of an octahedral Li plays a crucial role in determining when it is delithiated. We find a strong preference for Li extraction to start from octahedral environments with the most surrounding V. At highly delithiated states, most of the remaining octahedral Li is locked in sites with 2–5 NN V, and Li extraction instead shifts to Li in tetrahedral sites. We find that V oxidizes in a manner that minimizes the number of V^{5+}–V^{5+} bonds.

A design implication arising from this study is that future DRX designs should consider the amount of Li-excess required to balance the 0-TM channels needed for percolation with the potential increase in slope resulting from the higher concentration of high-voltage tetrahedral Li. Additionally, over-stabilized tetrahedral Li at the end of the charge can obstruct migration paths and lead to lower Li^+ diffusivity and energy density. Surprisingly we also find a partially collective migration of Li from octahedral to tetrahedral sites at partial state of charge, reminiscent of spinels. Although we focused on Li_2VO_3 as a model system, our results provide insight for all DRX materials, especially those containing low-voltage TM.

3.6 Supporting information
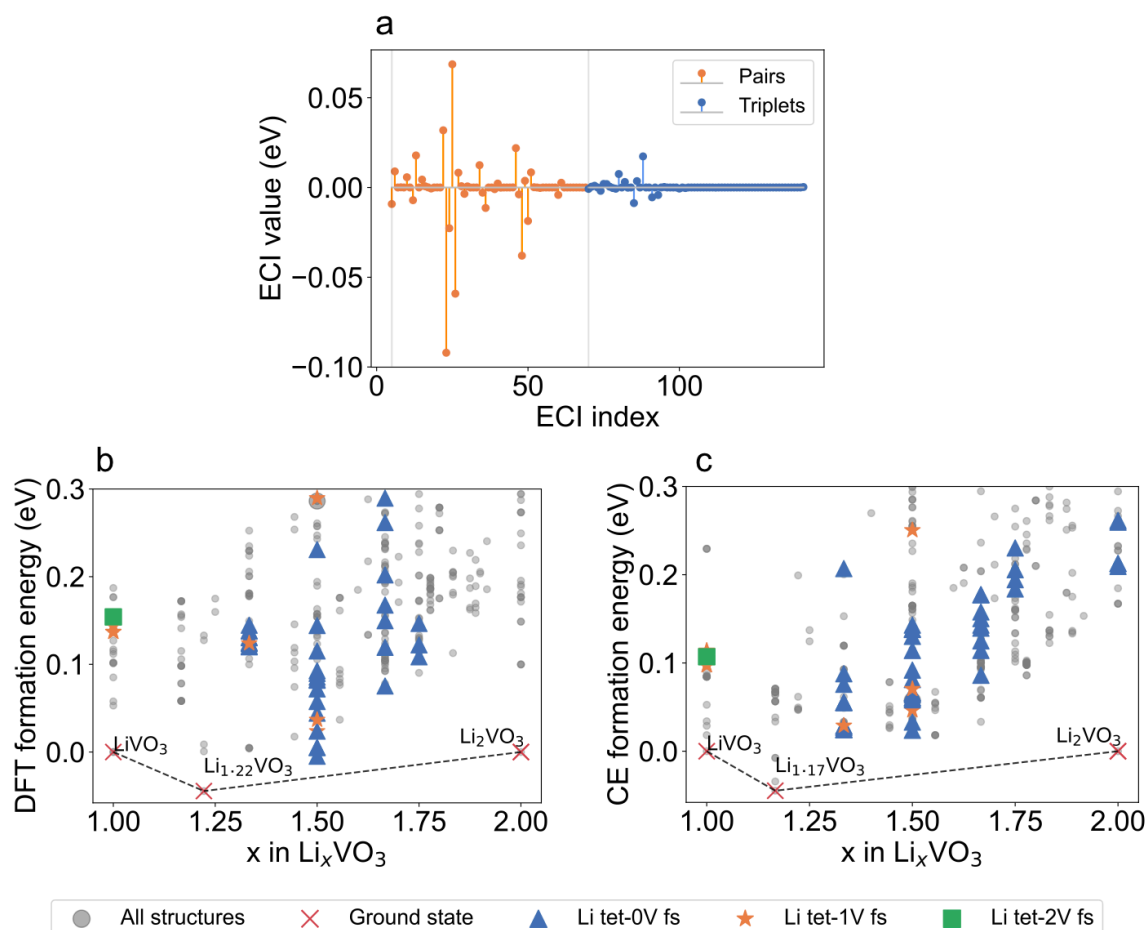
Figure 3-S1 (**a**) ECI value vs. ECI index. Each ECI index corresponds to a specific decoration of Li^+, V^{4+}, and V^{5+} in pair (orange) and triplet (blue) clusters. (**b**) DFT convex hull showing the energies of structures with an energy above the hull below 0.3 eV. The DFT formation energies of all the structures are marked with gray circles. The ground states (Li_2VO_3, $LiVO_3$, and $Li_{1.22}VO_3$) are marked by red crosses. Structures that contain tetrahedral Li with 0, 1, and 2 face-sharing V are marked by blue triangles, orange stars, and green squares, respectively. It is apparent that up to 2 Li tet-V face-sharing is possible based on the DFT data. (**c**) CE convex hull. The ground states (Li_2VO_3, $LiVO_3$, and $Li_{1.17}VO_3$) are marked by red crosses. Although the ground states $LiVO_3$ and Li_2VO_3 are the same in both the DFT and CE convex hulls, there is a discrepancy between the DFT and CE convex hull in predicting the ground state for $Li_{1.22}VO_3$. DFT predicts $Li_{1.22}VO_3$ as the ground state, but it is not predicted in the CE convex hull, where $Li_{1.17}VO_3$ is favored instead. Similar discrepancies in preserving the ground states have been observed in cluster expansions of other high-component systems. [94,103]
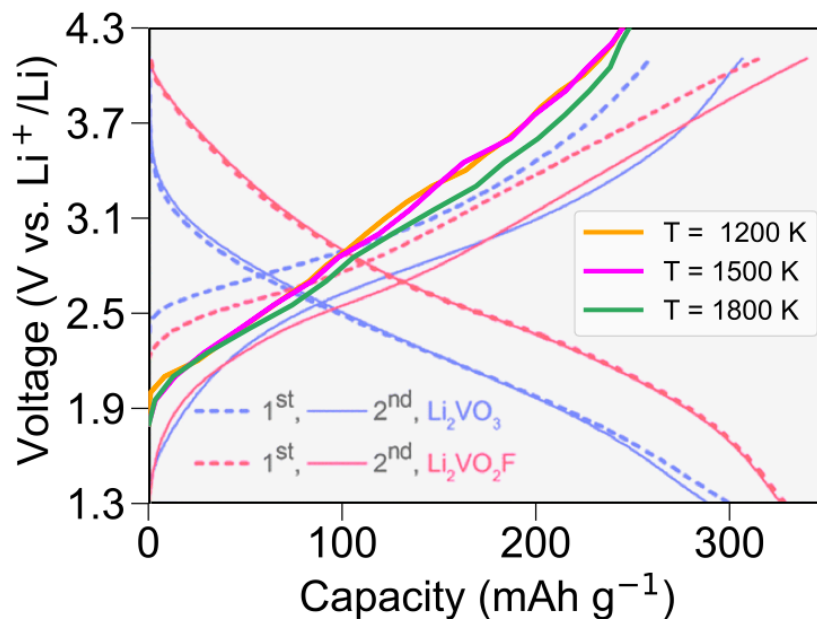
Figure 3-S2 Comparison between the experimental Li_2VO_3 voltage profile obtained by Chen et al. in the dotted blue curve [39] with our SGC MC calculated ones in the Li/V framework sampled at T = 1200 K, 1500 K, and 1800 K. The voltage profile obtained at the simulated temperature of 1800 K shows greater similarity to the experimental voltage profile (dotted blue curves) obtained by Chen et al. [39], specifically at higher delithiated states.
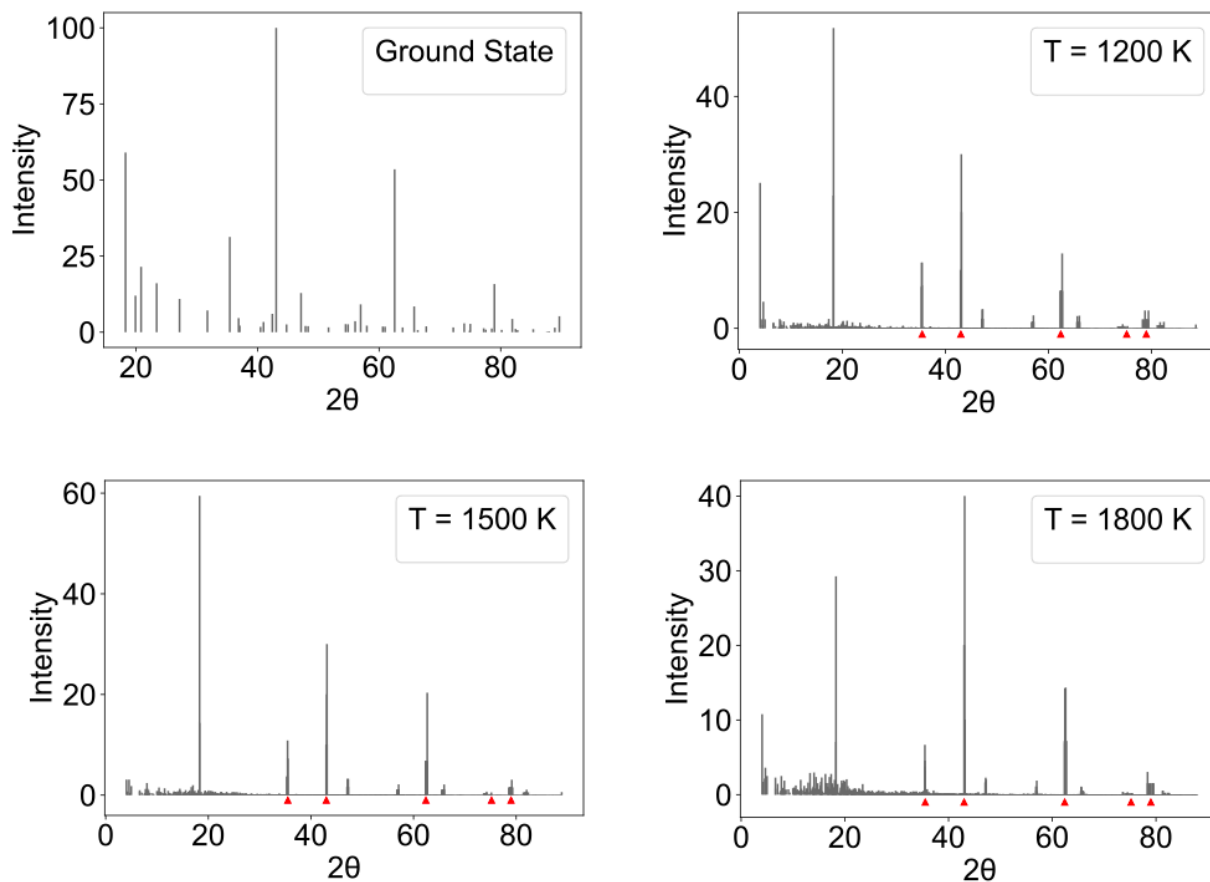
Figure 3-S3 Simulated XRD pattern of fully lithiated Li_2VO_3 in $9\times8\times9$ supercell using pymatgen python package. [111] At the ground state, the XRD pattern corresponds to that of the semi-layered ground state of Li_2VO_3. The simulated XRD patterns for T = 1200, 1500, and 1800 K are averaged over 10 Li/V^{4+} sampled configurations. The main rocksalt peaks (at 38°,43°,63°,76°, and 80°) are marked with red triangles in all cases. While there are peaks at angles below 20 degrees in all three cases, the intensities of the low-angle peaks at 1200 and 1500 K are higher than the main peak at 43°. This, however, does not apply to the Li/V^{4+} configurations sampled at 1800 K.
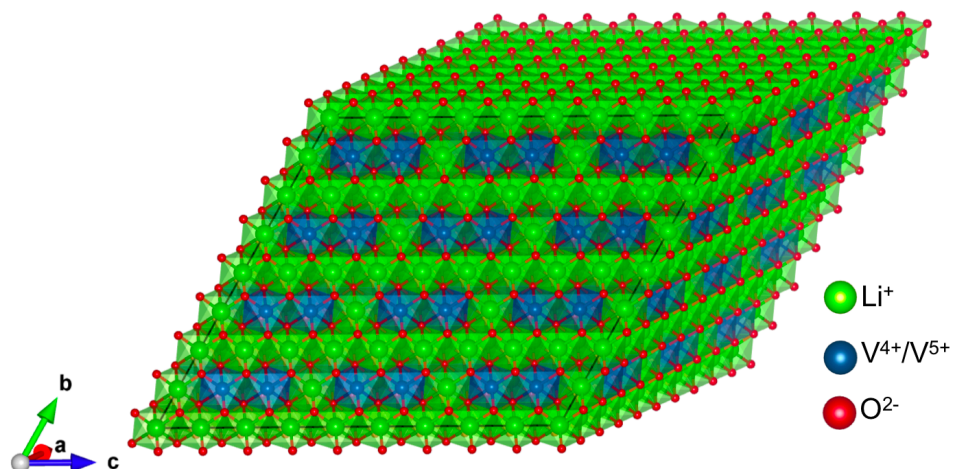
Figure 3-S4 Schematic of fully lithiated Li_2VO_3 at its ground state, which consists of alternating Li^+ and Li^+/V^{4+} layers.
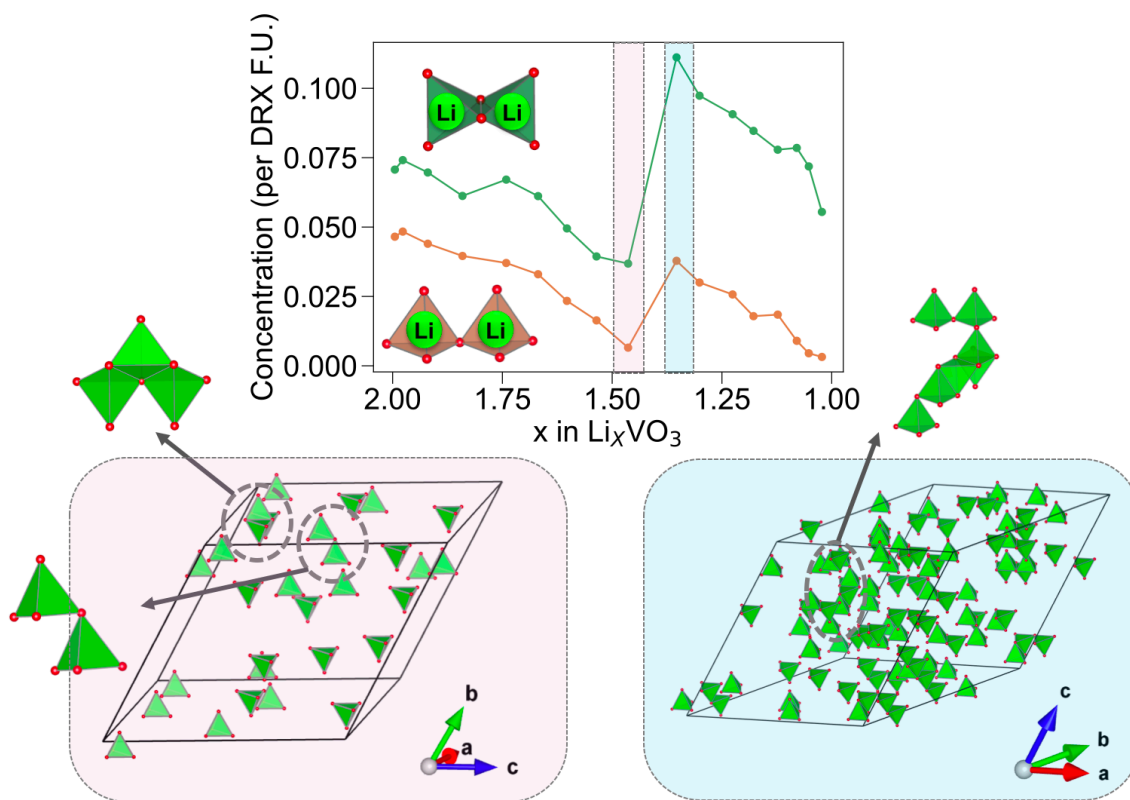
Figure 3-S5 Concentration of edge-sharing (depicted in green) and corner-sharing (represented in orange) Li-tetrahedra as a function of Li content in Li_xVO_3. In our system, the composition ~ $Li_{1.35}VO_3$, highlighted in light blue, exhibits the highest concentration of tetrahedral Li, while the composition ~ $Li_{1.44}VO_3$, highlighted in light pink, shows the lowest concentration of tetrahedral Li. These two cases are further visualized in the bottom figures, which display only the tetrahedral sites. The bottom left figure shows a schematic of Li tetrahedra in ~ $Li_{1.44}VO_3$, where most

42

tetrahedral Li are not edge-sharing or corner-sharing with other tetrahedral Li. By further delithiation of $Li_{1.44}VO_3$, more tetrahedral sites become available for Li to occupy, resulting in clusters of tetrahedral Li in the ~ $Li_{1.35}VO_3$.

Note 1: Challenges of the CE of the high-component system $Li_{2-x}VO_3$, 0 < x < 1

This study is based on a lattice cluster expansion of high-component systems with quaternary disorder (considering $Li^+/V^{4+}/V^{5+}$ and vacancies) on octahedral sites and binary disorder (Li^+ and vacancies) on tetrahedral sites. The fitting of the ECI for this cluster expansion uses an approach applied in other high-component systems. [94,96,103] In this study, we find there are several challenges associated with structural mapping and sampling when addressing the Li–Vac–V–O system in particular.

First, the V^{5+} octahedron experiences significant distortion in part because it is a d_0 element that can strongly distort without an energetic penalty. [124,125] As another example, the presence of vacancies in the system can allow for nearby cations to relax towards the vacancy and reduce electrostatic repulsion from its nearby cations. These distortions make the mapping of the relaxed structure to the lattice-site representation of the cluster expansion extremely challenging as the anion framework becomes highly distorted.

Second, the addition of the interstitial tetrahedral site to the cluster expansion increases the size of the configurational space significantly, and many configurations that could technically exist are practically not achievable. For instance, face-sharing metal-rich clusters have very strong electrostatic repulsion that makes the local configuration unstable. When these configurations are dynamically unstable, they relax away in DFT. As a result, our training data may contain insufficient sampling containing these types of local configurations. We find that this lack of sampling makes the Monte Carlo equilibration more difficult because equilibration may sample structures outside our training set. The dearth of training data with these types of face-sharing configurations may cause our model to represent the energies of structures with face-sharing less accurately and may be a reason for the 2 V– and 3 V–Li tet face-sharing in some of the simulations. Having these face-sharing features as well as the *possibly* larger number of tetrahedral sites compared to the experimental material could be two reasons why the simulated voltage profile is sloppier than the experimental one. Note that metal–Li tet face-sharing features have also been theoretically observed in other studies. [29,96,103]

Chapter 4

Kinetics of Li Transport in V-based Disordered Rocksalt Structures[3]

4.1 Introduction

While the 0-TM percolation theory provides crucial insights into structural characteristics influencing Li^+ transport properties, it only covers some influencing factors, leading to occasional discrepancies in predicting high Li diffusivity.[20,21,37] or the desired rate performance. [38] For instance, Li_2VO_2F exhibits considerable Li-excess but it is reported to have capacity fade due to seemingly slow Li^+ transport kinetics. [38]

A significant aspect not addressed in the current 0-TM percolation theory is the possibility of Li occupying tetrahedral sites in DRX materials [28,30,126], particularly in highly delithiated states where non-face-sharing tetrahedral Li sites can form. Consequently, alternative Li^+ hopping mechanisms, such as hops from a tetrahedral site to another tetrahedral site through an octahedral site or from an octahedral/tetrahedral site to a tetrahedral/octahedral site [30,126], are not considered in the 0-TM percolation analysis of DRX materials.

Another crucial aspect not included in the current percolation theory is the incomplete consideration of site interactions (site energies) and their impact on transport properties. Short-range ordering, which arises from site interactions, and its effect on Li^+ transport properties has been extensively studied. [20,127–129] However, the 0-TM percolation theory for DRX materials does not account for the effect of Li^+ correlated motion, which stems from site interactions and has been demonstrated to significantly hinder transport properties. [25,31,32] The correlations between Li^+ hops are of great importance because they can render Li^+ motion highly inefficient. For instance, even if a network of low-barrier pathways exists, the Li^+ motion may be correlated in such a way that it moves in circles or oscillates back and forth, resulting in no net transport despite locally low migration barriers. [31,32] This type of highly correlated Li jumps have been shown to impede Li^+ transport in spinel Li_xTiS_2 [31] despite its fully connected 0-TM network.

To expand our understanding of the critical factors influencing Li^+ percolation in DRX materials, we develop a kinetic model that accounts for both tetrahedral and octahedral Li occupancy and the site energies of Li occupation that can result in correlated motion. In this paper,

---

we study $Li_{2-x}VO_3$, where $0 \leq x \leq 1$, as a model system that has been investigated as a potential cathode material [39] to examine the kinetics of Li transport. We model this system using a lattice cluster expansion fit to density functional theory (DFT) first-principles calculations that includes quaternary disorder ($Li^+/V^{4+}/V^{5+}$ and vacancies) on octahedral sites and binary disorder (Li^+ and vacancies) on tetrahedral sites. The kinetics of Li^+ transport is modeled on top of this cluster expansion using the kinetic Monte Carlo method, employing the rejection-free (n-fold) algorithm. [130] Our findings reveal that the relative stability of the tetrahedral sites compared to the octahedral sites plays a crucial role in determining how Li^+ diffusivity varies with Li content. Furthermore, we demonstrate that the wide site energy distribution is the primary factor behind the correlated motion in $Li_{2-x}VO_3$. Our analysis recognizes a flat energy landscape as a critical design criterion for improved transport in DRX materials.

4.2 Methods

4.2.1 Cluster expansion model

Extensive configurational sampling can be obtained by using Monte Carlo with the Cluster expansion (CE) method, which is not possible directly using DFT. The CE model used in this work was constructed using the Statistical Mechanics on Lattices (smol) Python package [109] and was extensively described in previous chapter on the cationic short-range ordering of $Li_{2-x}VO_3$, $0 \leq x \leq 1$. [131] We present a brief overview of our model:

The CE for the configurational energy is written in the form shown in equation 4-1:

$$E(\boldsymbol{\sigma}) = \sum_{\beta} V_{\beta} \langle \Phi_{\alpha}(\boldsymbol{\sigma}) \rangle_{\beta}. \qquad (4-1)$$

The occupancy string $\boldsymbol{\sigma}$, in which each element σ_i denotes an occupation variable for site i is used to represent configurations. The summation in equation 4-1 encompasses all symmetrically distinct clusters of basis functions β. We use sinusoidal basis functions as detailed by Van de Walle et al. [101] The coefficients V_{β} are the effective cluster interactions (ECI) weighted by the crystallographic multiplicity of the corresponding clusters. [97,102] The functions Φ_{α} are cluster functions. [101]

Our CE model considers pair interactions up to 7.1 Å and triplet interactions up to 4 Å, based on a cubic cell with a lattice constant $a = 3.0$ Å. An Ewald summation term is also included in the energy model to increase the accuracy and sampling stability of our CE by accounting for long-range electrostatic interactions. [24,104,129,132]

The degrees of freedom in the lattice model for $Li_{2-x}VO_3$, as illustrated in Figure 4-1, include {Li^+, V^{4+}, V^{5+}, vacancy} on the octahedral sublattice [39] and {Li^+, vacancy} on the tetrahedral sublattice. [28,30] The anion sites are fully occupied by O^{2-} and hence do not need to be represented in the CE. [39] Sparse group lasso regularization was used to fit the ECIs of this high-component system using DFT energies of 450 symmetrically distinct configurations. In 10-fold cross-validation the resulting fit reproduced DFT with a root-mean-squared error (RMSE) of 13.1 meV per site and in-sample RMSE of 12.4 meV per site.
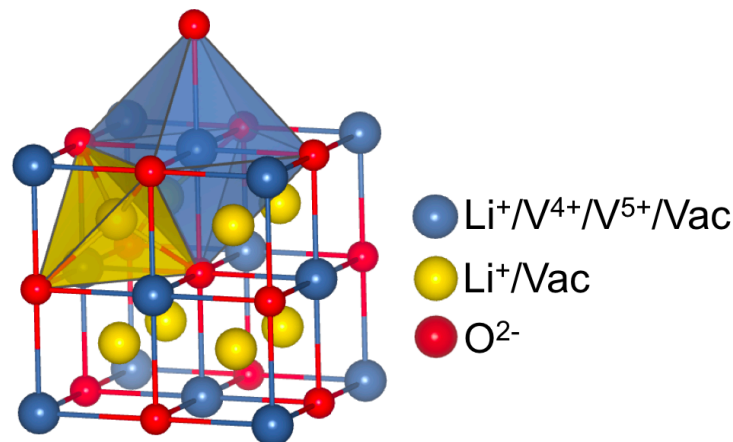
Figure 4-1 Rocksalt lattice of $Li_{2-x}VO_3$, $0 \leq x \leq 1$. The blue spheres correspond to the face-centered cubic (FCC) lattice of octahedral sites, which can be occupied by Li^+, V^{4+}, V^{5+}, or a vacancy. The yellow spheres correspond to tetrahedral sites, which can be occupied by Li^+ or a vacancy. The red spheres form the anion lattice, which is fully occupied by oxygen and does not need to be included in the degrees of freedom of the CE.

4.2.2 First principles DFT calculations

The structure–energy dataset used to fit the CE was obtained using DFT [133,134] implemented in the Vienna ab-initio simulation package (VASP) [135,136] with the projector-augmented wave (PAW) method. [137,138] The PBE exchange-correlation functional [139] with rotationally averaged Hubbard (U = 3.1 eV) correction was used based on a previously reported calibration to oxide formation energies (3.1 eV for V). [24,100] A plane-wave cutoff of 520 eV, reciprocal-space discretization of 25 K-points per Å, electronic convergence of 10^{-5} eV and 0.01 eV Å^{-1} for forces were used in all of our calculations.

The Nudged Elastic Band (NEB) calculations are conducted using five images along the diffusion paths for single-vacancy and divacancy TSH mechanisms at compositions of $LiVO_3$, $Li_{1.5}VO_3$, and Li_2VO_3 in supercells of 3×3×3 or 3×4×3, containing 27 or 36 oxygen atoms. Configurations for the NEB calculations are created by Monte Carlo at temperatures of 300 K and 5000 K to generate for various local environments for Li^+ migration. In the NEB calculations, it is ensured that the distance between the migrating Li^+ and its periodic image exceeds 8 Å in order to prevent any self-interactions. All the NEB calculations are performed using the GGA method without the Hubbard-U correction to prevent potential convergence issues arising from electron localization at different atomic centers along the migration path. [68,69]

4.2.3 Transport properties

In solid crystalline intercalation compounds, such as DRX materials, the diffusion of Li^+ typically occurs through a substitutional diffusion mechanism, in which Li^+ migrates to adjacent vacant sites. [25,31,35,36,54,140] The presence of diverse local environments in DRX materials results in a dependency of the Li^+ migration energy barrier on its local surroundings. Kinetic Monte Carlo (KMC) simulations can combine a cluster expansion to incorporate the Li^+-Li^+ and Li^+-host

energetics with a local cluster expansion to model the variations in migration energy. [25] We show below a simplified model to capture the dependence of migration energy on environment.

To derive the diffusion coefficients from the Li trajectories we employ the Green–Kubo approach, derived from the fluctuation theorem at equilibrium. [141–143] The chemical diffusion coefficient, $D_{Chemical}$, represents the relationship between the flux of migrating species, and their concentration gradients. [142] $D_{Chemical}$ can be calculated by multiplying the thermodynamic factor, Θ, with the jump diffusion coefficient, D_{Jump} [142]:

$$D_{Chemical} = \Theta D_{Jump}. \quad (4-2)$$

The thermodynamic factor Θ, given by equation 4-3, measures the deviation of the solution thermodynamics from the non-interacting ideal solution. When Li^+–Li^+ interactions are negligible (in the dilute-limit case), the thermodynamic factor is 1.

$$\Theta = \frac{\partial \left(\frac{\mu}{k_B T}\right)}{\partial \ln(x)} . \quad (4-3)$$

In equation 4-3, μ represents the Li chemical potential, k_B denotes Boltzmann's constant, T signifies the absolute temperature, and x corresponds to the Li concentration. In this study, the thermodynamic factor is computed by scanning the Li chemical potential in steps of 0.05 eV using semi-grand canonical Monte Carlo (SGC MC) simulations at T = 300 K. The thermodynamic and transport analysis are conducted in a 9×8×9 supercell (comprising a 648-oxygen supercell) of $Li_{2-x}VO_3$ with Li/V metal configurations obtained by equilibrating at 1800 K. The selection of 1800 K was established in previous work and is based on the similarity of the simulated and experimental voltage profiles and XRD patterns at this temperature. [131]

The jump diffusion coefficient D_{Jump} in equation 4-2 measures the fluctuation of the center of mass of all diffusing Li-ions and can be determined as [144,145]:

$$D_{Jump} = \frac{1}{2dt}\frac{1}{N}\langle \left[\sum_{i=1}^{N} \Delta\vec{R_i}(t)\right]^2 \rangle . (4-4)$$

In equation 4-4, d represents the dimension of the interstitial lattice in which diffusion occurs (for DRX $Li_{2-x}VO_3$, d is 3), t denotes time, N refers to the number of diffusing Li ions, and $\Delta\vec{R_i}(t)$ is the displacement vector of the ith ion after time t. The angular brackets signify the ensemble average at equilibrium after time t.

Compared to D_{Jump}, the tracer diffusion coefficient, D_{Tracer}, is based on the fluctuation of the position of individual Li-ions and can be determined as follows:

$$D_{Tracer} = \frac{1}{2dt}\frac{1}{N}\sum_{i=1}^{N} \langle \left[\Delta\vec{R_i}(t)\right]^2 \rangle . (4-5)$$

The tracer diffusion itself includes self-correlation caused by the diffusion topology and the energy landscape. The deviation of D_{Tracer} from the random-walk scenario is measured by the correlation factor : [31]

$$f = \frac{\langle \vec{R}(t)^2 \rangle}{na^2}. \quad (4-6)$$

In equation 4-6, $\langle \vec{R}(t)^2 \rangle$ represents the mean squared displacement of a Li ion after a time t. The variable n refers to the number of jumps Li$^+$ has executed during the simulation period, and a is the hop distance.

The rate constants Γ_{ij} for Li$^+$ hopping from site i to site j can be determined from transition state theory [146]:

$$\Gamma_{ij} = \nu^* exp \left(-\frac{\Delta E_{ij}}{K_B T} \right). \quad (4-7)$$

where ν^* is the vibrational prefactor, estimated to be 10^{13}. [25] The migration activation barrier for Li$^+$ hopping from site i to site j is represented by ΔE_{ij}. As ΔE_{ij} depends on the local environment it is crucial to parameterize its value in accordance with the variations in these local environments. [25,35,36]

When tetrahedral Li sites can be occupied, more elementary diffusion steps are possible than when Li only occupies octahedral sites. [30] To simplify our kinetic model, we allow Li$^+$ to hop between octahedral sites and their nearest-neighbor (face-sharing) tetrahedral sites and vice versa, as most of the diffusion mechanisms in DRX materials [30] can be broken down into these two fundamental hops. Hence, we assign a value of 1.82 Å to parameter a in equation 4-6, as it corresponds to the nearest-neighbor distance between octahedral and tetrahedral sites. Li$^+$ migration in DRX compounds can also potentially occur directly from a tetrahedral site to an edge-sharing tetrahedral site. [30] However, we have excluded this mechanism for two reasons. Firstly, the barrier for Li$^+$ migration through edge-sharing tetrahedral-tetrahedral hops has been found to reach up to 900 meV. [30] Secondly, including this mechanism will not significantly impact our simulation's final results since most low-barrier Li$^+$ migration mechanisms predominantly occur through the triangular face rather than the edge. [30]

The energy of a Li$^+$ ion in a tetrahedral site depends strongly on the occupancy of its four face-sharing octahedral sites. In our kinetic model, we account for all Li$^+$ transitions from octahedral to tetrahedral sites that do not face-share with any Vanadium-occupied sites, or face-share with a single Vanadium-occupied site and two vacant sites. These transitions are abbreviated as 0-TM and 1-TM$_{\text{di-vac}}$ in line with notation in earlier papers on diffusion in rocksalt-like materials. [14,15] Due to the high migration energy observed in the 1-TM$_{\text{single-vac}}$ hop (Figure 4-S1), we omitted it from our KMC simulations. Hops into tetrahedral sites with two face-sharing Vanadium have even higher energy and can safely be excluded from our simulation.[14] Migration barriers for face-sharing hops are obtained from NEB calculations of the tetrahedral site hop (TSH) mechanism when the tetrahedral site represents a local minimum in the minimum energy pathway. To integrate migration barriers with the site energy landscape of the cluster expansion, we use the kinetically resolved activation (KRA) barrier in KMC simulations. [25] The KRA is calculated by subtracting the average energy of the hop's endpoints from the energy of the activated state. [25] In our KMC simulations, we employed a single KRA value for all hops, and we provide the rationale for this decision in Figure 4-2.

KMC simulations are conducted at 300 K using the rejection-free algorithm. [147,148] The initial state of each KMC simulation done in a 9×8×9 supercell for 12 compositions of Li$_{2-x}$VO$_3$. At each KMC step (i.e., a Li$^+$ hop to a nearby vacancy), we randomly select a migrating Li$^+$ and choose a jump based on a probability proportional to its rate. [130] We perform 50,000 KMC steps starting from each initial configuration and average the Li$^+$ trajectories after 20,000 steps to ensure the system is fully equilibrated.

4.3 Results
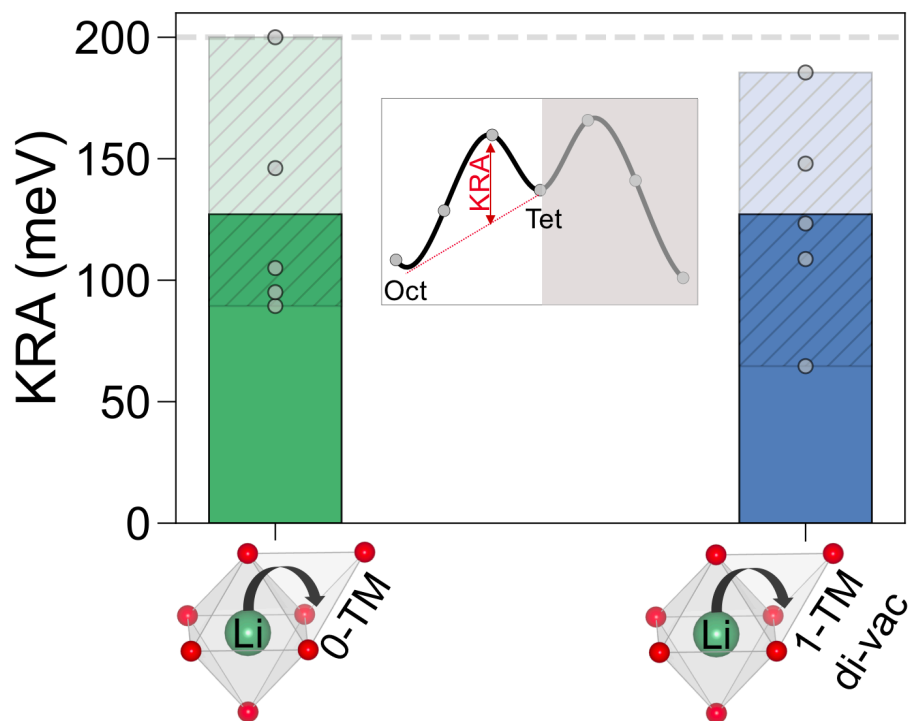
Figure 4-2 The KRA barriers for Li$^+$ hops from an octahedral site to 0-TM (green) and 1-TM$_{\text{di-vac}}$ tetrahedral sites (blue) are displayed. The solid bars represent the average value of the KRAs, and the hatched bars illustrate the range between the maximum and minimum values of the KRAs for each hop category. These KRAs were determined from 10 NEB calculations of TSH mechanisms on different Li/V configurations. In these calculations, the intermediate tetrahedral site acts as a local minimum for the migrating Li$^+$ (as shown in the inset plot). The circle markers indicate the data points for each hop category. The gray dotted line represents the upper limit of the KRA values, set at 200 meV, which is used as input for all octahedral-to-tetrahedral (or vice versa) hops in the KMC simulation.

Figure 4-2 displays the KRA values for Li$^+$ hops from octahedral sites to 0-TM single-vacancy, divacancy, and triple-vacancy tetrahedral sites as well as to 1-TM$_{\text{di-vac}}$ tetrahedral sites. The KRA values were derived from the TSH migration mechanisms, where the intermediate tetrahedral site serves as a local minimum, as shown in the inset plot. The minimum energy pathways for all 10 NEB calculations used to determine the KRA values are presented in Figure 4-S2.

The KRA values for both 0-TM and 1-TM$_{\text{di-vac}}$ hops range from ~ 70 to 200 meV, with their mean values centered at ~130 meV. One possible explanation for the migration barrier of the 1-TM$_{\text{di-vac}}$ hop being comparable to that of the 0-TM hop is the relaxation of V away from the center of the polyhedron. [126] This effect, especially pronounced for ions with d^0 electron configuration like V^{5+} [125,149], weakens the electrostatic interaction between Li$^+$ in the tetrahedral site and the face-sharing V in its neighboring site, potentially reducing migration barriers for the 1-TM$_{\text{di-vac}}$ environments. Moreover, due to the ease of V relaxation [126], tetrahedral Li–V face-sharing features have been observed in modeling of both Li$_{2-x}$VO$_3$ [131] and Li$_{3+x}$V$_2$O$_5$ DRX materials. [126] As there is no significant difference between 0-TM and 1-TM$_{\text{di-vac}}$ hops, we used a single KRA value for the KMC simulation to further simplify the kinetic model. The energy

difference between the initial and final states of the hop, captured by the CE, accounts for the difference between the migration barriers for 0-TM and 1-TM$_{di-vac}$ hops. This method of parameterizing the energy barrier has been successfully employed in other transport studies based on KMC simulations. [32] The selected KRA value for any octahedral-to-tetrahedral (or vice versa) hop is set at 200 meV, equal to the upper limit of the KRA values presented in Figure 4-2. Utilizing a single KRA value can influence the absolute magnitude of Li$^+$ diffusivity, which we further elaborate on in the discussion section.
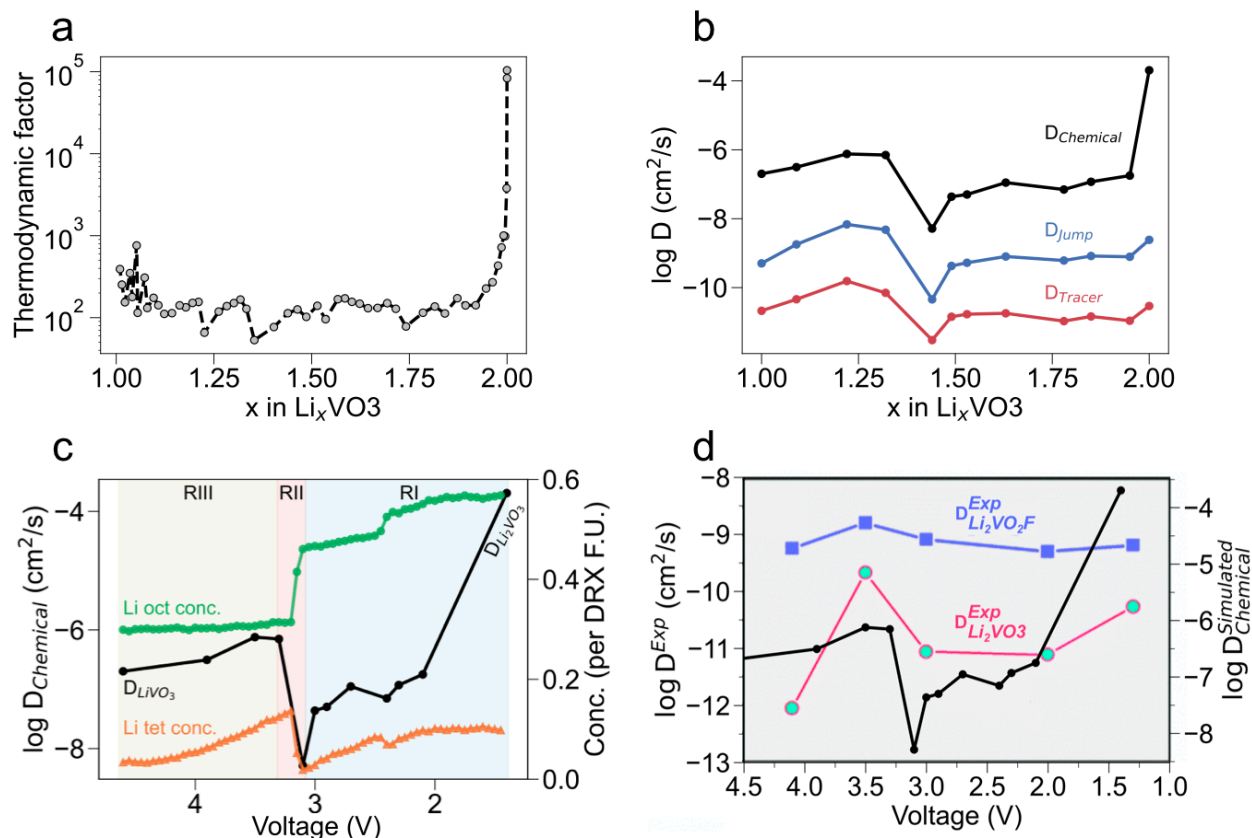
Figure 4-3 (a) The calculated thermodynamic factor, Θ, is shown as a function of Li content, x, in Li$_X$VO$_3$, at 300 K. The thermodynamic factor diverges at x$_{Li}$ = 2, corresponding to the fully lithiated composition. **(b)** The calculated D_{Tracer} (red), D_{Jump} (blue), and $D_{Chemical}$ (black) are displayed as a function of the Li content in Li$_x$VO$_3$ at 300 K, in units of cm^2/s. **(c)** The computed concentrations of octahedral Li (green) [131], tetrahedral Li (orange) [131], and $D_{Chemical}$ as a function of voltage [131]. The regions RI, RII, and RIII correspond to the voltage ranges of (1.4 to 3.1), (3.1 to 3.3), and (3.3 to 4.6), respectively. **(d)** Experimental diffusivity of Li$_2$VO$_3$ (red curve) and Li$_2$VO$_2$F (blue curve) obtained by Chen et al. [39] and simulated diffusivity of Li$_2$VO$_3$ (black curve) calculated by KMC simulations.

Figure 4-3a displays the thermodynamic factor calculated at 300 K as a function of Li content in Li$_x$VO$_3$. The value of the thermodynamic factor is on the order of 10^2 but diverges to much larger values for the fully lithiated composition as the thermodynamic factor is proportional to the inverse of the vacancy concentration. [25,31,35] Such behavior of the thermodynamic factor has been previously observed in certain layered and spinel systems. [25,31,35]

Figure 4-3b displays $D_{Chemical}$ (black), D_{Jump} (blue), and D_{Tracer} (red) calculated using equations 4-2, 4-4, and 4-5 as a function of Li content in Li_xVO_3. The magnitude of D_{Tracer} ranges from 10^{-11} to 10^{-10} cm^2/s, whereas that of D_{Jump} spans from 10^{-10} to 10^{-8} cm^2/s. In contrast, the magnitude of $D_{Chemical}$ mainly falls between 10^{-8} and 10^{-6} cm^2/s, except at the fully lithiated state, where it is on the order of 10^{-4} cm^2/s. Consistent with other kinetic studies on certain layered and spinel systems, D_{Tracer} is the lowest among the diffusion coefficients. [25,31,35] This finding occurs because D_{Jump} and $D_{Chemical}$ rely on the collective displacements of Li$^+$ rather than the average displacements of individual ions, which is the case for D_{Tracer}.

A noticeable jump in all the simulated diffusion coefficients is observed, with the lowest point occurring at the $Li_{1.44}VO_3$ composition and the highest point at $Li_{1.22}VO_3$. To investigate the reason for this jump, we present the concentrations of octahedral Li (green) [131] and tetrahedral Li (orange) [131] and the corresponding $D_{Chemical}$ as a function of voltage [131] in Figure 4-3c. In order to directly compare the simulated diffusivity with the experimental diffusivity of Li_2VO_3 (red curve in Figure 4-3d) obtained by Chen et al. [39], we analyze these quantities as a function of voltage instead of Li concentration in both Figure 4-3c and 4-3d.

Figure 4-3c highlights three regions. Region I (RI), which covers the voltage range of (1.4 to 3.1), corresponds to the delithiation of Li_2VO_3 down to $Li_{1.49}VO_3$ (as shown in Figure 4-3b). In this region, the magnitude of $D_{Chemical}$ initially decreases from Li_2VO_3 to $Li_{1.95}VO_3$ and then remains approximately constant at ~10^{-7} cm^2/s. The experimental diffusivity of this material exhibits a similar change as a function of voltage within this voltage range, as shown in Figure 4-3d. [39] Additionally, we observe that both the tetrahedral and octahedral Li concentrations decrease in this voltage range.

Region II (RII), covering the voltage range of (3.1 to 3.3), corresponds to the delithiation of $Li_{1.49}VO_3$ to $Li_{1.32}VO_3$. As depicted in Figure 4-3c, we observe an increase in diffusivity along with the concentration of tetrahedral Li while the concentration of octahedral Li oct decreases. The experimental diffusivity of this material exhibits a similar jump within the similar voltage window. [39] The simultaneous decrease/increase in the octahedral/tetrahedral Li concentration suggests that some of the octahedral Li migrates to the tetrahedral sites. [131] This migration has also been observed for the fluorinated iso-structure of this material at this composition, $Li_{1.44}VO_2F$. [150] Such collective migration phenomena are known to occur in ordered spinel compounds [103]; however, they have not yet been well characterized for cation-disordered materials. This correlation between the magnitude of diffusivity as a function of Li content and the concentrations of Li in tetrahedral and octahedral sites underscores the importance of considering both tetrahedral and octahedral sites in the transport analysis of DRX materials.

Region III (RIII) spans the voltage range of (3.3 to 4.6) and corresponds to the delithiation of $Li_{1.32}VO_3$ to $LiVO_3$. In this region, we observe a decrease in diffusivity, which aligns with the behavior of the experimental diffusivity of Li_xVO_3 as a function of voltage. [39] In RIII, the Li concentration in octahedral sites remains constant while the tetrahedral Li concentration decreases. This suggests that Li extraction from $Li_{1.44}VO_3$ primarily occurs from high-voltage tetrahedral sites [131], contributing to the lower diffusivity in this range. Notably, the experimental diffusivity of this material decreases more rapidly [39] than the simulated diffusivity in RIII. In the discussion section, we leverage the insights obtained from studying oxide compounds to compare and understand the experimental diffusivity of Li_2VO_2F.
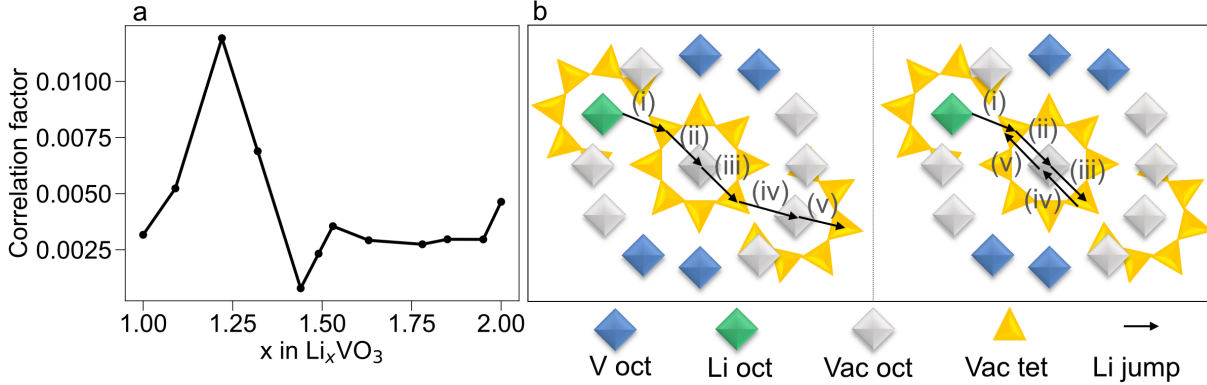
Figure 4-4 (a) The calculated correlation factor as a function of Li content, x, in Li_xVO_3. **(b)** A two-dimensional schematic of a Li-ion migrating in a rocksalt structure is shown. The left panel represents the case where the correlated motion of Li-ions is not considered, whereas the right panel represents the case where the correlated motion is included. In a rocksalt structure, each octahedral site (shown with diamonds) edge-shares with 12 other octahedral sites and face-shares with 8 tetrahedral sites (shown with triangles). The V-ions are represented by blue diamonds, while the green diamonds, gray diamonds, and yellow triangles represent octahedral Li sites, octahedral vacant sites, and tetrahedral vacant sites, respectively. The black arrows denote the Li^+ jumps, which are labeled sequentially from (i) to (v).

Figure 4-4a displays the calculated correlation factor plotted against the Li content in Li_xVO_3. The correlation factor ranges between 10^{-3} and 10^{-2} with the highest value at the composition $Li_{1.22}VO_3$ and the lowest value at $Li_{1.44}VO_3$. The observed correlation factor in Li_xVO_3 is consistent with the predicted range of 10^{-3} to 10^{-2} in the DRX transport model developed by Anand et al. [151] For comparison, the correlation factor for diffusion in layered $LiCoO_2$ [25] and the spinels $Li_{1+x}Ti_2O_4$ [35] and Li_xTiS_2 [31] is on the order of 10^{-1} across varying Li content, while the predicted correlation factor for Mg_xTiS_2 [32] can be as low as 10^{-5}. Unlike Li_xCoO_2 [25] and the spinels Mg_xTiS_2 [32], Na_xTiS_2 [32], Li_xTiS_2 [32], which show an increase in the correlation factor with delithiation (i.e., increasing vacancy concentration), the correlation factor of DRX Li_xVO_3 does not show a consistent trend with increasing vacancy concentration. This finding indicates that factors other than the vacancy concentration play a role in determining Li^+ correlated motion in this DRX system.

To enhance our understanding of the concept of Li^+ correlated motion, Figure 4-4b depicts how Li-ions move in a local environment based on the results of the KMC simulation. The left panel of Figure 4-4b shows Li^+ migration from one octahedral site to another without significant self-correlation. However, in systems in which there is significant correlation Li^+ performs oscillatory movements between specific sites, slowing its progress to the following site, as depicted in the right panel of Figure 4-4b. This type of correlated motion is commonly observed and has been extensively studied in ionic conductors and electrolytes [80,152,153] and is known as *self-correlated* motion, reflected in the D_{Tracer} value. [154]

It has been demonstrated mathematically that the connectivity of the sites impacts the correlated motion. [154] The connectivity of the sites can be disrupted if a high-barrier channel obstructs a network. In such cases, migrating Li^+ cannot move past the block or percolate through the structure. [14,15] Both Li-excess and cation short-range ordering influence the formation of a percolating network in DRX. [20,127–129] As previously mentioned, Li-excess results in the formation of Li_4 clusters, whereas cation short-range ordering determines the extent of Li_4 tetrahedral

connectivity in DRX materials. [20,127–129] Another factor responsible for the correlated motion is the ionic interactions that introduce non-uniformity in the energy landscape. [154] When an ion jumps uphill it is now more likely to jump backward to the site it came from. As stated by Anand et al. [151], when the standard deviation of the site-energy distribution exceeds k_BT, the fraction of Li sites involved in percolation can be significantly lower [151] than what the 0-TM percolation theory predicts. [14,15] It is worth noting that the model developed by Anand et al. represents Li–TM and Li–Li interactions through variations in site energies, considering all sites as Li/vacancy sites. [151]
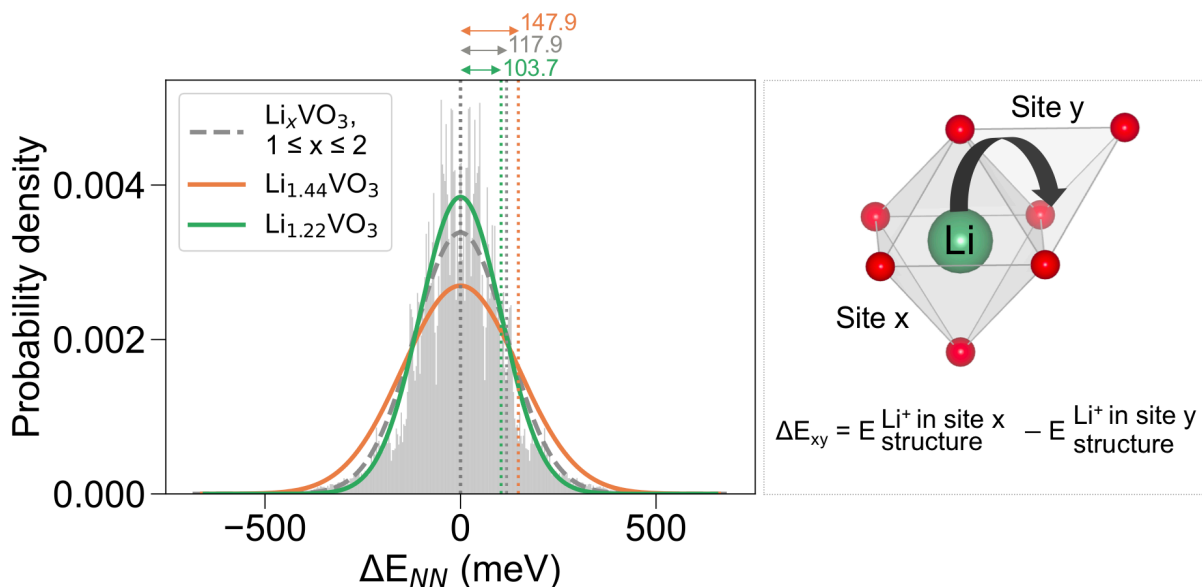
Figure 4-5 The gray histogram in the left panel illustrates the energy difference between nearest-neighbor sites (ΔE_{NN}) along the hops in the kinetic Monte Carlo simulation in the composition range of Li_xVO_3 ($1 \leq x \leq 2$). The dotted gray curve represents the fitted normal distribution to this histogram. The orange and green curves correspond to the normal distribution curves fitted to the energy differences between nearest-neighbor sites along the Li^+ hops restricted to compositions $Li_{1.44}VO_3$ and $Li_{1.22}VO_3$, respectively. The values 103.7, 117.9, and 147.9 at the top of the plot indicate the standard deviations of ΔE_{NN} for compositions $Li_{1.22}VO_3$, Li_xVO_3 ($1 \leq x \leq 2$), and $Li_{1.44}VO_3$, respectively. The schematic on the right further clarifies the meaning of ΔE_{NN} along the hop.

Figure 4-5 presents the energy difference between the nearest-neighbor sites along the Li^+ hop (ΔE_{NN}). The gray histogram in the background of Figure 4-5 illustrates the distribution of ΔE_{NN} within the composition range of Li_xVO_3 ($1 \leq x \leq 2$). The dotted gray curve represents the normal distribution fitted to the ΔE_{NN} histogram and shows a standard deviation of approximately 118 meV. When fitted to only hops that occur at composition $Li_{1.22}VO_3$ (green) the distribution narrows to 104 meV, while at composition $Li_{1.44}VO_3$ (orange) the distribution widens to 148 meV. Comparison of these hop distributions with the correlation factor in Figure 4-4a suggests that flatter energy landscapes, characterized by a narrower hop energy distribution, increase the correlation factor and thereby the effective diffusivity, as suggested by Anand. [151]
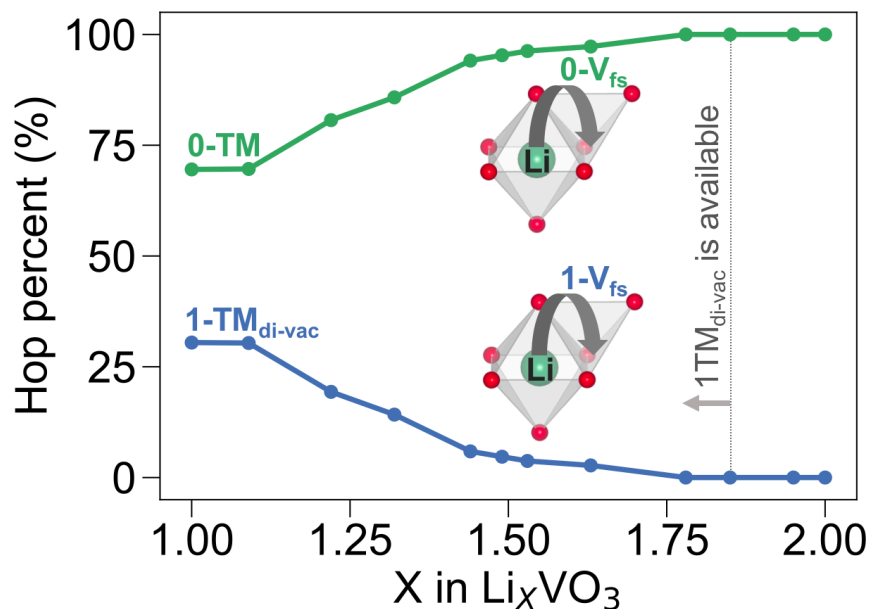
Figure 4-6 The percentage of Li$^+$ hops from octahedral to tetrahedral sites that face-sharing with no vanadium (0-TM) (represented in green) or with one Vanadium (depicted in blue) as function of Li composition.

The initial premise of the 0-TM percolation theory underscored the significance of incorporating 0-TM in transport analysis. [14,15] Our KMC model provides the opportunity to investigate the environment through which Li ions hop. We present in Figure 4-6 the percentage of hops from octahedral to 0-TM and 1-TM tetrahedral sites. Our results reveal a consistent predominance of Li$^+$ hops from octahedral to 0-TM tetrahedral sites over those to 1-TM$_{\text{di-vac}}$ tetrahedral sites, consistent with the basic idea of 0-TM percolation theory. [14,15] The lack of availability of 1-TM$_{\text{di-vac}}$ at high Li content is not unexpected, considering prior work on LiCoO$_2$ in which it was observed that the divacancy mechanism only becomes accessible for $x_{\text{Li}} < 0.8$. [25]

Our analysis proposes that as the number of vacancies increases towards $x_{\text{Li}} = 1$, hops to a tetrahedral site with face-sharing vanadium (1-TM$_{\text{di-vac}}$) occur, but remain minority pathways. Although our analysis has been centered on octahedral-to-tetrahedral hops rather than octahedral–tetrahedral–octahedral hops, our findings confirm that as a general rule 0-TM channels do provide the pathway for Li percolation though extensions to include the 1-TM$_{\text{di-vac}}$ mechanism could be relevant near the top of charge.

4.4 Discussion

In this paper we investigated the macroscopic diffusion mechanism in the disordered rocksalt Li$_x$VO$_3$ by combining a cluster expansion for the energy landscape and limited migration hops from octahedral to tetrahedral sites and vice versa. The incorporation of the tetrahedral site as a distinct Lithium site enables us to better understand the role it plays in delithiation and its kinetics. Specifically, Figure 4-3c demonstrates the significant impact of the relative stability between Li in tetrahedral and octahedral sites on the variation of Li$^+$ diffusivity with Li content.

In contrast to certain layered and spinel systems [25,31,32,35], the diffusion coefficient (Figure 4-3b) and correlation factor (Figure 4-4a) of Li$_x$VO$_3$ do not improve with an increasing vacancy

concentration. Moreover, empirical evidence shows that the diffusivity of DRX materials [20,21,37,39] remains relatively stable even when the Li concentration varies. This indicates the presence of other influential factors that overshadow the effects of vacancy concentrations. The distribution of the Li site energy in DRX structures is greatly affected by the variation in the surrounding TM around the Li sites, which is determined by the strength of the Li–TM interaction. [28] For Li^+ to percolate efficiently, there must be a network of low-barrier local environments where all the nearest-neighbor sites are in a similar energy range. [151,153] Notably, the importance of the energy landscape in the kinetics of DRX materials is highlighted by Figure 4-5 and the recent publication by Anand et al. [151] For layered structures such as $LiCoO_2$, where all the Li sites have the same number of TM around them, overcoming the energy difference between the initial and final states of the hop is not a significant issue, as the only difference is in the vacancy concentration. [25] However, Figure 4-5 reveals that for DRX Li_xVO_3, even the composition with highest diffusivity ($Li_{1.22}VO_3$) can exhibit a difference in nearest-neighbor site energies exceeding 400 meV. This substantial variation in nearest-neighbor site energy within Li_xVO_3 can help to explain the low correlation factor in Li_xVO_3 comparing to some layered and spinel systems. [25,31,32]

Our results reveal that the abrupt enhancement in both theoretical and experimental diffusivity shown in Figure 4-3d, [39] between the compositions of $Li_{1.22}VO_3$ (V = 3.5 V) and $Li_{1.44}VO_3$ (V = 3.1 V), can be attributed to the somewhat sudden transition of Li^+ from octahedral to tetrahedral sites, as demonstrated in Figure 4-3c. This same transition from octahedral to tetrahedral Li^+ migration has been computationally observed in $Li_{1.44}VO_2F$, a fluorinated isostructural counterpart of Li_2VO_3.[150] Interestingly, the experimental diffusivity of Li_2VO_2F (shown in Figure 4-3d) [39] exhibits a jump at 3.5 V (~ $Li_{1.44}$) [39], similar to the theoretical and experimental findings observed in the oxide compound, though with a less pronounced peak. [39] Collective migration phenomena such as these are recognized in ordered spinel compounds [103], yet their occurrence within DRX compounds is somewhat surprising. A potential explanation for this collective motion could be that following the removal of 28% of Li (from Li_2VO_3 to $Li_{1.44}VO_3$), the energy for Li to occupy tetrahedral and octahedral sites begins to converge due to the creation of vacancies on octahedral sites (which lower the energy of tetrahedral occupancy). Support for this explanation is provided in Figure 4-5, where the distribution of hop energies in the $Li_{1.22}VO_3$ composition exhibits the smallest standard deviation, indicating in a dense network of available sites with comparable energies. Consequently, the correlation factor and the diffusion coefficient increase from $Li_{1.44}VO_3$, peaking at the composition $Li_{1.22}VO_3$.

An increase in the stability of Li^+ in tetrahedral sites can enhance the diffusivity by providing more available sites for Li^+; however, when the site energy for Li in tetrahedral sites becomes too low, their occupation by Li^+ can also impede migration through these sites, leading to lower experimental [39] and theoretical diffusivities as observed in highly delithiated states. Notably, the experimental diffusivity of Li_xVO_3 [39] declines more rapidly near the end of the charge than the theoretical diffusivity.

The experimental diffusivity of Li_2VO_3 has been reported to fall in the range of 10^{-12} to 10^{-10} cm^2/s (Figure 4-3d) [39], which is four orders of magnitude lower than our simulated chemical diffusivity. Other kinetic studies have also observed this disparity between the experimental and simulated diffusivity. [32,80] This discrepancy may have multiple origins. One of the primary problems when comparing experimental and simulated diffusivities is the challenge in estimating the active electrode and electrolyte surface area. [31] In the past, everything from the active electrode area to the total particle surface area has been used leading to very different diffusion constants.

Assumptions in the theory models, such as the choice of single KRA and prefactor values, the diffusion mechanisms considered, may also contribute to the deviation between the experimental and theoretical diffusivity, though it seems unlikely that these would lead to variations that are more than an order of magnitude. The lack of any consideration of electronic transport limitations, either at the particle or electrode level may further complicate comparison between theory and experiment. Consequently, kinetic studies, including ours, have primarily concentrated on how the diffusivity varies with Li content rather than focusing on its absolute magnitude. [32]

The probability of finding tetrahedral sites in $Li_{2-x}VO_3$ face-sharing with 1-V, is twice as high as the probability of tetrahedral sites without face-sharing, as illustrated in Figure 4-S3. Nevertheless, Figure 4-6 demonstrates that nearly all octahedral-to-tetrahedral hops within the composition range of $Li_{1.63}VO_3$ to Li_2VO_3 are into tetrahedral sites without V face-sharing. Beginning with the composition $Li_{1.32}VO_3$, we observe that over 10% of hops are to 1-TM_{di-vac} tetrahedral sites, and this fraction rises to approximately 25% for $LiVO_3$. Still, our findings indicate that the substantial energy difference between octahedral and 1-TM tetrahedral sites suggests that the 0-TM network is the most relevant pathway for Li^+ transport in DRX materials.

This study, along with the one conducted by Anand et al. [151], supports the notion that a flat energy landscape improves effective Li^+ percolation in DRX structures. However, no established strategy exists for creating a flat energy landscape in such structures. A study on the Li_2VO_2F compound demonstrated that substituting some of the V with Fe or Ti can enhance the electrochemical cyclability and reduce the voltage slope [123], suggesting a flatter energy landscape. Research on high-entropy disordered cathodes [155] has indicated that using a variety of TMs can decrease short-range order and promote long-range Li^+ transport. [155] Although introducing multiple TMs reduces short-range ordering [155], further investigation is needed to understand how this reduction influences the site energy distribution and whether it improves Li^+ transport properties by flattening the energy landscape or if other factors contribute to the enhancement.

The positive impact of F on Li^+ transport has also been demonstrated in other studies. [129] Comparing the experimental diffusivity of Li_2VO_3 and Li_2VO_2F (Figure 4-3d) [39] further emphasizes the advantages of F, as the fluorinated compound exhibits a diffusivity of approximately 1 to 3 orders of magnitude higher than that of the oxide compound. However, the amount of F must be carefully selected, as F can also immobilize Li due to strong Li–F bonds when a high concentration of vacancies is present. [128]

Due to the complexity of Li^+ transport in the DRX materials, accurately predicting Li^+ transport properties requires information on the site energy distribution and interactions, which can be obtained through advanced modeling techniques such as the CE and KMC simulations employed in this work. Our findings emphasize the importance of understanding the factors contributing to a flat energy landscape in DRX materials. More precise results will be achieved if the comparison of Li^+ percolation across different DRX materials is based on both 0-TM connectivity network as well as their energy landscape.

4.5 Conclusions

In this study, we used KMC simulations to examine the kinetics of Li^+ transport in a Li_2VO_3 DRX material. Our findings underscore the necessity of considering the Li occupancy in both tetrahedral and octahedral sites to understand any potential collective ion migration and its possible impact on the macroscopic diffusivity. Our results show that the diffusivity and correlation factor of Li_xVO_3 do not exhibit enhancement as the vacancy concentration increases, which contrasts with the

patterns observed in kinetic studies of some layered and spinel systems. This observation suggests that a rough energy landscape within the DRX structures, can outweigh the influence of vacancy concentrations. Our findings continue to demonstrate that while 1-TM$_{di\text{-}vac}$ channels play a role in the diffusion process, it is the 0-TM channels that remain the primary channels, especially in highly lithiated states where the vacancy concentration is insufficient to activate the 1-TM$_{di\text{-}vac}$ mechanism.

4.6 Supporting information
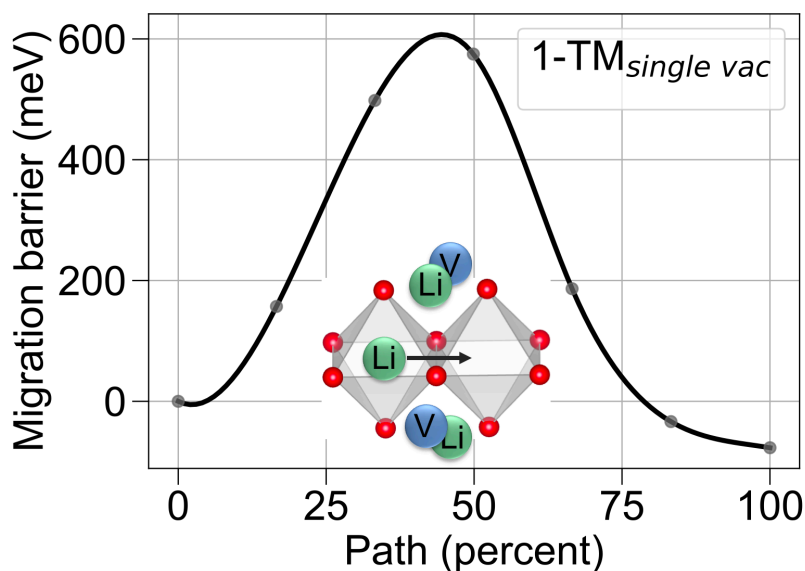
Figure 4-S1 Energy (meV) along the Li migration pathway (%) for the octahedral-to-octahedral mechanism in Li$_2$VO$_3$ is examined when the lower and upper tetrahedral sites face-share with Li and V and one vacancy. Since the migration barrier exceeds 300 meV, it is safe to conclude that Li does not pass through the 1-TM single vacancy path. In addition, the intermediate tetrahedral site does not represent a local minimum in this case. Hence, we did not consider the 1-TM single vacancy hop in our KMC simulation.

57
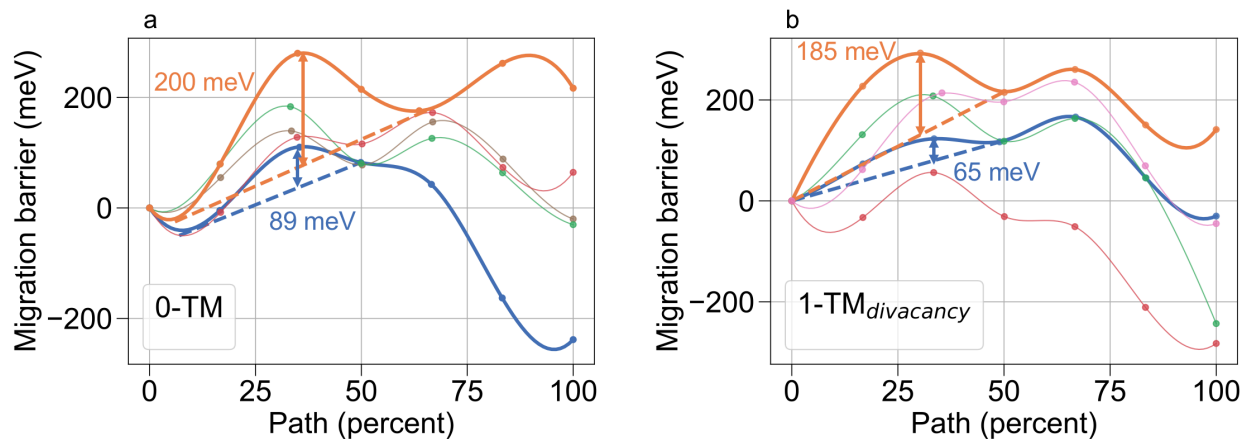
Figure 4-S2 Energy (meV) along the Li migration pathway (%) for the octahedral-tetrahedral-octahedral mechanism in Li_xVO_3 ($1 \leq x \leq 2$): (a) when the tetrahedral site does not share a face with any V and (b) when it shares a face with one V and two octahedral vacancies. The minimum and maximum KRA values are indicated in each case.
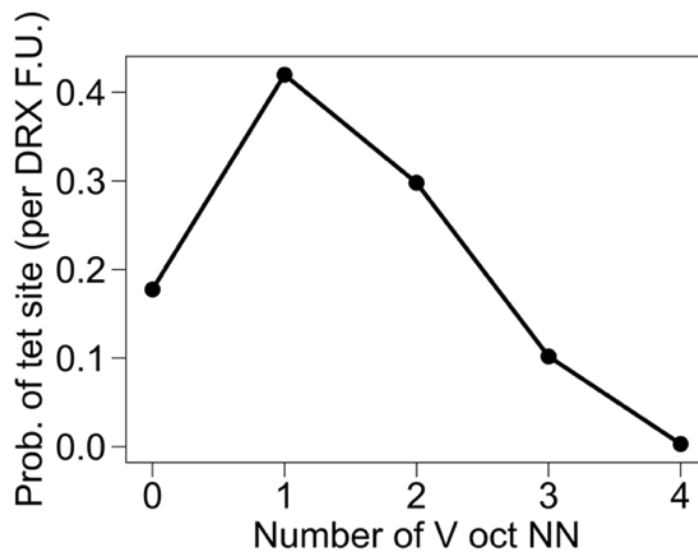
Figure 4-S3 Probability of any tetrahedral site per DRX formula unit (F.U.) with a certain number of nearest-neighbor face-sharing V.

Chapter 5

Conclusion remarks

In this dissertation, we have conducted a detailed analysis of Li^+ migration in Mn-based cathode materials and a thorough examination of short-range ordering and the kinetics of Li^+ transport in vanadium-based disordered rocksalt structure with the presence of Li-excess.

The findings from Chapter 2 indicated that fluorine substitution influences the Li migration energy in $LiMnO_2$, but this impact is largely offset in the presence of Li-excess. Hence, irrespective of the presence of F, systems that are 0-TM percolating can potentially have reasonable Li transport.

In Chapter 3, a study on the cation short-range order of Li and V in $Li_{2-x}VO_3$ revealed that the number of neighboring V around an octahedral Li influences its delithiation. Our research reveals that the quantity of the closest neighboring V significantly impacts the timing of octahedral Li's delithiation. Li extraction is predominantly initiated from octahedral positions with the highest number of adjacent V. In cases of extensive delithiation, most residual octahedral Li is trapped in areas with 2-5 nearest V neighbors, prompting the shift of Li extraction towards tetrahedral sites. Our findings also show that V undergoes oxidation in a way that reduces the amount of V^{5+}–V^{5+} bonds. These findings suggest that future DRX designs should balance the necessary amount of Li-excess for percolation with the possible increase in slope due to a higher concentration of high-voltage tetrahedral Li. Moreover, the presence of over-stabilized tetrahedral Li can impede migration paths, potentially reducing Li^+ diffusivity and energy density. Our findings also unveiled a partially collective migration of Li^+ from octahedral to tetrahedral sites at a partial state of charge, adding valuable insights into the behavior of all DRX materials.

The kinetic study conducted in Chapter 4 using KMC simulations emphasized the importance of considering Li occupancy in both tetrahedral and octahedral sites to fully understand any potential collective ion migration and its impact on macroscopic diffusivity. Unlike certain layered and spinel systems, increased vacancy concentration in Li_xVO_3 does not enhance diffusivity and correlation factor. This implies that an uneven energy landscape in DRX structures can offset the effects of higher vacancy concentrations. Our research consistently reaffirms that the main channels responsible for Li^+ diffusion in DRX compounds are the 0-TM channels.

This dissertation has provided insights into the local migration and macroscopic diffusion of Li^+ in Mn and V-based DRX cathode materials. The findings regarding Li-excess, SRO, and the kinetics of Li transport have broader implications for the study and design of DRX materials. These insights advance our understanding of Li^+ transport properties in these systems and provide valuable information for other DRX chemistries due to the similarity in structural framework and

energy landscape among these materials. By gaining a deeper understanding of the transport properties, the battery community can further develop percolation theory to more effectively characterize the transport properties in DRX systems. Furthermore, as Li's transport properties directly impact the amount of extractable Li during battery cycling, our findings can provide valuable insights into the structural features that can enhance the accessible Li, which influences the rate performance of DRX cathode materials.

References

1. Goodenough, J. B. & Park, K.-S. The Li-Ion Rechargeable Battery: A Perspective. *J. Am. Chem. Soc.* **135**, 1167–1176 (2013).
2. Yang, Y., Bremner, S., Menictas, C. & Kay, M. Battery energy storage system size determination in renewable energy systems: A review. *Renew. Sustain. Energy Rev.* **91**, 109–125 (2018).
3. Ma, J. *et al.* The 2021 battery technology roadmap. *J. Phys. Appl. Phys.* **54**, 183001 (2021).
4. Clément, R. J., Kitchaev, D., Lee, J., & Gerbrand Ceder. Short-Range Order and Unusual Modes of Nickel Redox in a Fluorine-Substituted Disordered Rocksalt Oxide Lithium-Ion Cathode. *Chem. Mater.* **30**, 6945–6956 (2018).
5. Reed, J. & Ceder, G. Role of Electronic Structure in the Susceptibility of Metastable Transition-Metal Oxide Structures to Transformation. *Chem. Rev.* **104**, 4513–4534 (2004).
6. Reed, J. & Ceder, G. Charge, Potential, and Phase Stability of Layered Li (Ni0. 5Mn0. 5) O 2. *Electrochem. Solid-State Lett.* **5**, A145 (2002).
7. Mizushima, K., Jones, P. C., Wiseman, P. J. & Goodenough, J. B. LixCoO2 (0< x<-1): A new cathode material for batteries of high energy density. *Mater. Res. Bull.* **15**, 783–789 (1980).
8. Ohzuku, T. & Ueda, A. Solid-State Redox Reactions of LiCoO2 (R3m) for 4 Volt Secondary Lithium Cells. *J. Electrochem. Soc.* **141**, 2972–2977 (1994).
9. Olivetti, E. A., Ceder, G., Gaustad, G. G. & Fu, X. Lithium-Ion Battery Supply Chain Considerations: Analysis of Potential Bottlenecks in Critical Metals. *Joule* **1**, 229–243 (2017).
10. Howell, D., Cunningham, B., Duong, T. & Faguy, P. Overview of the DOE VTO advanced battery R&D program. *Dep. Energy* (2016).
11. Clément, R. J., Lun, Z. & Ceder, G. Cation-disordered rocksalt transition metal oxides and oxyfluorides for high energy lithium-ion cathodes. *Energy Environ. Sci.* **13**, 345–373 (2020).
12. Delmas, C., Brèthes, S. & Ménétrier, M. ω-LixV2O5 — a new electrode material for rechargeable lithium batteries. *J. Power Sources* **34**, 113–118 (1991).
13. Obrovac, M. N., Mao, O. & Dahn, J. R. Structure and electrochemistry of LiMO2 (M=Ti, Mn, Fe, Co, Ni) prepared by mechanochemical synthesis. *Solid State Ion.* **112**, 9–19 (1998).
14. Lee, J. *et al.* Unlocking the Potential of Cation-Disordered Oxides for Rechargeable Lithium Batteries. *Science* **343**, 519–522 (2014).
15. Urban, A., Lee, J. & Ceder, G. The Configurational Space of Rocksalt-Type Oxides for High-Capacity Lithium Battery Electrodes. *Adv. Energy Mater.* **4**, 1400478 (2014).
16. Lee, J. *et al.* Reversible Mn2+/Mn4+ double redox in lithium-excess cathode materials. *Nature* **556**, 185–190 (2018).
17. Chen, R. *et al.* Disordered Lithium-Rich Oxyfluoride as a Stable Host for Enhanced Li+ Intercalation Storage. *Adv. Energy Mater.* **5**, 1401814 (2015).
18. Yabuuchi, N. *et al.* High-capacity electrode materials for rechargeable lithium batteries: Li3NbO4-based system with cation-disordered rocksalt structure. *Proc. Natl. Acad. Sci.* **112**, 7650–7655 (2015).

19. Ren, S. *et al.* Improved Voltage and Cycling for Li+ Intercalation in High-Capacity Disordered Oxyfluoride Cathodes. *Adv. Sci.* **2**, 1500128 (2015).
20. Ji, H. *et al.* Hidden structural and chemical order controls lithium transport in cation-disordered oxides for rechargeable batteries. *Nat. Commun.* **10**, 592 (2019).
21. Lee, J. *et al.* Determining the Criticality of Li-Excess for Disordered-Rocksalt Li-Ion Battery Cathodes. *Adv. Energy Mater.* **11**, 2100204 (2021).
22. A. House, R. *et al.* Lithium manganese oxyfluoride as a new cathode material exhibiting oxygen redox. *Energy Environ. Sci.* **11**, 926–932 (2018).
23. Yabuuchi, N. *et al.* Origin of stabilization and destabilization in solid-state redox reaction of oxide ions for lithium-ion batteries. *Nat. Commun.* **7**, 13814 (2016).
24. Kitchaev, D. A. *et al.* Design principles for high transition metal capacity in disordered rocksalt Li-ion cathodes. *Energy Environ. Sci.* **11**, 2159–2171 (2018).
25. Van der Ven, A., Ceder, G., Asta, M. & Tepesch, P. D. First-principles theory of ionic diffusion with nondilute carriers. *Phys. Rev. B* **64**, 184307 (2001).
26. Jadidi, Z., Chen, T., Xiao, P., Urban, A. & Ceder, G. Effect of fluorination and Li-excess on the Li migration barrier in Mn-based cathode materials. *J. Mater. Chem. A* **8**, 19965–19974 (2020).
27. Kang, K. Electrodes with High Power and High Capacity for Rechargeable Lithium Batteries. *Science* **311**, 977–980 (2006).
28. Abdellahi, A., Urban, A., Dacek, S. & Ceder, G. Understanding the effect of cation disorder on the voltage profile of lithium transition-metal oxides. *Chem. Mater.* **28**, 5373–5383 (2016).
29. Guo, X., Chen, C. & Ong, S. P. Intercalation Chemistry of the Disordered Rocksalt Li3V2O5 Anode from Cluster Expansions and Machine Learning Interatomic Potentials. *Chem. Mater.* **35**, 1537–1546 (2023).
30. Liu, H. *et al.* A disordered rock salt anode for fast-charging lithium-ion batteries. *Nature* **585**, 63–67 (2020).
31. Bhattacharya, J. & Van der Ven, A. First-principles study of competing mechanisms of nondilute Li diffusion in spinel Li x TiS 2. *Phys. Rev. B* **83**, 144302 (2011).
32. Kolli, S. K. & Van der Ven, A. Elucidating the Factors That Cause Cation Diffusion Shutdown in Spinel-Based Electrodes. *Chem. Mater.* **33**, 6421–6432 (2021).
33. Jow, T. R., Delp, S. A., Allen, J. L., Jones, J.-P. & Smart, M. C. Factors Limiting Li+ Charge Transfer Kinetics in Li-Ion Batteries. *J. Electrochem. Soc.* **165**, A361 (2018).
34. Van der Ven, A. & Ceder, G. Lithium diffusion in layered Li x CoO2. *Electrochem. Solid-State Lett.* **3**, 301–304 (2000).
35. Bhattacharya, J. & Van Der Ven, A. Phase stability and nondilute Li diffusion in spinel Li 1 + x Ti 2 O 4. *Phys. Rev. B* **81**, 104304 (2010).
36. Van Der Ven, A., Thomas, J. C., Xu, Q., Swoboda, B. & Morgan, D. Nondilute diffusion from first principles: Li diffusion in Li x TiS 2. *Phys. Rev. B* **78**, 104306 (2008).
37. Huang, J. *et al.* Non-topotactic reactions enable high rate capability in Li-rich cathode materials. *Nat. Energy* **6**, 706–714 (2021).
38. Wang, X. *et al.* Structure evolution and thermal stability of high-energy-density Li-ion battery cathode Li2VO2F. *J. Electrochem. Soc.* **164**, A1552 (2017).
39. Chen, R. *et al.* Li+ intercalation in isostructural Li2VO3 and Li2VO2F with O2− and mixed O2−/F− anions. *Phys. Chem. Chem. Phys.* **17**, 17288–17295 (2015).

40. Cambaz, M. A. *et al.* Oxygen Activity in Li-Rich Disordered Rock-Salt Oxide and the Influence of LiNbO3 Surface Modification on the Electrochemical Performance. *Chem. Mater.* **31**, 4330–4340 (2019).

41. Clément, R. J., Lun, Z. & Ceder, G. Cation-disordered rocksalt transition metal oxides and oxyfluorides for high energy lithium-ion cathodes. *Energy Environ. Sci.* **13**, 345–373 (2020).

42. Lun, Z. *et al.* Improved Cycling Performance of Li-Excess Cation-Disordered Cathode Materials upon Fluorine Substitution. *Adv. Energy Mater.* **9**, 1802959 (2019).

43. Redel, K., Kulka, A., Plewa, A. & Molenda, J. High-performance Li-rich layered transition metal oxide cathode materials for Li-ion batteries. *J. Electrochem. Soc.* **166**, A5333–A5342 (2019).

44. Lee, J. *et al.* Reversible Mn 2+/Mn 4+ double redox in lithium-excess cathode materials. *Nature* **556**, 185–190 (2018).

45. Lun, Z. *et al.* Design principles for high-capacity Mn-based cation-disordered rocksalt cathodes. *Chem* **6**, 153–168 (2020).

46. House, R. A. *et al.* What triggers oxygen loss in oxygen redox cathode materials? *Chem. Mater.* **31**, 3293–3300 (2019).

47. Seo, D.-H. *et al.* The structural and chemical origin of the oxygen redox activity in layered and cation-disordered Li-excess cathode materials. *Nat. Chem.* **8**, 692–697 (2016).

48. Chen, D., Kan, W. H. & Chen, G. Understanding Performance Degradation in Cation-Disordered Rock-Salt Oxide Cathodes. *Adv. Energy Mater.* **9**, 1901255 (2019).

49. Kan, W. H. *et al.* Unravelling solid-state redox chemistry in Li1. 3Nb0. 3Mn0. 4O2 single-crystal cathode material. *Chem. Mater.* **30**, 1655–1666 (2018).

50. Koga, H. *et al.* Reversible oxygen participation to the redox processes revealed for Li1. 20Mn0. 54Co0. 13Ni0. 13O2. *J. Electrochem. Soc.* **160**, A786–A792 (2013).

51. Armstrong, A. R. *et al.* Demonstrating oxygen loss and associated structural reorganization in the lithium battery cathode Li [Ni0. 2Li0. 2Mn0. 6] O2. *J. Am. Chem. Soc.* **128**, 8694–8698 (2006).

52. Ouyang, B. *et al.* Effect of Fluorination on Lithium Transport and Short-Range Order in Disordered-Rocksalt-Type Lithium-Ion Battery Cathodes. *Adv. Energy Mater.* 1903240 (2020).

53. Van der Ven, A. & Ceder, G. Lithium diffusion mechanisms in layered intercalation compounds. *J. Power Sources* **97–98**, 529–531 (2001).

54. Van der Ven, A., Bhattacharya, J. & Belak, A. A. Understanding Li Diffusion in Li-Intercalation Compounds. *Acc. Chem. Res.* **46**, 1216–1225 (2013).

55. Ceder, G. & Mishra, S. K. The Stability of Orthorhombic and Monoclinic-Layered LiMnO2. *Electrochem. Solid-State Lett.* **2**, 550 (1999).

56. Jang, Y.-I., Chou, F. C., Huang, B., Sadoway, D. R. & Chiang, Y.-M. Magnetic characterization of orthorhombic LiMnO2 and electrochemically transformed spinel LixMnO2 (x< 1). *J. Phys. Chem. Solids* **64**, 2525–2533 (2003).

57. Richards, W. D., Dacek, S. T., Kitchaev, D. A. & Ceder, G. Fluorination of Lithium-Excess Transition Metal Oxide Cathode Materials. *Adv. Energy Mater.* **8**, 1701533 (2018).

58. Hohenberg, P. & Kohn, W. Inhomogeneous electron gas. *Phys. Rev.* **136**, B864 (1964).

59. Kohn, W. & Sham, L. J. Self-consistent equations including exchange and correlation effects. *Phys. Rev.* **140**, A1133 (1965).

60. Perdew, J. P., Burke, K. & Ernzerhof, M. Generalized gradient approximation made simple. *Phys. Rev. Lett.* **77**, 3865 (1996).
61. Blöchl, P. E. Projector augmented-wave method. *Phys. Rev. B* **50**, 17953 (1994).
62. Kresse, G. & Joubert, D. From ultrasoft pseudopotentials to the projector augmented-wave method. *Phys. Rev. B* **59**, 1758 (1999).
63. Kresse, G. & Furthmüller, J. Efficiency of ab-initio total energy calculations for metals and semiconductors using a plane-wave basis set. *Comput. Mater. Sci.* **6**, 15–50 (1996).
64. Kresse, G. & Furthmüller, J. Efficient iterative schemes for ab initio total-energy calculations using a plane-wave basis set. *Phys. Rev. B* **54**, 11169 (1996).
65. Dudarev, S. L., Botton, G. A., Savrasov, S. Y., Humphreys, C. J. & Sutton, A. P. Electron-energy-loss spectra and the structural stability of nickel oxide: An LSDA+ U study. *Phys. Rev. B* **57**, 1505 (1998).
66. Jain, A. *et al.* Commentary: The Materials Project: A materials genome approach to accelerating materials innovation. *APL Mater.* **1**, 011002 (2013).
67. Henkelman, G. & Jónsson, H. Improved tangent estimate in the nudged elastic band method for finding minimum energy paths and saddle points. *J. Chem. Phys.* **113**, 9978–9985 (2000).
68. Urban, A., Seo, D.-H. & Ceder, G. Computational understanding of Li-ion batteries. *Npj Comput. Mater.* **2**, 1–13 (2016).
69. Asari, Y., Suwa, Y. & Hamada, T. Formation and diffusion of vacancy-polaron complex in olivine-type LiMnPO 4 and LiFePO 4. *Phys. Rev. B* **84**, 134113 (2011).
70. Kong, F. *et al.* Ab initio study of doping effects on LiMnO2 and Li2MnO3 cathode materials for Li-ion batteries. *J. Mater. Chem. A* **3**, 8489–8500 (2015).
71. Zarkevich, N. A. & Johnson, D. D. Nudged-elastic band method with two climbing images: Finding transition states in complex energy landscapes. *J. Chem. Phys.* **142**, 024106 (2015).
72. Henkelman, G. A. *Methods for calculating rates of transitions with application to catalysis and crystal growth*. (University of Washington, 2001).
73. Ohno, S. *et al.* How certain are the reported ionic conductivities of thiophosphate-based solid electrolytes? An interlaboratory study. *ACS Energy Lett.* **5**, 910–915 (2020).
74. Kang, K. & Ceder, G. Factors that affect Li mobility in layered lithium transition metal oxides. *Phys. Rev. B* **74**, 094105 (2006).
75. Wei, Y. *et al.* Kinetics tuning of Li-ion diffusion in layered Li (Ni x Mn y Co z) O2. *J. Am. Chem. Soc.* **137**, 8364–8367 (2015).
76. Xiao, W. *et al.* Insight into fast Li diffusion in Li-excess spinel lithium manganese oxide. *J. Mater. Chem. A* **6**, 9893–9898 (2018).
77. Ma, X., Kang, B. & Ceder, G. High rate micron-sized ordered LiNi0. 5Mn1. 5O4. *J. Electrochem. Soc.* **157**, A925–A931 (2010).
78. Morgan, D., Van der Ven, A. & Ceder, G. Li conductivity in Li x MPO 4 (M= Mn, Fe, Co, Ni) olivine materials. *Electrochem. Solid State Lett.* **7**, A30 (2003).
79. Zeng, H. *et al.* Ab initio identification of the Li-rich phase in LiFePO 4. *Phys. Chem. Chem. Phys.* **20**, 17497–17503 (2018).
80. Xia, H., Meng, S. Y., Lu, L. & Ceder, G. Electrochemical Behavior and Li Diffusion Study of LiCoO₂ Thin Film Electrodes Prepared by PLD. (2007).
81. Ji, H. *et al.* Ultrahigh power and energy density in partially ordered lithium-ion cathode materials. *Nat. Energy* **5**, 213–221 (2020).

82. Euchner, H., Chang, J. H. & Groß, A. On stability and kinetics of Li-rich transition metal oxides and oxyfluorides. *J. Mater. Chem. A* **8**, 7956–7967 (2020).

83. Lee, J. *et al.* Mitigating oxygen loss to improve the cycling performance of high capacity cation-disordered cathode materials. *Nat. Commun.* **8**, 981 (2017).

84. Ji, H. *et al.* Hidden structural and chemical order controls lithium transport in cation-disordered oxides for rechargeable batteries. *Nat. Commun.* **10**, 592 (2019).

85. Jones, M. A. *et al.* Short-range ordering in a battery electrode, the 'cation-disordered' rocksalt Li1.25Nb0.25Mn0.5O2. *Chem. Commun.* **55**, 9027–9030 (2019).

86. Kan, W. H. *et al.* Understanding the Effect of Local Short-Range Ordering on Lithium Diffusion in Li1.3Nb0.3Mn0.4O2 Single-Crystal Cathode. *Chem* **4**, 2108–2123 (2018).

87. Cowley, J. M. X-Ray Measurement of Order in Single Crystals of Cu ₃ Au. *J. Appl. Phys.* **21**, 24–30 (1950).

88. Warren, B. E., Averbach, B. L. & Roberts, B. W. Atomic Size Effect in the X-Ray Scattering by Alloys. *J. Appl. Phys.* **22**, 1493–1496 (1951).

89. Fontaine, D. D. An analysis of clustering and ordering in multicomponent solid solutions— II fluctuations and kinetics. *J. Phys. Chem. Solids* **34**, 1285–1304 (1973).

90. Schönfeld, B. Local atomic arrangements in binary alloys. *Prog. Mater. Sci.* **44**, 435–543 (1999).

91. Dubiel, S. M. & Cieslak, J. Short-range order in iron-rich Fe-Cr alloys as revealed by Mössbauer spectroscopy. *Phys. Rev. B* **83**, 180202 (2011).

92. Staunton, J. B., Johnson, D. D. & Pinski, F. J. Compositional short-range ordering in metallic alloys: Band-filling, charge-transfer, and size effects from a first-principles all-electron Landau-type theory. *Phys. Rev. B* **50**, 1450–1472 (1994).

93. Reinhard, L. & Moss, S. C. Recent studies of short-range order in alloys: the Cowley theory revisited. *Ultramicroscopy* **52**, 223–232 (1993).

94. Yang, J. H., Chen, T., Barroso-Luque, L., Jadidi, Z. & Ceder, G. Approaches for handling high-dimensional cluster expansions of ionic systems. *Npj Comput. Mater.* **8**, 133 (2022).

95. Chen, T., Yang, J., Barroso-Luque, L. & Ceder, G. Removing the Two-Phase Transition in Spinel LiMn ₂ O ₄ through Cation Disorder. *ACS Energy Lett.* 314–319 (2022) doi:10.1021/acsenergylett.2c02141.

96. Yang, J. H. & Ceder, G. Activated Internetwork Pathways in Partially-Disordered Spinel Cathode Materials with Ultrahigh Rate Performance. *Adv. Energy Mater.* **13**, 2202955 (2023).

97. Sanchez, J. M., Ducastelle, F. & Gratias, D. Generalized cluster description of multicomponent systems. *Phys. Stat. Mech. Its Appl.* **128**, 334–350 (1984).

98. De Fontaine, D. Cluster approach to order-disorder transformations in alloys. *Solid State Phys.* **47**, 33–176 (1994).

99. Laks, D. B., Ferreira, L. G., Froyen, S. & Zunger, A. Efficient cluster expansion for substitutional systems. *Phys. Rev. B* **46**, 12587–12605 (1992).

100. Wang, L., Maxisch, T. & Ceder, G. Oxidation energies of transition metal oxides within the GGA+ U framework. *Phys. Rev. B* **73**, 195107 (2006).

101. Van De Walle, A. Multicomponent multisublattice alloys, nonconfigurational entropy and other additions to the Alloy Theoretic Automated Toolkit. *Calphad* **33**, 266–278 (2009).

102. Ceder, G., Garbulsky, G. D. & Tepesch, P. D. Convergent real-space cluster expansion for configurational disorder in ionic systems. *Phys. Rev. B* **51**, 11257 (1995).

103. Chen, T., Yang, J., Barroso-Luque, L. & Ceder, G. Removing the Two-Phase Transition in Spinel LiMn2O4 through Cation Disorder. *ACS Energy Lett.* 314–319 (2022) doi:10.1021/acsenergylett.2c02141.

104. Seko, A. & Tanaka, I. Cluster expansion of multicomponent ionic systems with controlled accuracy: importance of long-range interactions in heterovalent ionic systems. *J. Phys. Condens. Matter* **26**, 115403 (2014).

105. Barroso-Luque, L. *et al.* Cluster expansions of multicomponent ionic materials: Formalism and methodology. *Phys. Rev. B* **106**, 144202 (2022).

106. Hastings, W. K. Monte Carlo sampling methods using Markov chains and their applications. (1970).

107. Huang, W. *et al.* Construction of ground-state preserving sparse lattice models for predictive materials simulations. *Npj Comput. Mater.* **3**, 1–9 (2017).

108. Seko, A., Togo, A., Oba, F. & Tanaka, I. Structure and Stability of a Homologous Series of Tin Oxides. *Phys. Rev. Lett.* **100**, 045702 (2008).

109. Barroso-Luque, L. *et al.* smol: A Python package for cluster expansions andbeyond. *J. Open Source Softw.* **7**, 4504 (2022).

110. Tibshirani, R. Regression Shrinkage and Selection Via the Lasso. *J. R. Stat. Soc. Ser. B Methodol.* **58**, 267–288 (1996).

111. Ong, S. P. *et al.* Python Materials Genomics (pymatgen): A robust, open-source python library for materials analysis. *Comput. Mater. Sci.* **68**, 314–319 (2013).

112. Lee, J. B. *et al.* Unusual conversion-type lithiation in LiVO3 electrode for lithium-ion batteries. *Chem. Mater.* **28**, 5314–5320 (2016).

113. Mozhzhukhina, N. *et al.* Short-range ordering in the Li-rich disordered rock salt cathode material Li2VO2F revealed by Raman spectroscopy. *J. Raman Spectrosc.* **51**, 2095–2101 (2020).

114. Loftager, S. *et al.* Novel Cathode Materials for Lithium Ion Batteries. *Lir. Eur. Union's Horiz.* (2018).

115. Wolverton, C. & Zunger, A. Cation and vacancy ordering in Li x CoO 2. *Phys. Rev. B* **57**, 2242–2252 (1998).

116. Abdellahi, A., Urban, A., Dacek, S. & Ceder, G. The Effect of Cation Disorder on the Average Li Intercalation Voltage of Transition-Metal Oxides. *Chem. Mater.* **28**, 3659–3665 (2016).

117. Saubanère, M., Yahia, M. B., Lebègue, S. & Doublet, M.-L. An intuitive and efficient method for cell voltage prediction of lithium and sodium-ion batteries. *Nat. Commun.* **5**, 5559 (2014).

118. Kosova, N. V., Rezepova, D. O. & Slobodyuk, A. B. Effect of annealing temperature on the structure and electrochemistry of LiVO3. *Electrochimica Acta* **167**, 75–83 (2015).

119. Konuma, I. *et al.* A near dimensionally invariable high-capacity positive electrode material. *Nat. Mater.* **22**, 225–234 (2023).

120. Nakajima, M. & Yabuuchi, N. Lithium-excess cation-disordered rocksalt-type oxide with nanoscale phase segregation: Li1. 25Nb0. 25V0. 5O2. *Chem. Mater.* **29**, 6927–6935 (2017).

121. Baur, C., Lăcătuşu, M.-E., Fichtner, M. & Johnsen, R. E. Insights into structural transformations in the local structure of Li2VO2F using operando x-ray diffraction and total scattering: amorphization and recrystallization. *ACS Appl. Mater. Interfaces* **12**, 27010–27016 (2020).

122. Aydinol, M. K., Kohan, A. F. & Ceder, G. Ab initio calculation of the intercalation voltage of lithium-transition-metal oxide electrodes for rechargeable batteries. *J. Power Sources* **68**, 664–668 (1997).

123. Baur, C. *et al.* Improved cycling stability in high-capacity Li-rich vanadium containing disordered rock salt oxyfluoride cathodes. *J. Mater. Chem. A* **7**, 21244–21253 (2019).

124. Ok, K. M. *et al.* Distortions in Octahedrally Coordinated d ^{0} Transition Metal Oxides: A Continuous Symmetry Measures Approach. *Chem. Mater.* **18**, 3176–3183 (2006).

125. Urban, A., Abdellahi, A., Dacek, S., Artrith, N. & Ceder, G. Electronic-structure origin of cation disorder in transition-metal oxides. *Phys. Rev. Lett.* **119**, 176402 (2017).

126. Guo, X., Chen, C. & Ong, S. P. The Intercalation Chemistry of the Disordered RockSalt Li3V2O5 Anode from Cluster Expansions and Machine Learning Interatomic Potentials. Preprint at https://doi.org/10.48550/arXiv.2208.14420 (2022).

127. Huang, L. *et al.* Optimizing Li-Excess Cation-Disordered Rocksalt Cathode Design Through Partial Li Deficiency. *Adv. Energy Mater.* **n/a**, 2202345.

128. Zhong, P. *et al.* Increasing Capacity in Disordered Rocksalt Cathodes by Mg Doping. *Chem. Mater.* **32**, 10728–10736 (2020).

129. Ouyang, B. *et al.* Effect of Fluorination on Lithium Transport and Short-Range Order in Disordered-Rocksalt-Type Lithium-Ion Battery Cathodes. *Adv. Energy Mater.* **10**, 1903240 (2020).

130. Andersen, M., Panosetti, C. & Reuter, K. A Practical Guide to Surface Kinetic Monte Carlo Simulations. *Front. Chem.* **7**, (2019).

131. Jadidi, Z., Yang, J. H., Chen, T., Barroso-Luque, L. & Ceder, G. Ab-initio study of short-range ordering in vanadium-based disordered rocksalt structures. Preprint at https://doi.org/10.48550/arXiv.2304.14645 (2023).

132. Richards, W. D., Dacek, S. T., Kitchaev, D. A. & Ceder, G. Fluorination of lithium-excess transition metal oxide cathode materials. *Adv. Energy Mater.* **8**, 1701533 (2018).

133. Hohenberg, P. & Kohn, W. Inhomogeneous electron gas phys. rev. 136. *B864* (1964).

134. Kohn, W. & Sham, L. J. Self-Consistent Equations Including Exchange and Correlation Effects. *Phys. Rev.* **140**, A1133–A1138 (1965).

135. Kresse, G. & Furthmüller, J. Efficiency of ab-initio total energy calculations for metals and semiconductors using a plane-wave basis set. *Comput. Mater. Sci.* **6**, 15–50 (1996).

136. Kresse, G. & Furthmüller, J. Efficient iterative schemes for ab initio total-energy calculations using a plane-wave basis set. *Phys. Rev. B* **54**, 11169–11186 (1996).

137. Kresse, G. & Joubert, D. From ultrasoft pseudopotentials to the projector augmented-wave method. *Phys. Rev. B* **59**, 1758 (1999).

138. Blöchl, P. E. Projector augmented-wave method. *Phys. Rev. B* **50**, 17953 (1994).

139. Perdew, J. P., Burke, K. & Ernzerhof, M. Generalized gradient approximation made simple. *Phys. Rev. Lett.* **77**, 3865 (1996).

140. Bruce, P. G., Lisowska-Oleksiak, A., Saidi, M. Y. & Vincent, C. A. Vacancy diffusion in the intercalation electrode Li1−xNiO2. *Solid State Ion.* **57**, 353–358 (1992).

141. Zwanzig, R. Time-Correlation Functions and Transport Coefficients in Statistical Mechanics. *Annu. Rev. Phys. Chem.* **16**, 67–102 (1965).

142. Gomer, R. Diffusion of adsorbates on metal surfaces. *Rep. Prog. Phys.* **53**, 917–1002 (1990).

143. Zhou, Y. & Miller, G. H. Green−Kubo Formulas for Mutual Diffusion Coefficients in Multicomponent Systems. *J. Phys. Chem.* **100**, 5516–5524 (1996).

144. Richards, P. M. Theory of one-dimensional hopping conductivity and diffusion. *Phys. Rev. B* **16**, 1393–1409 (1977).

145. Mazenko, G., Banavar, J. R. & Gomer, R. Diffusion coefficients and the time auto-correlation function of density fluctuations. *Surf. Sci.* **107**, 459–468 (1981).

146. Vineyard, G. H. Frequency factors and isotope effects in solid state rate processes. *J. Phys. Chem. Solids* **3**, 121–127 (1957).

147. Bortz, A. B., Kalos, M. H. & Lebowitz, J. L. A new algorithm for Monte Carlo simulation of Ising spin systems. *J. Comput. Phys.* **17**, 10–18 (1975).

148. Bulnes, F. M., Pereyra, V. D. & Riccardo, J. L. Collective surface diffusion: n-fold way kinetic Monte Carlo simulation. *Phys. Rev. E* **58**, 86 (1998).

149. Ok, K. M. *et al.* Distortions in octahedrally coordinated d0 transition metal oxides: A continuous symmetry measures approach. *Chem. Mater.* **18**, 3176–3183 (2006).

150. Loftager, S. *et al. Novel Cathode Materials for Lithium Ion Batteries.* https://ec.europa.eu/research/participants/documents/downloadPublic?documentIds=080166e5be07724f&appId=PPGMS (2018).

151. Anand, S., Chen, T. & Ceder, G. Impact of the Energy Landscape on the Ionic Transport of Disordered Rocksalt Cathodes. Preprint at https://doi.org/10.48550/arXiv.2301.10842 (2023).

152. Jacobson, S. H., Nitzan, A. & Ratner, M. A. Charge carrier correlations in framework solid electrolytes. *Solid State Ion.* **5**, 125–128 (1981).

153. Zeng, Y. *et al.* High-entropy mechanism to boost ionic conductivity. *Science* **378**, 1320–1324 (2022).

154. Vargas-Barbosa, N. M. & Roling, B. Dynamic ion correlations in solid and liquid electrolytes: how do they affect charge and mass transport? *ChemElectroChem* **7**, 367–385 (2020).

155. Lun, Z. *et al.* Cation-disordered rocksalt-type high-entropy cathodes for Li-ion batteries. *Nat. Mater.* **20**, 214–221 (2021).